Development of a cryogenic minimum deviation angle measurement system in the mid-infrared to determine the refractive index of CdZnTe, a material for the immersion grating

Umi Enokidani

Doctor of Philosophy

Department of Space and Astronautical Science
School of Physical Sciences

The Graduate University for Advanced Studies, SOKENDAI

February 25, 2025

ABSTRACT

This paper presents the results of refractive index measurements of CdZnTe at the wavelength range of 10.6, 11.4, 14.0, and 17.1 μm and in the temperature range between 4 and room temperature, and the development of a high-precision cryogenic mid-infrared refractive index measurement system. We show how these results have influenced the detailed optical design of HRS (High Resolution Spectrometer, wavelength range between 10 and 18 μm, spectral resolution $R = \lambda/\Delta\lambda > 25,000$, operating temperature $T < 20$ K), one of the instruments on board GREX-PLUS (Galaxy Reionization EXplorer and PLanetary Universe Spectrometer).

GREX-PLUS is an ambitious mission designed to explore a wide range of astrophysical phenomena, including the formation of galaxies and planetary systems, and to make detailed studies of planetary atmospheres and the potential for life beyond Earth. One of the science topics of particular interest is the observation of H_2O snow lines in protoplanetary disks. We are developing a CdZnTe immersion grating for a compact high-dispersion mid-infrared spectrometer GREX-PLUS/HRS. One of the key challenges in the design of high-dispersion spectrometers for space-based infrared astronomy is the need to miniaturize components without sacrificing performance. Immersion gratings are a promising solution to this problem. By using an immersion grating, the spectrometer size can be reduced to $1/n$ ($1/n^3$ in volume, n: refractive index) compared to conventional diffraction gratings. This allows the spectrometer to be significantly smaller and lighter, which is crucial for space missions where weight and size are limiting factors. CdZnTe is promising as a material for immersion gratings for the wavelength range between 10 and 18 μm.

Immersion gratings are useful for miniaturization of spectrometers, but have not been established in the mid-IR due to the lack of materials with well-known optical constants at cryogenic temperatures. CdZnTe has been proposed as a promising material, but its n and its temperature dependence in the wavelength range between 10 and 18 μm, which are important for optical design, have not been directly measured. n is a crucial parameter for the spectral resolution and optical design of the spectrometer. In the GREX-PLUS/HRS design, n values with a measurement accuracy of $\Delta n_{\rm req} < 1.0 \times 10^{-3}$

are required to maximize efficiency at certain wavelengths (e.g., 17.754 mum).

In this study, we developed a high-precision cryogenic mid-infrared refractive index measurement system that operates at wavelengths of 10.6, 11.4, 14.0, and 17.1 μm and in a temperature range between 12.4 and 300 K. The measurement system is characterized by its innovative features, including the realization of a highly efficient optical system, the construction of a cooling system capable of achieving cryogenic temperatures, and the establishment of a minimum deviation measurement method utilizing a single-element detector.

Using the measurement system, two experiments were performed to obtain n of CdZnTe. In the first experiment, the apex angle of the prism was measured using visible autocollimation. The second experiment was a declination measurement in the mid-infrared at cryogenic temperatures.

From the results of the two experiments, n of CdZnTe at wavelengths of 10.6, 11.4, 14.0, and 17.1 μm and temperatures between 12.4 K and 292.84 K was obtained with an accuracy of $\Delta n_{\mathrm{total}} < 1.3 \times 10^{-3}$. Using these refractive indices and their measurement accuracy, three topics were discussed. First, the temperature dependence of n of CdZnTe at low temperatures for each wavelength was revealed, indicating a difference in temperature dependence between CdZnTe and CdTe. Second, it was demonstrated that the previously estimated n of CdZnTe, based on the temperature dependence of CdTe, does not meet the required precision of $\Delta n_{\mathrm{req}} < 1.0 \times 10^{-3}$, suggesting the importance of measuring refractive indices at cryogenic temperatures in the mid-infrared region. Finally, the impact of the system's measurement precision on the design of immersion gratings was examined. For ground-based high-dispersion spectrometers, the diffraction efficiency could drop to 75–85%, while for GREX-PLUS, the influence is considered negligible due to its lower diffraction order and wider free spectral range. The current accuracy of $\Delta n_{\mathrm{total}} < 1.3 \times 10^{-3}$ is considered sufficient for GREX-PLUS.

The results of this research are expected to play a key role in refining the optical design of the HRS and ensuring the success of the GREX-PLUS mission. Moreover, the techniques and findings presented in this thesis can be applied to the study of other

materials and wavelength ranges, potentially benefiting a wide range of future space missions in the field of infrared astronomy.

Contents

List of Figures

List of Tables

Chapter 1

INTRODUCTION

1.1 Space Infrared Telescope Features and Current Status

Infrared radiation is a type of electromagnetic wave, with wavelengths of $1 \sim 3$ μm categorized as near-infrared, $3 \sim 30$ μm as mid-infrared, and $30 \sim 1000$ μm as far-infrared. The infrared region contains the peak of blackbody radiation spectra for temperatures around $3 \sim 3000$ K, making it suitable for observing low-temperature interstellar matter and planets both inside and outside the solar system. One example is the observation of interstellar dust, which is a component of interstellar matter. Interstellar dust coexists with interstellar gas and is heated by visible light and ultraviolet radiation from stars. It is thought that low-temperature dust is heated to tens of kelvins, while high-temperature dust can reach thousands of kelvins, where sublimation occurs. Thus, infrared observations are useful. Infrared observations are also effective for observing the regions where stars and planets form. Typically, the radiation peak of a star exists in the ultraviolet to infrared region, but the visible light from stars in the central region of the galaxy is dimmed by interstellar matter. This is because, as we are located within the galactic disk, the visible light from the center of the galaxy passes through interstellar matter, where it is scattered and absorbed by interstellar dust. This scattering and absorption of electromagnetic waves are maximized at visible wavelengths, which are comparable to the

size of the dust particles. Infrared light, however, is less affected by extinction, allowing us to observe the central parts of the galaxy and star formation regions shrouded in dense interstellar gas that cannot be detected in visible light. Additionally, to explore stars and galaxies born in the early universe, we need to observe light from distant objects. Due to redshift, this light is stretched to longer wavelengths and can be observed in the infrared. Furthermore, many spectral lines associated with vibrational and rotational transitions of interstellar gas molecules, as well as fine-structure lines of atoms and ions, exist in the infrared region. In this way, astronomical observations using infrared wavelengths are crucial for understanding the early universe, the history of star and planet formation, and the evolution of galaxies.

However, most of the infrared radiation, except for the 10 and 20 μm bands known as atmospheric windows, is absorbed by the Earth's atmosphere, which limits ground-based observations (Figure 1.1). In particular, it is challenging to observe the mid- to far-infrared regions beyond 10 μm from the ground. Additionally, the thermal radiation from the Earth's atmosphere peaks in the infrared region and is significantly brighter than cosmic infrared radiation, increasing noise and further complicating infrared observations from the ground.

One solution to this problem is to equip telescopes on artificial satellites and launch them into space. By placing telescopes in space, where there are no atmospheric constraints that hinder astronomical observations, it becomes possible to observe wavelength bands that are otherwise unobservable from the ground. Moreover, without the influence of the Earth's atmospheric thermal radiation, the detection limit can be dramatically improved compared to ground-based telescopes of the same aperture, allowing the observation of fainter celestial objects.

To take full advantage of these benefits, it is necessary to cool the entire observational system, including the telescope itself, to cryogenic temperatures, as shown in Figure 1.2. A room-temperature telescope (300 K) is insufficient because the infrared radiation emitted by the telescope itself would drown out the infrared radiation from the celestial objects being observed. Cooling the telescope reduces its thermal emission, and the peak

wavelength of this emission shifts to longer wavelengths, enabling high sensitivity even in the far-infrared region. Examples of actual space infrared telescopes are shown in Table 1.1.

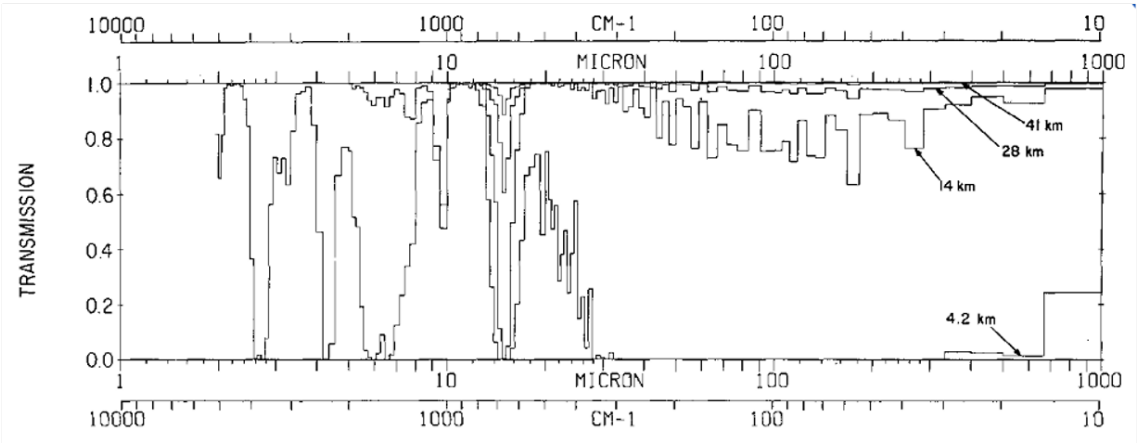

Figure 1.1: Atmospheric transmission from the summit of Mauna Kea to balloon observation altitude [1]

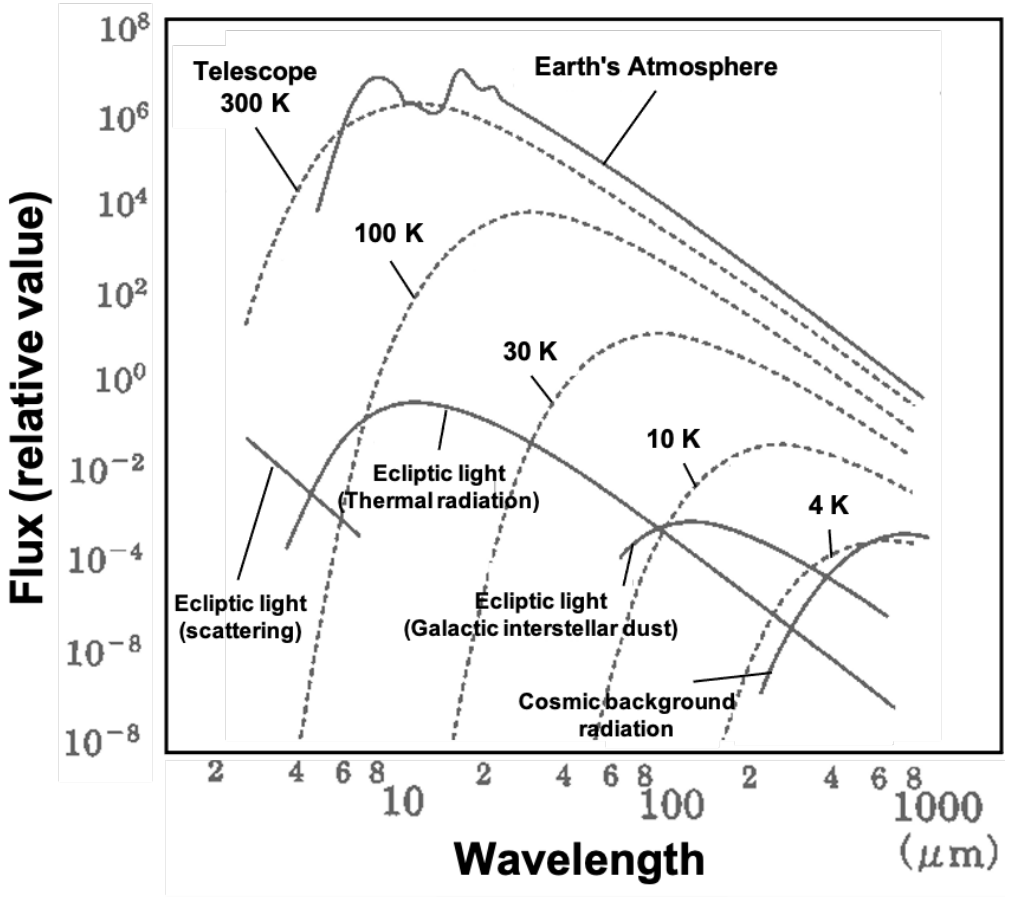

Figure 1.2: Comparison of infrared emission from the Earth's atmosphere and telescopes with celestial infrared radiation [2]

Table 1.1: Observation wavelengths and operating temperatures of major space infrared telescopes

Telescope	Launch year (Year)	Aperture (m)	Observation wavelength (μm)	Operating temperature (K)
IRAS [3]	1983	0.57	10 - 100	< 3
IRTS [4]	1995	0.15	1.4 - 700	1.9
ISO [5]	1995	0.6	2.5 - 240	3
Spitzer Space Telescope [6]	2003	0.85	3.6 - 160	5.5
AKARI [7]	2006	0.68	2 - 180	5.8
WISE [8]	2009	0.4	3.3 - 23	17
Herschel Space Observatory [9]	2009	3.5	55 - 671	$\simeq 85$
JWST [10]	2021	6.5	0.6 - 28	$\simeq 40$
SPICA [11]	(cancelled)	2.5	12 - 210	8
GREX-PLUS [12]	(2030)	1.2	2 - 20	50

1.2 High Dispersion Spectroscopy Infrared Astronomy

Mid-infrared high-dispersion spectroscopy from space offers many advantages. First, space telescopes are positioned above the Earth's atmosphere, eliminating the need to consider absorption and scattering effects caused by the atmosphere. This is particularly important for infrared observations because water vapor and oxygen in the Earth's atmosphere strongly absorb infrared radiation. By avoiding atmospheric absorption due to water vapor, observations in the mid-infrared range become possible, significantly improving observational sensitivity. Additionally, high spectral resolution enables the acquisition of detailed information about celestial objects, such as their Doppler shift, chemical composition, temperature, and density.

These advantages allow us to explore new scientific fields. One example is the observation of the H_2O snowline in protoplanetary disks. Figure 1.3 illustrates a conceptual diagram of the evolutionary process from a protoplanetary disk to a planetary system. A protoplanetary disk is a rotating circumstellar disk composed mainly of gas and dust that forms around a newly born star. In the region close to the central star, water molecules in the disk are heated by radiation from the star and exist as water vapor. In contrast, in the outer regions farther from the central star, water molecules exist as ice. The boundary that separates these two regions, where water transitions between vapor and ice, is called the H_2O snowline. Within the protoplanetary disk, materials undergo repeated collisions and coalescence, eventually forming planets. Inside the H_2O snowline, the planet's core is primarily composed of dust. Outside the H_2O snowline, both dust and ice contribute to the formation of the planetary core. As a result, planets forming beyond the H_2O snowline develop larger cores than those forming inside the snowline. These cores continue to grow and gradually capture surrounding gas. The larger planetary cores outside the H_2O snowline capture more gas compared to the smaller planetary cores inside the snowline. Consequently, rocky planets form inside the H_2O snowline, while giant gas planets form outside it. This evolutionary model is known as the Kyoto Model [13].

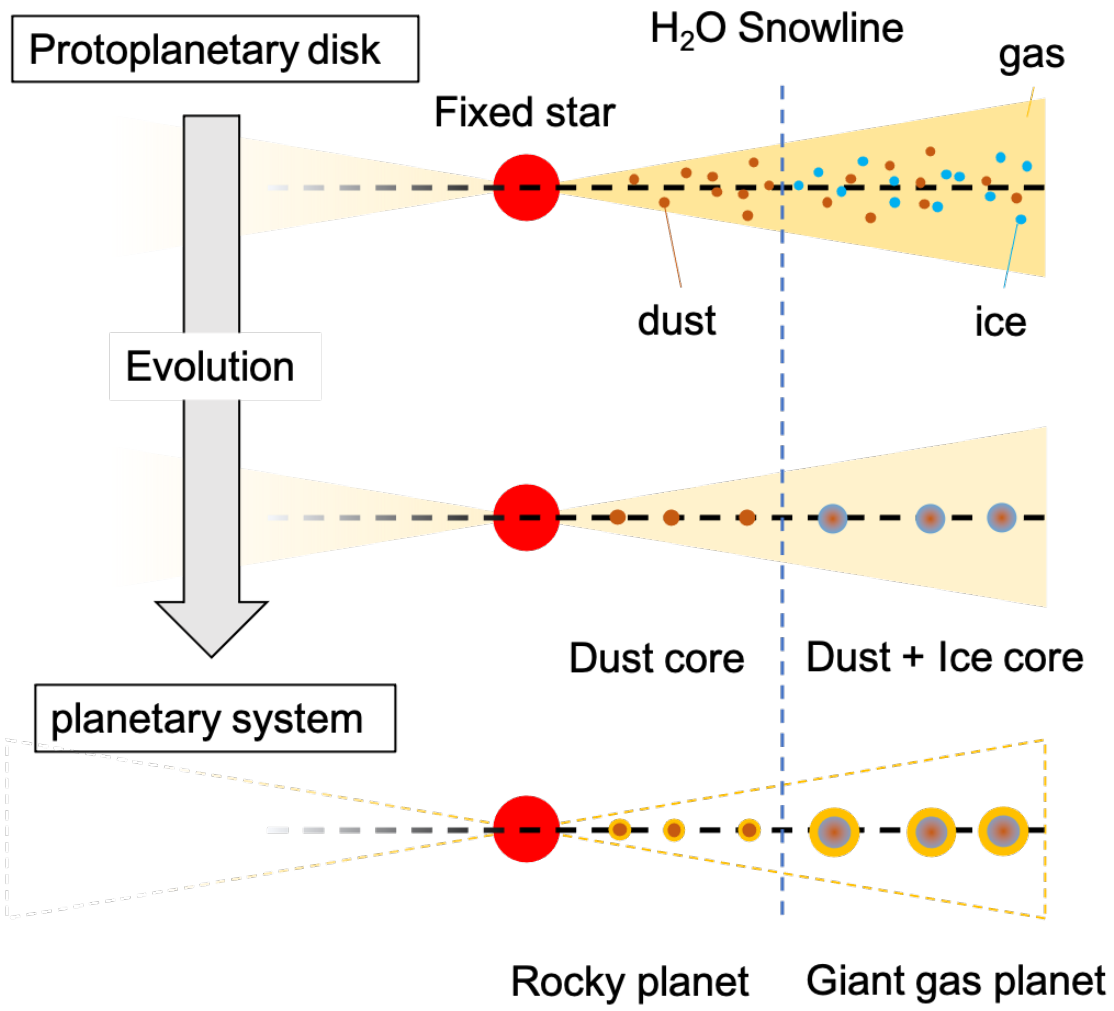

Figure 1.3: Conceptual diagram of the evolutionary process from a protoplanetary disk to a planetary system

Recently, some studies have suggested that the position of the H_2O snowline may shift over time during planetary system evolution. Determining the location of the H_2O snowline is crucial for understanding planetary system formation [14].

Mid-infrared high-dispersion spectroscopy is a useful method for observing the H_2O snowline in protoplanetary disks. Figure 1.4 shows a simulation result of the water vapor distribution in a T Tauri star's protoplanetary disk. The horizontal axis represents the radial distance r from the central star, while the vertical axis represents the height Z above the disk midplane, normalized by r. The color scale indicates the abundance of water vapor, with red representing higher concentrations.

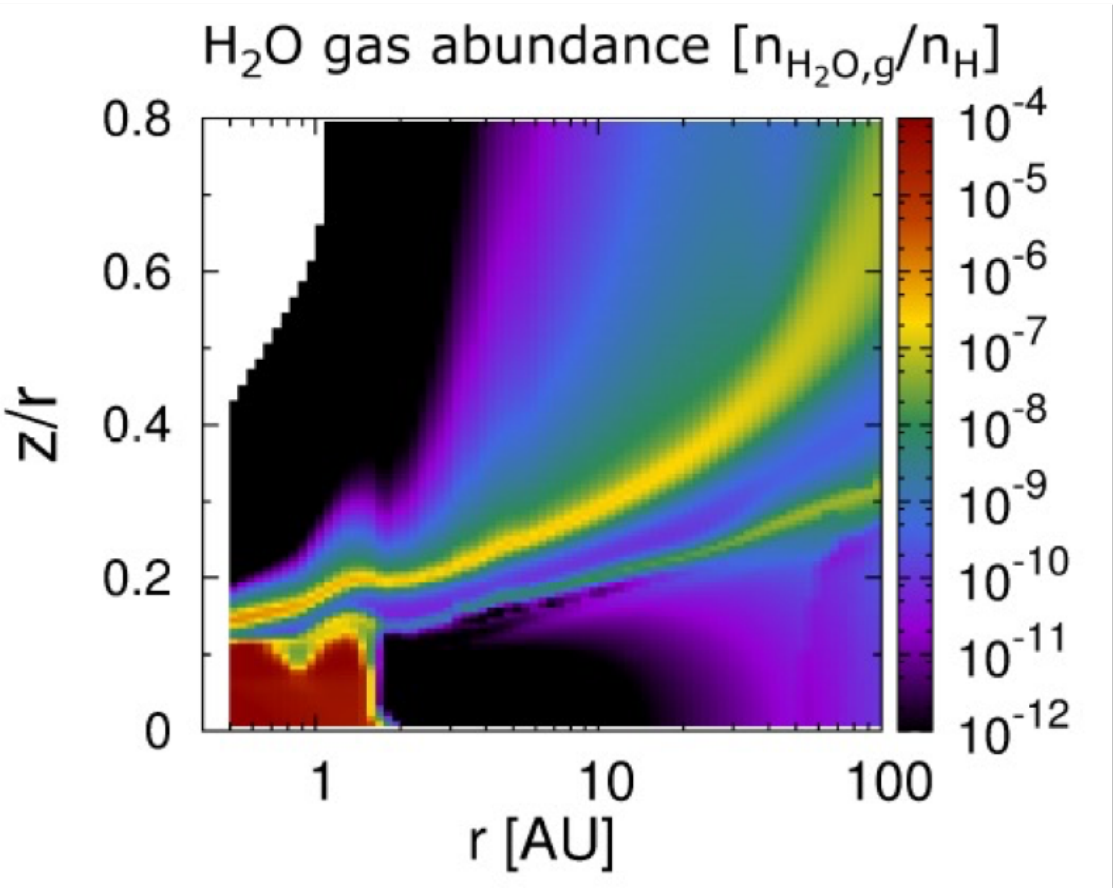

Figure 1.4: Simulation result of the water vapor distribution in a T Tauri star's protoplanetary disk [15, 16]

The simulation results show that water vapor is abundant in the surface layers of the protoplanetary disk and in the inner region within 2 au. In contrast, beyond 2 au, the water vapor abundance drops sharply. This boundary represents the H_2O snowline. To detect molecular components inside the snowline, it is necessary to observe water spectral lines that can penetrate the disk (i.e., spectral lines with small Einstein A coefficients). For example, model calculations suggest that the location of the H_2O snowline can be identified by observing the Doppler shift of the 17.754 μm H_2O emission line caused by rotational motion.

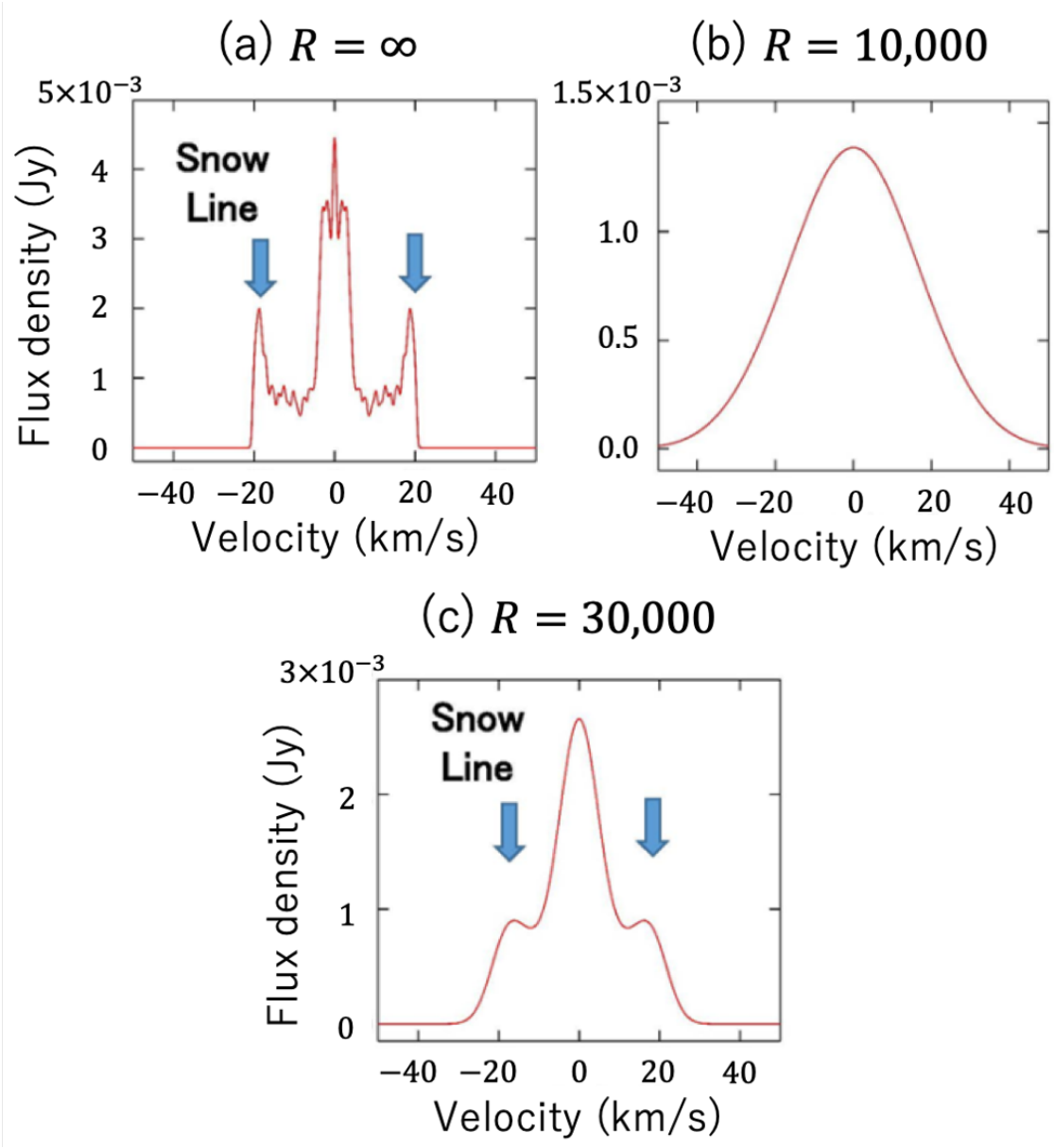

Figure 1.5: Simulation of Doppler shift of H_2O gas emission lines due to rotational motion. Velocity profiles of H_2O gas emission lines at (a) infinite wavelength resolution, (b) wavelength resolution R = 10,000, and (c) wavelength resolution R = 30,000 (Notsu et al. 2016 [15]; Nakagawa in prep, partial change).

Figure 1.5 illustrates the Doppler shift of the H_2O emission line due to rotational motion. Figure 1.5 (a) shows the Doppler shift profile of the H_2O emission line with infinite spectral resolution. It suggests that the H_2O snowline exists at positions corresponding to velocities of ± 20 km/s. As shown in Figure 1.5 (b), at a spectral resolution of $R \sim 10,000$, the profile of the H_2O snowline cannot be resolved. However, at $R \sim 30,000$ in Figure 1.5 (c), the velocity resolution reaches 10 km/s, allowing the profile of the H_2O

snowline to be resolved.

Despite the many advantages of mid-infrared high-dispersion spectroscopy, it has not yet been fully realized. One of the main challenges is the increasing size of spectrometers as wavelength resolution improves. In general, high-resolution spectrometers become larger, making it difficult to design a compact spectrometer with high resolution that can be installed on a space telescope. Additionally, infrared observation instruments require cooling of the entire system to avoid thermal noise caused by background infrared radiation. When the spectrometer is large, cooling the entire system is not practical. Addressing these challenges is essential for the successful implementation of mid-infrared high-dispersion spectroscopy in space.

The key technology to overcome these challenges is the immersion grating, which will be discussed in the next section 1.3.

1.3 Immersion grating

An immersion grating is an optical element that can reduce the size of the spectrometer to $1/n$ ($1/n^3$ in volume, n: refractive index) compared to conventional diffraction gratings (see Figure 1.6). This is because passing light through a high-refractive-index medium allows for an effectively longer optical path length L_{IG} compared to L_{air} in air by a factor of n. So far, there have been demonstrations of immersion gratings for the near-infrared, such as the Si immersion grating used in IGRINS (Immersion GRating INfrared Spectrometer) [17, 18] and the Ge immersion grating used in GIGMICS (Germanium Immersion Grating Mid-Infrared Cryogenic Spectrograph) [19]. However, a development of mid-infrared (beyond 10 μm) immersion grating has not yet been reported.

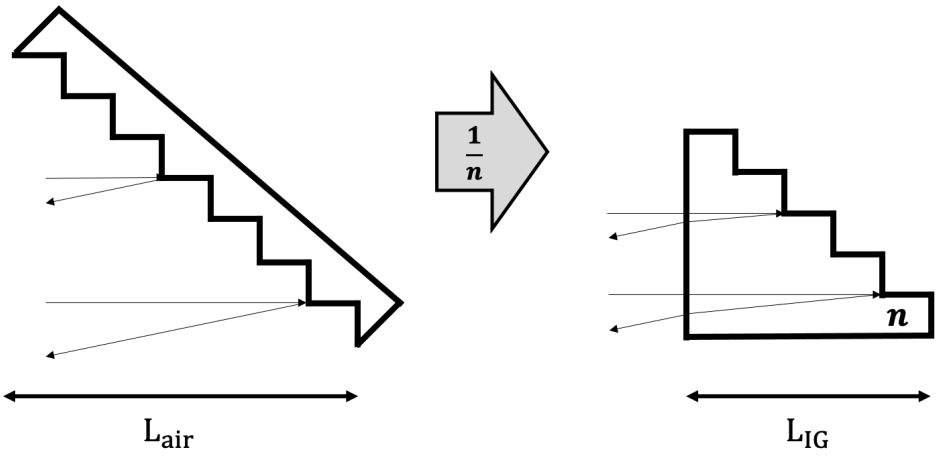

Figure 1.6: Conceptual diagram of conventional diffraction grating on the left and immersion grating on the right

The material for the immersion grating requires a high n and transmittance in the observation wavelength range (10–18 μm) and at the operating temperature ($<$ 20 K). Additionally, it must have sufficient strength for microfabrication. From this perspective, CdZnTe was chosen as the material for immersion gratings in the mid-infrared range [20]. However, there is no literature value for n of CdZnTe in the observation wavelength range (10–18 μm), and only estimated values calculated from the transmittance T and absorption coefficient κ were available. In Sarugaku et al. (2017), the absorption coefficient of CdZnTe in the range of 2 to 13 μm was determined from transmittance T measurements of CdZnTe flat samples with different thicknesses t at room temperature. Considering the sample thickness t, n, and absorption coefficient κ, the transmittance T can be expressed using Equation 1.1 as follows:

$$T = \frac{(1-R)^2 \exp(-\kappa t)}{1 - R^2 \exp(-2\kappa t)} \tag{1.1}$$

where $R = \frac{(n-1)^2}{(n+1)^2}$ is the Fresnel reflection at the sample surface. From R and Equation 1.1, the absorption coefficient κ can be expressed as follows:

$$\kappa = -\frac{\ln(T_1/T_2)}{|t_1 - t_2|} \tag{1.2}$$

where T_1 and T_2 are the transmittances of samples with thicknesses t_1 and t_2, respec-

tively. Thus, using Equations 1.1 and 1.6, n can be estimated from the transmittance T and the absorption coefficient κ. In this way, n of CdZnTe at room temperature in the range of 2 to 13 μm was estimated. Additionally, for wavelengths longer than 13 μm, n of CdZnTe is estimated based on n of CdTe. This is because CdTe and CdZnTe both belong to the same cubic crystal system, and $Cd_{0.98}Zn_{0.04}Te$, which is CdTe with 4% of Cd replaced by Zn, has a chemical formula similar to CdTe.

An accurate n for CdZnTe is crucial for determining the wavelength dispersion capability of the transmission-type dispersive element, the immersion grating. It is also essential for the detailed design of the spectrometer's optical system to achieve high efficiency at specific wavelengths. This accuracy is required because of the following reasons. First, the maximum value of the spectral resolution R of the immersion grating at wavelength λ is given by Equation 1.3 [21]. In this way, it is necessary to know the absolute value of n to determine the wavelength resolution.

$$R_{\max} = \frac{\lambda}{(\Delta\lambda)_{\min}} = \frac{2n\phi \tan\theta_{\mathrm{bla}}}{\lambda} \tag{1.3}$$

where n is the refractive index, Φ is the diameter of the collimated beam, and θ_{bla} represents the blaze angle of the diffraction grating under the Littrow configuration. The Littrow configuration of a diffraction grating is a setup that maximizes the intensity of the diffracted light. In this configuration, the incident light and the diffracted light are at the same angle. This setup allows for the maximization of the diffracted light intensity, making it an efficient method for measuring wavelengths, particularly in spectral analysis.

Additionally, for achieving high efficiency at a target wavelength, the detailed design of the spectrometer's optical system is essential. The following describes the required precision for refractive index measurements. Figure 1.7 (left) shows an image of the spectrum dispersed by the diffraction grating on the detector surface. A smaller diffraction order m corresponds to longer wavelengths, while a larger m corresponds to shorter wavelengths. As shown in Figure 1.7 (right), the center of the FSR $\Delta\lambda$ is the wavelength at which the diffraction efficiency peaks for that order, known as the blaze wavelength λ_{bla}. The goal is to design the optical system so that the target wavelength matches the

blaze wavelength $\lambda_{\rm bla}$ with 10% accuracy, and to achieve a diffraction efficiency of 90% or higher at the target wavelength on the spectrometer's detector surface.

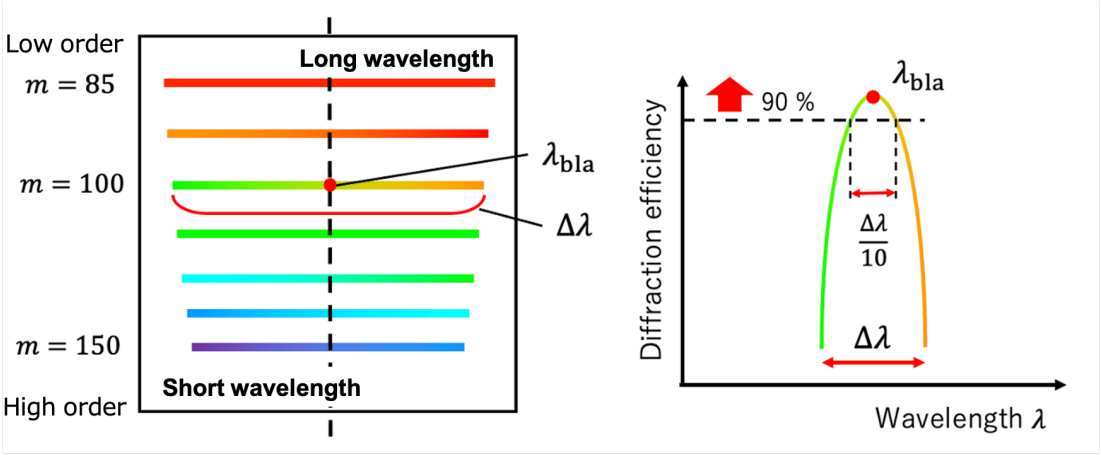

Figure 1.7: Image of the spectrum dispersed by the diffraction grating on the detector surface (left), and Image of the diffraction efficiency's wavelength dependence for the FSR (right).

The blaze wavelength $\lambda_{\rm bla}$ and the free spectral range $\Delta\lambda$ are given by Equation 1.4 and 1.5, respectively.

$$\lambda_{\rm bla} = \frac{2n\sigma \sin\theta_{\rm bla}}{m} \tag{1.4}$$

$$\Delta\lambda \sim \frac{\lambda_{\rm bla}}{m} \quad (m \gg 1) \tag{1.5}$$

where σ is the grating pitch, and m is the diffraction order.

Two applications of immersion gratings can be listed. One is GREX-PLUS/HRS (Galaxy Reionization EXplorer and PLanetary Universe Spectrometer/High-Resolution Spectroscopy), and the other is the ground demonstration spectrometer for GREX-PLUS/HRS. For detailed specifications of each spectrometer, please refer to Section 1.4.1.

The observation target wavelength of GREX-PLUS/HRS is the H_2O gas emission line at 17.754 μm. The diffraction order m is assumed to be approximately $m \approx 100$ due to the constraints of the detector pixel format. The required precision for refractive index measurements is examined to constrain the blaze wavelength $\lambda_{\rm bla}^{\rm GRX\text{-}PLUS}$ within 10% of

the FSR peak. Using the equation, the bandwidth of the FSR is $\Delta\lambda = 0.17754\,\mu m$. This means the blaze wavelength must be within $\Delta\lambda/10 = 0.01775\,\mu m$. From the equation, it can be seen that the blaze wavelength and n are in a proportional relationship. Considering that there are errors in the diffraction grating pitch σ and blaze angle θ_{bla}, the required precision for n is further reduced, leading to $\Delta n_{\text{req}}^{\text{GRX-PLUS}} < 1.8 \times 10^{-3}$. Similarly, when examining the required precision for refractive index measurements for the ground demonstration spectrometer of GREX-PLUS/HRS, the required precision is $\Delta n_{\text{req}}^{\text{for testing}} < 0.8 \times 10^{-3}$ (with diffraction order $m = 150$ and observation target wavelength 12.453 μm). Therefore, the required precision for refractive index measurements is set as $\Delta n_{\text{req}} < 10^{-3}$.

Additionally, an important parameter for immersion gratings is the absorption coefficient κ. Unlike conventional diffraction gratings, immersion gratings allow light to pass through the medium, leading to light loss due to absorption. For an immersion grating with length L_{IG}, if the absorption loss is set to $A_{\text{abs}} < 10\%$, the absorption coefficient κ can be determined by following Equation 1.6.

$$\kappa = -\frac{\ln(1 - A_{\text{abs}})}{L} < 0.01 \left(\frac{L}{85\,\text{mm}}\right)^{-1} \text{cm}^{-1} \quad . \tag{1.6}$$

For the GREX-PLUS/HRS IG with $L = 85\,\text{mm}$, the required absorption coefficient is $\alpha < 0.01\,\text{cm}^{-1}$ (at operating temperature).

When measuring the absorption coefficient κ, multiple reflections within the sample can interfere with accurate measurement. Li et al. 2024 [22] developed a model for deriving the absorption coefficient κ of CdZnTe, considering the effects of multiple reflections (Equation 1.7).

$$\kappa = -\frac{1}{t} \ln \left(\frac{(1 - R)^2 + 4R^2\tau_{\text{sum}}}{2R^2} \right), \tag{1.7}$$

κ: absorption coefficient, t: sample thickness, R: Fresnel surface reflectance, τ_{sum}: transmittance calculated using an infinite Fresnel reflection model.

Equation 1.7 is used to determine the absorption coefficient κ from the transmittance

τ_{sum} of two samples with different thicknesses. τ_{sum} refers to the transmittance calculated using the infinite Fresnel reflection model. Although Equation 1.7 can also be used to estimate n, it is difficult to minimize the estimation error of n due to the limited measurement accuracy of τ_{sum}. Therefore, independent measurement of n is important.

1.4 Candidates for immersion grating

1.4.1 GREX-PLUS

GREX-PLUS is a medium-class mission strategically implemented by JAXA, aimed for launch in the 2030s (Figure 1.8). It is a cryogenic space telescope with an aperture of 1.0 m, cooled to a temperature of 50 K, and equipped with two scientific instruments. One is a wide-field camera covering the 2–10 μm wavelength range, and the other is a high-dispersion spectrometer with a wavelength range of 10–20 μm and a spectral resolution of $>$ 25,000 (Table 1.3). In particular, the high-dispersion spectrometer has a spectral resolution of $R > 25,000$, which is 10 times higher than that of JWST ($R > 3,000$) (Table 1.3, Figure 1.9, [23]). The observation period is expected to last one year (to be confirmed) after launch, and it will observe from either a Sun-Earth L_2 orbit or an Earth-trailing orbit. This telescope aims to enhance our understanding of the formation and evolution of galaxies and planetary systems.

The primary goal of GREX-PLUS in galaxy formation and evolution studies is to discover the rare, bright "early galaxies" in the early universe and to observe "building blocks," which have a mass one-hundredth that of the Milky Way, across 95% of cosmic history. To achieve this, the GREX-PLUS wide-field camera will conduct surveys in the 2–10 μm wavelength range with a sensitivity 100 times higher and a survey area 1000 times wider than previous missions.

In planetary system formation and evolution studies, the primary objective is to determine the location of the H_2O snowline in the midplane of protoplanetary disks within the Milky Way and to elucidate the formation process of planetary systems, including rocky planets and giant gas planets [15, 16] (see Section 1.2). Additionally, GREX-

PLUS will contribute to planetary astrobiology research by observing organic molecules in protoplanetary disks and atmospheric molecules in both Solar System and extrasolar planets. This will advance our understanding of the synthesis of life-forming materials, planetary atmospheric structures, and the origins of oceans on rocky planets. To achieve these objectives, the GREX-PLUS high-dispersion spectrometer, with its unique spectral resolution of $> 25{,}000$ in the 10–20 μm wavelength range, is essential. The development of CdZnTe immersion gratings for the mid-infrared range is crucial for realizing this high-dispersion spectrometer. As shown, GREX-PLUS aims to address a wide range of scientific issues.

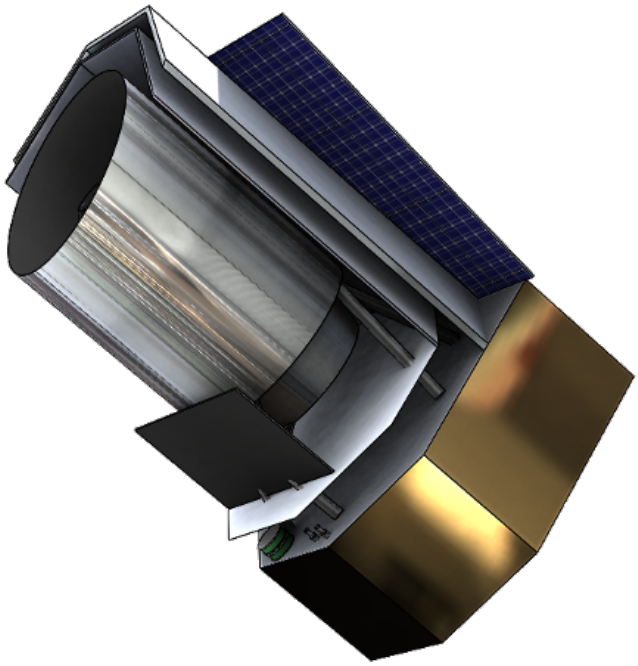

Figure 1.8: Appearance of GREX-PLUS [24]

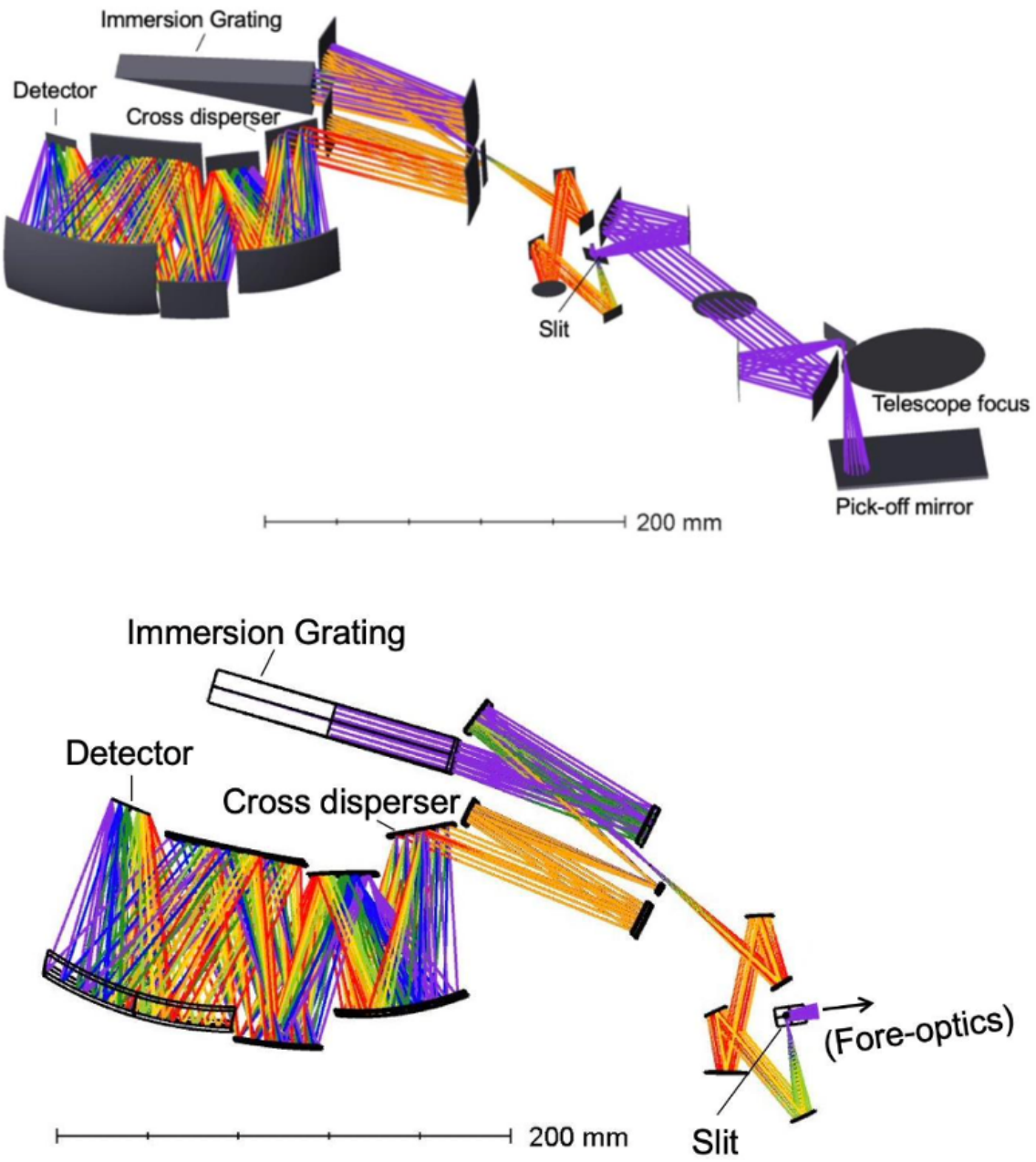

Figure 1.9: GREX-PLUS/HR optics design proposal. The top panel shows the layout of the optical system, and the bottom panel shows the design solution for the rear optical system [12].

Table 1.2: Specifications of GREX-PLUS [24]

Launch	Target year	2030s
Spacecraft	Mass	1,390 kg
Instruments	Wide-field camera	2–10 μm
	High-dispersion spectrometer	10–18 μm
Telescope	Aperture	1.0 m
	Temperature	< 50 K
Cooling system		Cryocoolers and radiative cooling

Table 1.3: Specifications of GREX-PLUS/HRS [24, 25]

Wavelength range	10–18 μm
Spectral resolution [$\lambda/\Delta\lambda$]	$> 25{,}000$
Detector	Si:As BIB detector, 1k×1k
Pixel scale [arcsec pix^{-1}]	1.5
Field-of-view [arcsec^2]	8.2×3.5
Continuum sensitivity [mJy]†	4.2 / 5.0
Line sensitivity [10^{-20} W m^{-2}]†	3.4 / 4.1

1.4.2 Mid-infrared high-dispersion spectrometer for ground-based observation

The mid-infrared high-dispersion spectrometer for ground-based observation, currently being studied under the leadership of Nakagawa, Baba, and Hirahara, is one of the potential instruments for installing an immersion grating. This spectrometer is designed to demonstrate the performance of the CdZnTe immersion grating, and its specifications are shown in Table 1.4.

Table 1.4: Specification of the mid-infrared high-dispersion spectrometer for ground-based observation

Parameter	**Details**
Telescope	1.3 m ISAS telescope
Wavelength Range	N-band (7.5–13.5 μm)
Typical Seeing Angle	Approximately 2 arcsec
Target Lines	H_2O 13_{76}–12_{49} at 12.453 μm
Detector	Raytheon 512×412 Si:As (30 μm pixel^{-1})

1.5 Refractive Index Measurement Systems of the World

There are many refractive index measurement systems in the world. Table 1.5 lists the refractive index measurement systems that meet the following conditions:

- They use the same minimum deviation method as the one used in this measurement.
- The measurement wavelength includes infrared.
- They have a cooling system and allow for temperature selection.

Regarding the measurement wavelength, this study, the Spectrometer NRI-200, and Liao Sheng et al. (2011) all reach the 10 μm range. However, the Spectrometer NRI-200 only reaches a cooling temperature of 233 K, and Liao Sheng et al. (2011) only reaches 100 K, neither reaching cryogenic temperatures. About the measurement temperature, this study, CHARMS NASA GSFC [26] and Simon G. Kaplan et al. 2002 [27] reach the 10 K range. However, they have measurement wavelengths in the near infrared range. CHARMS was developed for JWST and has also been used to measure optical elements for ESA's Euclid [28]. A key feature of this system is that the light source and detector can be placed inside the shroud to improve measurement accuracy. Another advantage is that α can be measured during cooling. Since some materials have crystal anisotropy, measuring α at low temperatures is important. Simon G. Kaplan et al. have the advantage of measuring n over a continuous wavelength range by using a Fourier-transform infrared (FTIR) spectrometer as the detector.

Table 1.5: Comparison of Wavelength and Temperature Range

Study	Wavelength (μm)	Temperature (K)
This Work	0.365, 10.6 – 17.1	12.6 – 300
Yamamuro et al. 2006 [29]	0.365 – 3.5	80 – 293
Shimadzu GMR-1D[30]	0.254 – 2.325	233 – 353
Spectrometer NRI-200 [31]	0.4 – 14	233 – 353
CHARMS NASA GSFC [26]	0.4 – 5.6	15 – 340
Liao Sheng et al. 2011 [32]	1.0 – 12	100 or 300
Simon G. Kaplan et al. 2002 [27]	1.0 – 5.4	10 – 295

1.6 Minimum deviation method

The representative methods for measuring n of solid materials include the minimum deviation method, critical angle method, V-block method, and ellipsometry method. In this study, we adopted the minimum deviation method, which allows for the most accurate measurements and is regarded as a standard measurement technique among optical equipment manufacturers. The minimum deviation method is the only technique capable of measuring the absolute refractive index n_{abs}. Other methods measure relative refractive index measurements compared to standard prisms. On the other hand, the minimum declination method can measure absolute refractive indices, which is another reason for using this method.

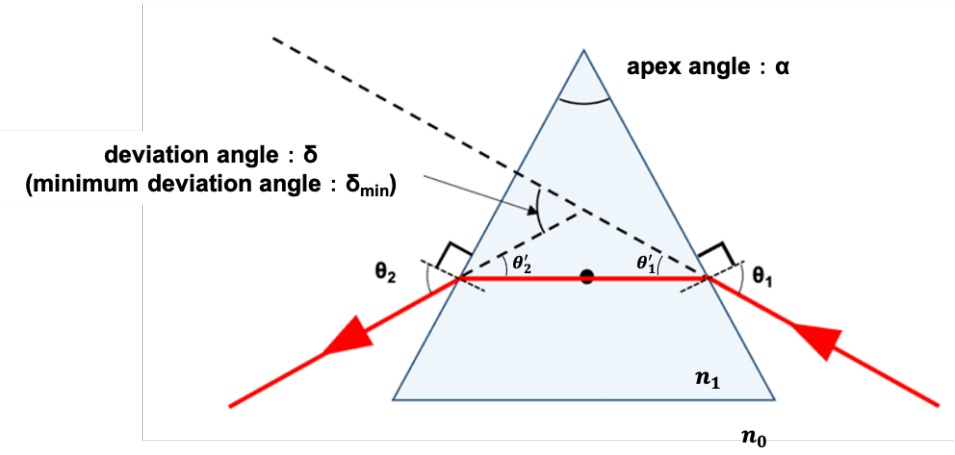

Figure 1.10: Refraction of a monochromatic collimated beam through a prism. The symbol n_0 is the refractive index of vacuum, and the symbol $n_0 = 1$. n is the refractive index of the prism's material.

When determining n of a material using the minimum deviation method, it is necessary to shape the material into a prism. Figure 1.10 shows monochromatic collimated light entering a prism with an apex angle α and n at an incident angle θ_1. After refraction, the light exits at an exit angle θ_2. The angle between θ_1 and the exit angle θ_2 is the deviation angle δ. Using geometric relations (Equation 1.8) and Snell's law, δ can be determined from θ_1, the exit angle θ_2, and α of the prism as shown in Equation 1.9.

$$\delta = \theta_1 + \theta_2 - \alpha \tag{1.8}$$

$$\delta = \theta_1 - \alpha + \arcsin\left[n \sin\left[\alpha - \arcsin\left(\frac{\sin\theta_1}{n}\right)\right]\right] \tag{1.9}$$

The minimum value of δ is referred to as the minimum deviation angle $\delta_{\min}$. When $\frac{d\delta}{d\theta_1} = 0$, δ becomes equal to $\delta_{\min}$. n can then be determined using $\delta_{\min}$ and α of the prism through Equation 1.10.

$$n = \frac{\sin\left(\frac{\delta_{\min}+\alpha}{2}\right)}{\sin\left(\frac{\alpha}{2}\right)}, \tag{1.10}$$

Therefore, we first optically measure α of the prism with precision exceeding the mechanical processing accuracy. Then, we find $\delta_{\min}$ by varying θ_1.

1.7 The Purpose And Outline Of This Thesis

This study has two issues. First, there are no actual measurements of n of CdZnTe at cryogenic mid-infrared temperatures, and it is highly indefinite. Second, there is the absence of a measurement system to measure n at cryogenic temperatures at the wavelength of mid-infrared.

Therefore, this paper has three objectives. First, to measure n of CdZnTe at cryogenic temperatures in the mid-infrared wavelength region with $\Delta n_{\mathrm{req}} < 10^{-3}$. Second, to produce a high-precision cryogenic mid-infrared refractive index measurement system to perform the above measurements. Finally, to verify the impact of the measurement results of this study on the design of CdZnTe immersion gratings.

This paper consists of five sections. Following the introduction in Section 1, Section 2 describes the experimental setup. Section 3 presents the experimental methods and results. Section 4 discusses the findings of this study. The conclusions are summarized in Section 5.

Chapter 2

EXPERIMENTAL SETUP

In this chapter, we explain the a gonio-type refractometer GMR-1 which is the foundational component of the measurement system, along with the main optical system, cooling system, and motorized rotation stage system. Additionally, we describe the novelty and originality of the measurement system. For other components, refer to the appendix.

2.1 Angle measurement system

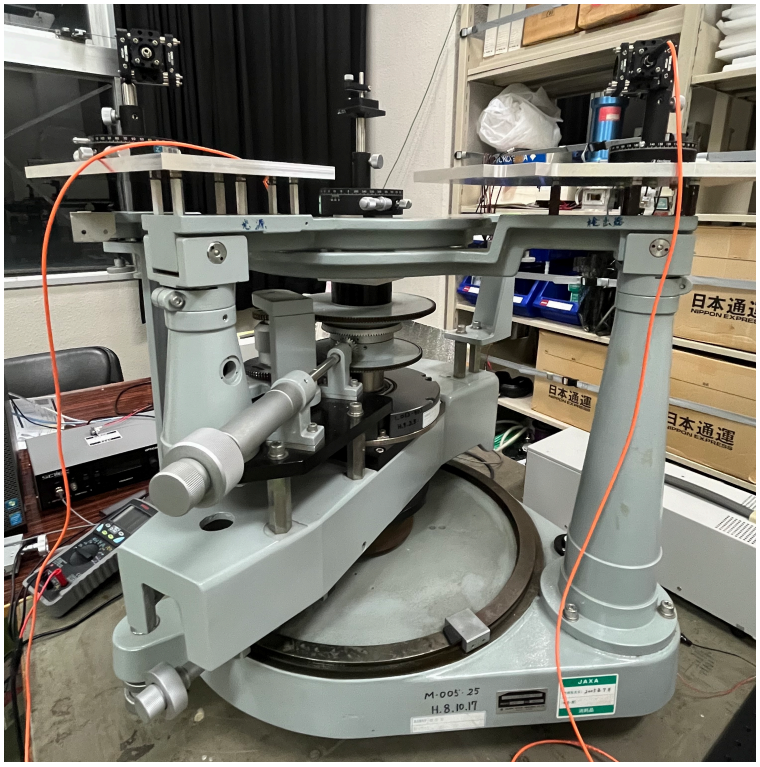

Figure 2.1: Gonio-type refractometer GMR-1 (Shimadzu Corporation)

We customized a gonio-type refractometer [33], the GMR-1, an initial model of high-precision angle measurement stage from Shimadzu Device Corporation's GMR series produced by Kalnew-Iida Works (Figure 2.1). At the center of the refractometer, is a rotating sample stage where a prism sample is placed. There are two platforms for placing the optical system: one is a fixed stage, and the other is a movable stage. The movable stage can rotate coaxially with the rotating sample stage. It is equipped with a precise angle encoder (angular resolution of 10^{-4} degree), which can measure the rotation angle of the movable stage. Moreover, it allows the rotation of the movable stage to be synchronized with that of the rotating sample stage. In this case, when the movable stage rotates by θ_{msta}, the rotating sample stage rotates by $\theta_{\mathrm{msta}}/2$. This function enables precise measurement of the rotation angle of the sample stage .

2.2 Optical system

We constructed a visible light measurement system for angle calibration and apex angle measurement and a cryogenic infrared measurement system for deviation angle measurement.

2.2.1 Visible Light Measurement System for Angle Calibration and Apex Angle Measurement

Light source

The light source for the visible light measurement system is a wavelength of 635 nm diode laser (Thorlabs, CPS635R). The beam size is 2.9 mm in diameter, and its power stability is within 2% over 8 hours. This beam is focused by a lens (Thorlabs, LA1131-A) and introduced into a fiber with an aperture diameter of 105 μm (see the optical fiber).

Optical fiber

The apex angle measurement of a prism in this refractometer is achieved by illuminating a collimated beam perpendicularly to the prism surface using the auto collimation method (see section 3.3). At this time, the beam from the light source and the beam reflected back from the prism surface travel the same optical path, so the returning beam is usually introduced to the detector via a beam-splitter. To simplify the optical alignment procedure, an optical fiber coupler (Thorlabs, TM105R5S2B) was adopted. The aperture diameter of the coupler is 105 μm, and the numerical aperture (NA) is 0.22 $\pm$ 0.02. The core material is Low OH, and the wavelength range between 400 and 2,200 nm. Additionally, the coupler has a 50:50 coupling ratio, allowing for even distribution of light.

We will explain the light branching process. As shown in Figure 2.2, for example, when light enters port 1 of this fiber, it is output from ports 3 and 4 in a 50:50 ratio. This splitting ratio remains the same regardless of which port the light is introduced from.

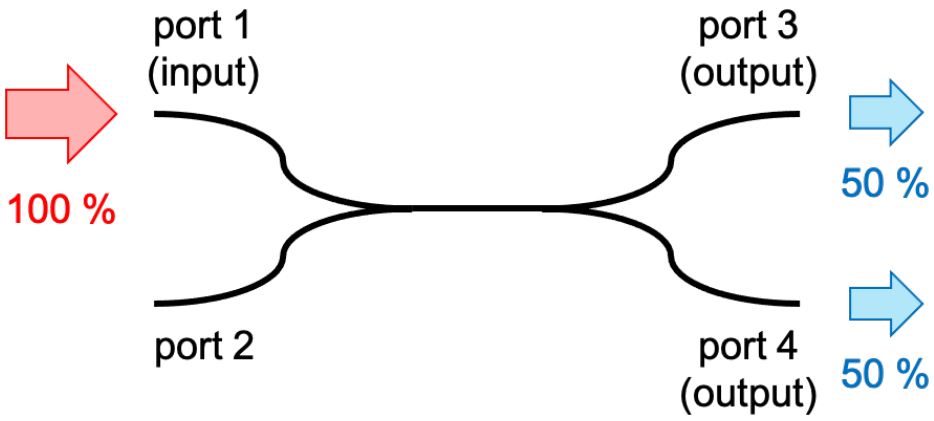

Figure 2.2: The coupling ratio of the optical fiber coupler

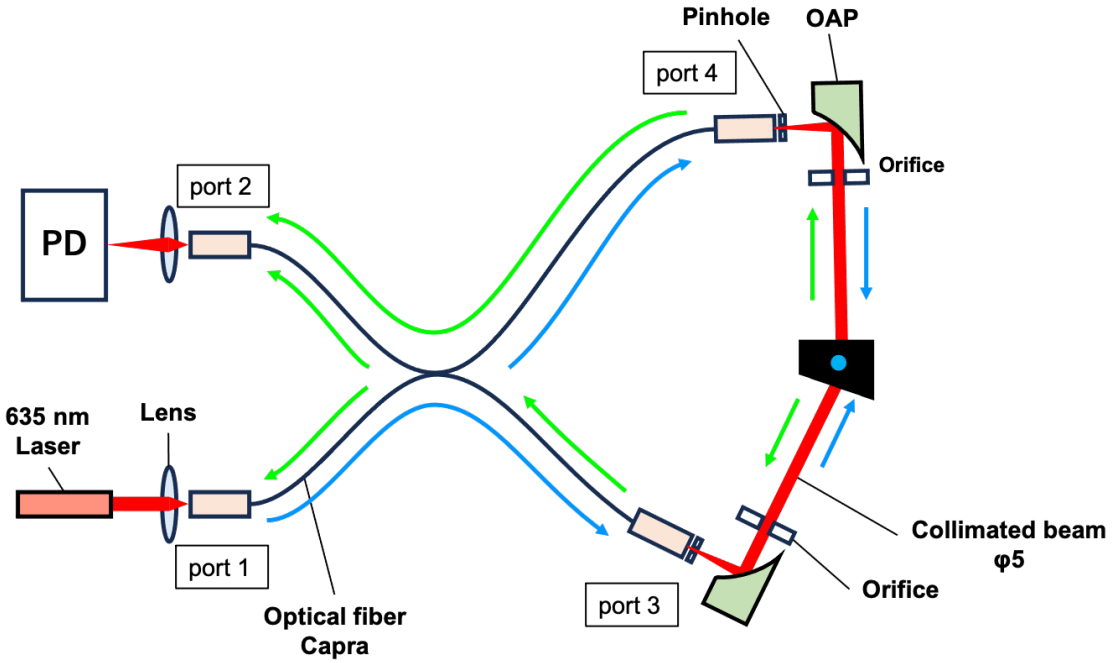

Figure 2.3: Schematic setup for auto-collimation measurement using the fiber coupler, illustrating the light branching by the fiber coupler

Using this property, in this study, the fiber is used in place of a beam splitter to simplify the auto-collimation measurement. Figure 2.3 shows a schematic setup for auto-collimation measurement using the fiber coupler, illustrating the light branching by the fiber coupler. The light emitted from the laser is focused by a lens and enters port 1 of the fiber coupler. The light entering the fiber (shown by the blue arrow) is split into a 50:50 ratio at the branching point of the coupler. The split light is transmitted to ports

3 and 4, and after being emitted from the fiber ends, it is reflected by the OAP mirror (see section 2.2.1) and becomes collimated light. The collimated light is reflected at the side of the sample, and then reflected again by the OAP mirror, entering ports 3 and 4 (shown by the green arrows). The light entering ports 3 and 4 is transmitted through the fiber and is split again into a 50:50 ratio at the branching point. Half of the split light is transmitted to port 2, where the light is detected by a PD (see section 2.2.1) .

In this way, auto-collimation measurement is achieved without using a beam splitter. For the method of measuring α using auto-collimation, please refer to Section 3.3.

Off-Axis Parabolic Mirror (OAP mirror)

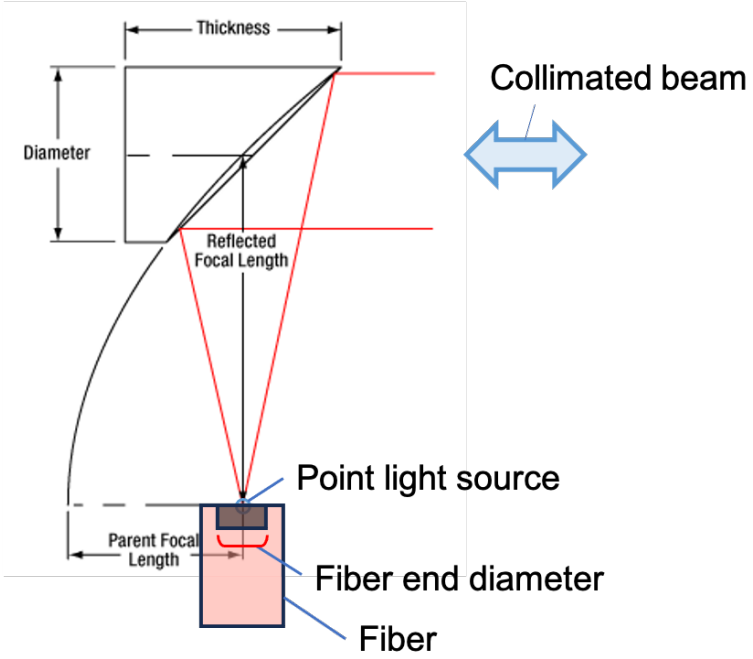

Figure 2.4: OAP mirror (Thorlabs, MPD019-M01) [34]

To collimate the measurement beam incident on the sample, an OAP mirror was used. By adopting a mirror system instead of a lens system and placing an SMA connector at the focal point of the OAP mirror, the optical systems for visible light and infrared light were unified. The OAP mirror has a parabolic reflective surface. As shown in Figure 2.4, this mirror achromatically (without chromatic aberration) focuses collimated beam or collimates a point light source. The off-axis angle between the focused beam and

the collimated beam is 90°. However, in the actual measurement setup, the light at the focal point of the OAP mirror is not a point light source but light with the diameter of the fiber end face. Therefore, the collimated beam generated by the OAP mirror is slightly expanded. To address this, an aperture was placed approximately 40 mm from the mirror to restrict the collimated beam. This helps to reduce the field of view seen from the mirror. Additionally, a 0.5 mm pinhole is placed in front of the fiber end face. The end face of the fiber for visible light is sufficiently small, but the end face of the fiber for infrared light is large, with a diameter of 1 mm. These two measures help to suppress the spreading of the collimated beam.

The focal length f of the OAP mirror (Thorlabs, MPD019-M01) used in this study is 24.5 mm. The diameter of the collimated beam R_{beam} was found to be 10.89 mm based on the following Equation 2.1. Since the CdZnTe prism to be measured has a size of 10 mm square, the collimated beam was narrowed to a diameter of 5 mm using an aperture.

$$R_{\mathrm{beam}} = 2 \times \mathrm{NA} \times f, \tag{2.1}$$

Furthermore, the OAP mirror is coated with gold, and its reflectance at the measurement wavelengths of 635 nm and 10–17 μm is over 90%. This OAP mirror is also used in the cryogenic infrared measurement system for deviation angle measurement.

Visible light detector

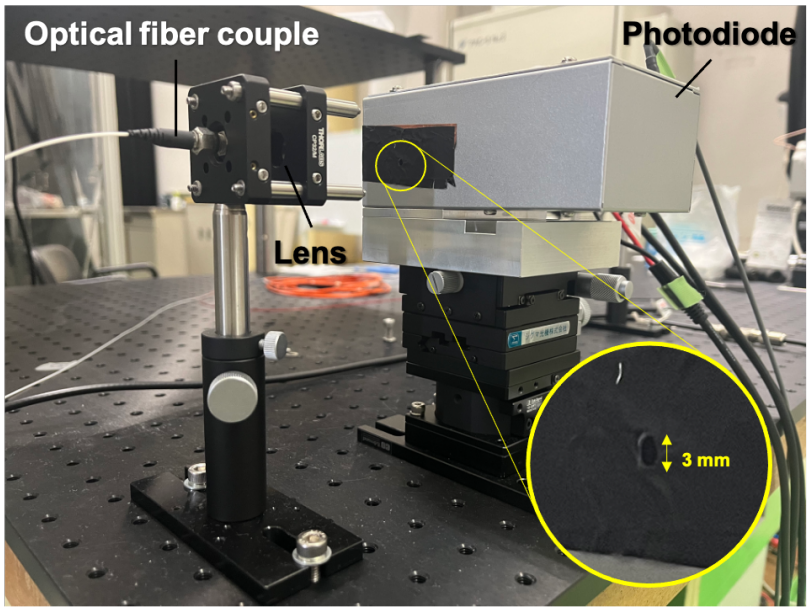

Figure 2.5: Visible light detector unit

Figure 2.5 shows the visible light detector of this measurement system. The light emitted from the optical fiber coupler is focused by the BK7 lens (LA1074-A-ML, Thorlabs) and reaches the detector surface of the 2.4 × 2.8 mm^2 sensor through a 3 mm hole in the aluminum box. The sensor uses a photodiode (Hamamatsu Photonics, S1133-14) as shown in the right part of Figure 2.6. There is a red LED above the photodiode, but it is not currently in use. By turning the variable feedback dial shown on the left of Figure 2.6, the feedback resistance can be adjusted from 10 kΩ to 447 MΩ, allowing for gain adjustment.

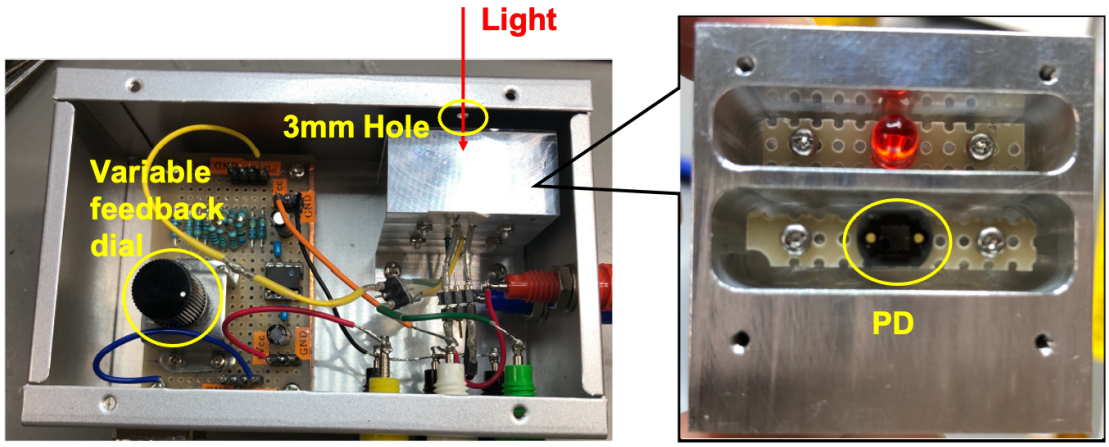

Figure 2.6: Inside of Visible light detector unit

2.2.2 Infrared Measurement System for Deviation Angle Measurement

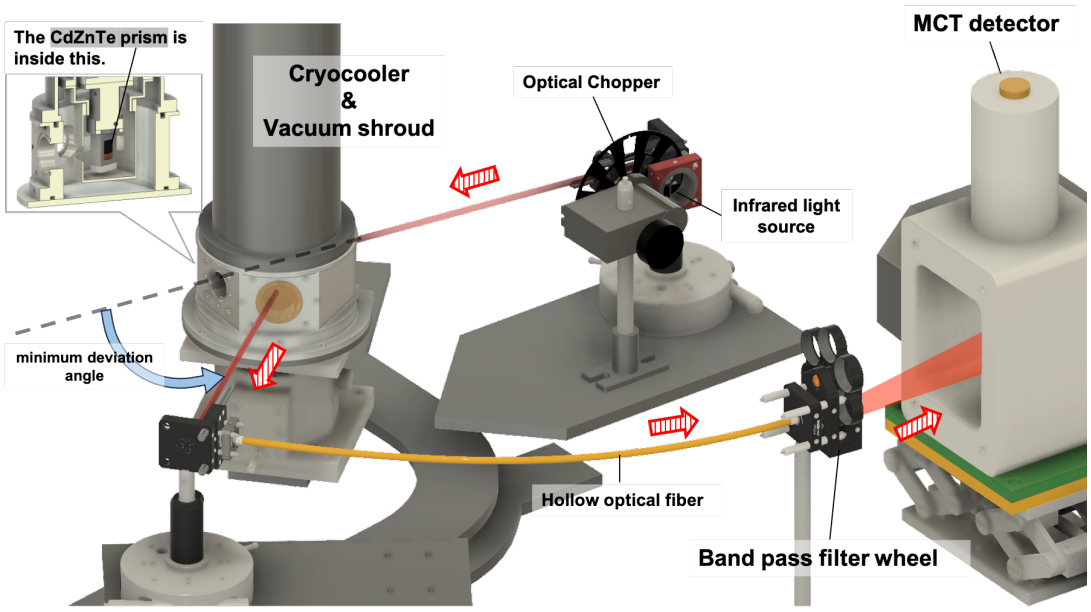

Figure 2.7: 3D configuration of the cryogenic infrared refractive index mesurement system. The red arrow indicates the direction of the measurement light. How this system is used in the apex angle measurement and the deviation angle measurement is shown in Figure 3.3 and 3.5, respectively.

On the fixed stage, a filament light source (the black body at approximately 1200 K), a collimator, and an orifice that generates collimated light with a diameter of 5 mm are

placed. Additionally, the fixed stage is equipped with a focusing system that guides light into a fiber, which transmits the light to a detector. There are two types of fibers and detectors: one for visible light and one for infrared light. In front of the infrared detector (MCT), a band-pass filter (BPF) is placed to select the measurement wavelength. A vacuum shroud and a mechanical refrigerator were added to the sample stage (details are explained in the next section). This measurement system allows n to be measured over a wide range, from visible to mid-infrared light (635 nm to 10.6 μm), and at temperatures from cryogenic to room temperature (4 to 300 K).

Light source

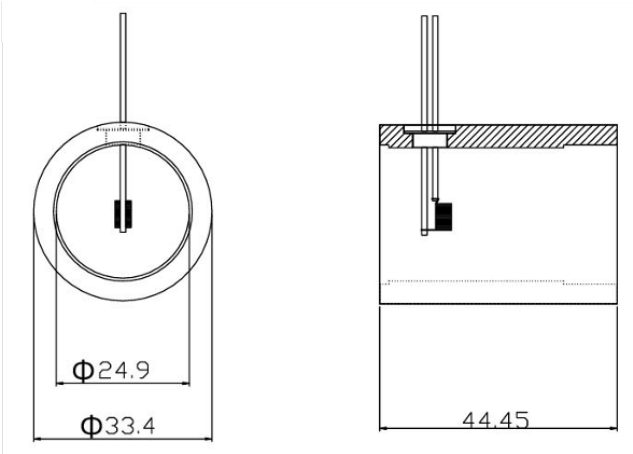

Figure 2.8: Design drawing of infrared light source (IR system, IRS-001C) [35]

The light source for the infrared measurement system is a filament light source (IR system, IRS-001C) (Figure 2.8). It operates at a voltage of 5 V, and the source temperature is approximately 1,200 K. Figure 2.9 shows the emission spectrum of the light source, which was approximated as a blackbody source.

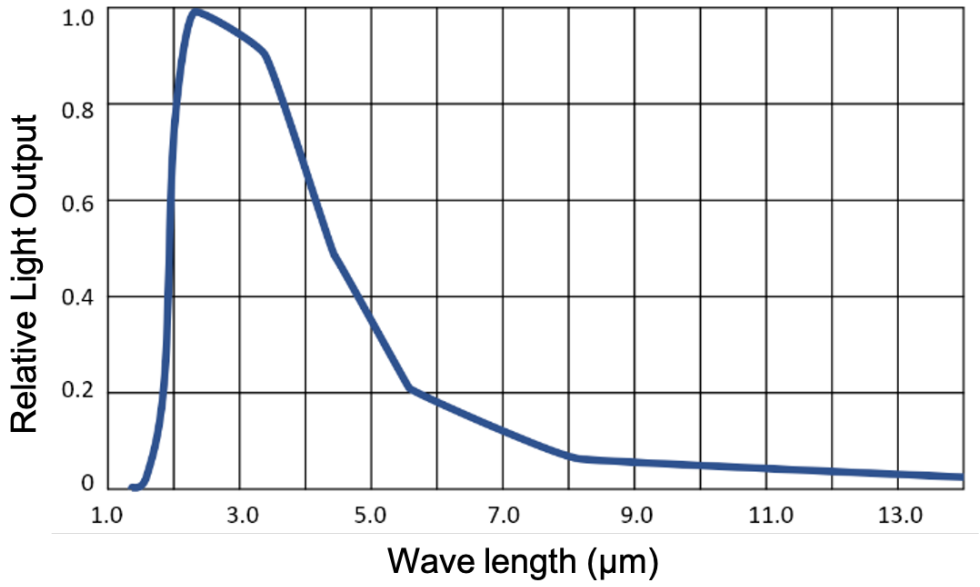

Figure 2.9: Emission spectrum of infrared light source (IR system, IRS-001C) [35]

Additionally, the infrared light source stabilizes after approximately 40 minutes, with a temporal stability of 1%. The filament size of the light source is approximately 5 mm × 3 mm, and a 500 μm pinhole is placed 5 mm in front to create a pseudo point light source. Since the light is incident on the entire surface of the OAP mirror with a focal length of 25.4 mm, the diameter of the collimated beam R_{beam} was approximately calculated to be 12.7 mm. This is the diameter of the OAP mirror. As with the visible light measurement system, an orifice was used to reduce the collimated beam diameter to 5 mm.

Infrared fiber

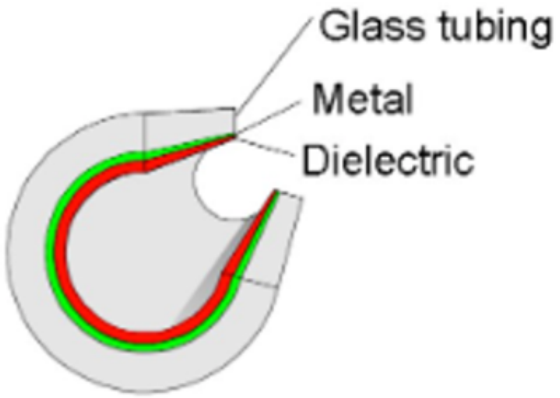

Figure 2.10: Stracture of hollow optical fiber(DOKO Engineering, IRS) [36]

We used a hollow optical fiber (DOKO Engineering) as shown in Figure 2.10 [37]. This fiber has a hollow core, with the inner wall coated with a silver mirror coating, allowing light to propagate through reflections inside the tube. The inner diameter of the fiber is 1,000 μm, and the outer diameter is 1,600 μm. The length of the fiber is 2 m, and the specified transmission wavelength range is 2–15 μm. However, our measurements indicated that the fiber transmits infrared light up to 19 μm. The transmission efficiency, for a straight length of 1 m, is 65% at a wavelength of 10 μm. According to our measurements, for a curved length of 2 m, the normalized transmission efficiency at 10 μm was 10% at 17 μm and 3% at 19 μm.

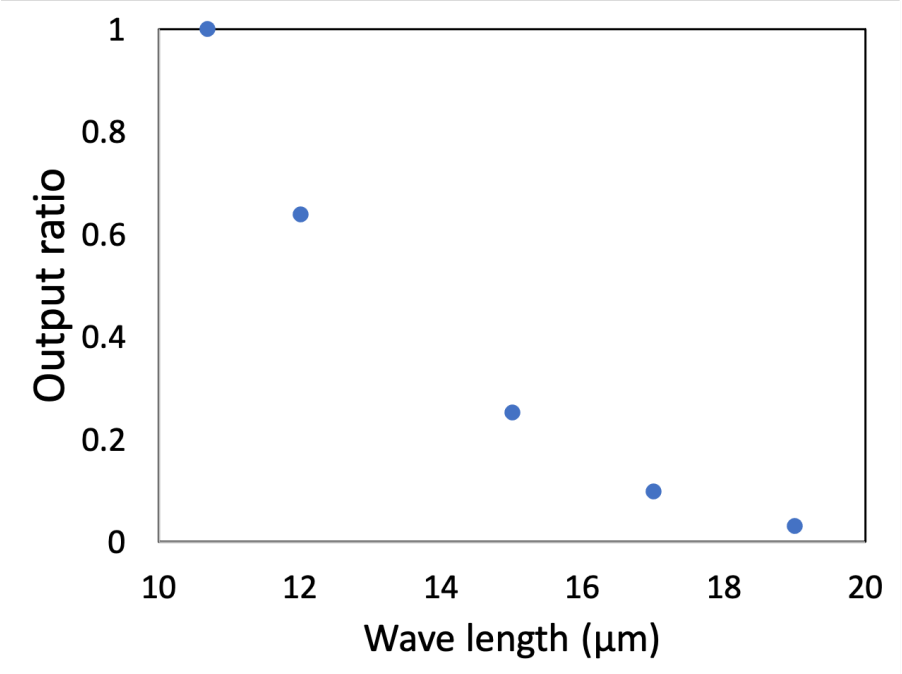

Figure 2.11: Transmission spectrum of hollow optical fiber

Band pass filter (BPF)

Figure 2.12: Narrow band pass filter wheel

To select the measurement wavelength, we used a narrow BPF. Figure 2.12 shows a photograph of the narrow BPF mounted on the filter wheel. This filter wheel is placed

in front of the detector and rotated to match the desired measurement wavelength.

In general, optical property measurements of materials are often performed using light sources with finite wavelength bandwidths (BW) rather than monochromatic light such as lasers. In our setup, the transmission wavelength characteristics of the BPF $\alpha_{\mathrm{measure}}(\lambda)$ were measured by a Fourier spectrometer. By the following procedure, we calculated the effective central wavelength (CWL) of the BPF. In this measurement, four BPFs are used. As an example, the calculation for 17.1 μm BPF is shown here. For the other BPFs (10.6, 11.4, 14.0 µμm), please refer to Figure A.1 – A.3 in Appendix A.

The effective transmission characteristics of the BPF $\alpha_{\mathrm{bpf}}(\lambda)$ were calculated using the following Equation 3.1:

$$\alpha_{\mathrm{bpf}}(\lambda) = L_{\mathrm{ir}}(\lambda) \times \alpha_{\mathrm{fiber}}(\lambda) \times \alpha_{\mathrm{measure}}(\lambda) \tag{2.2}$$

- $L_{\mathrm{ir}}(\lambda)$: Emission spectrum of a filament light source approximated as blackbody radiation at 1,200 K (Figure 2.13),
- $\alpha_{\mathrm{fiber}}(\lambda)$: Wavelength-dependent transmission characteristics of the hollow optical fiber (Figure 2.14),
- $\alpha_{\mathrm{measure}}(\lambda)$: Measured transmission wavelength characteristics of the BPF using the Fourier spectrometer (Figure 2.15).

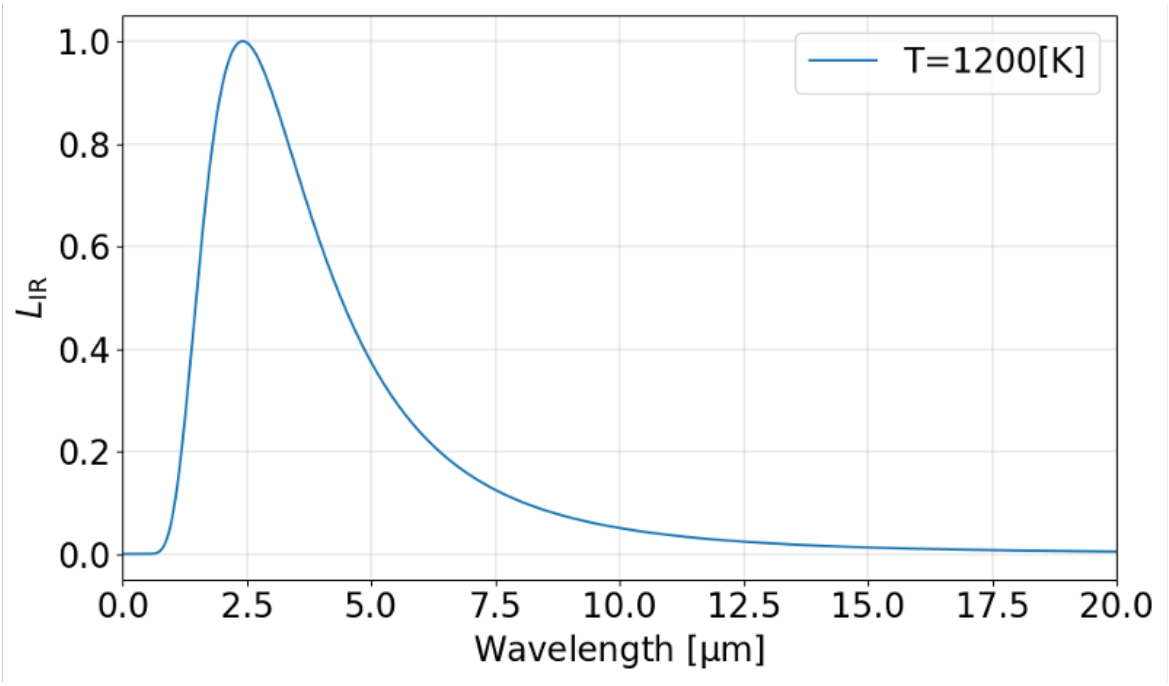

Figure 2.13: Emission spectrum of a 1200 K blackbody light source $L_{\mathrm{ir}}(\lambda)$. The spectral intensity is normalized by the peak intensity and plotted.

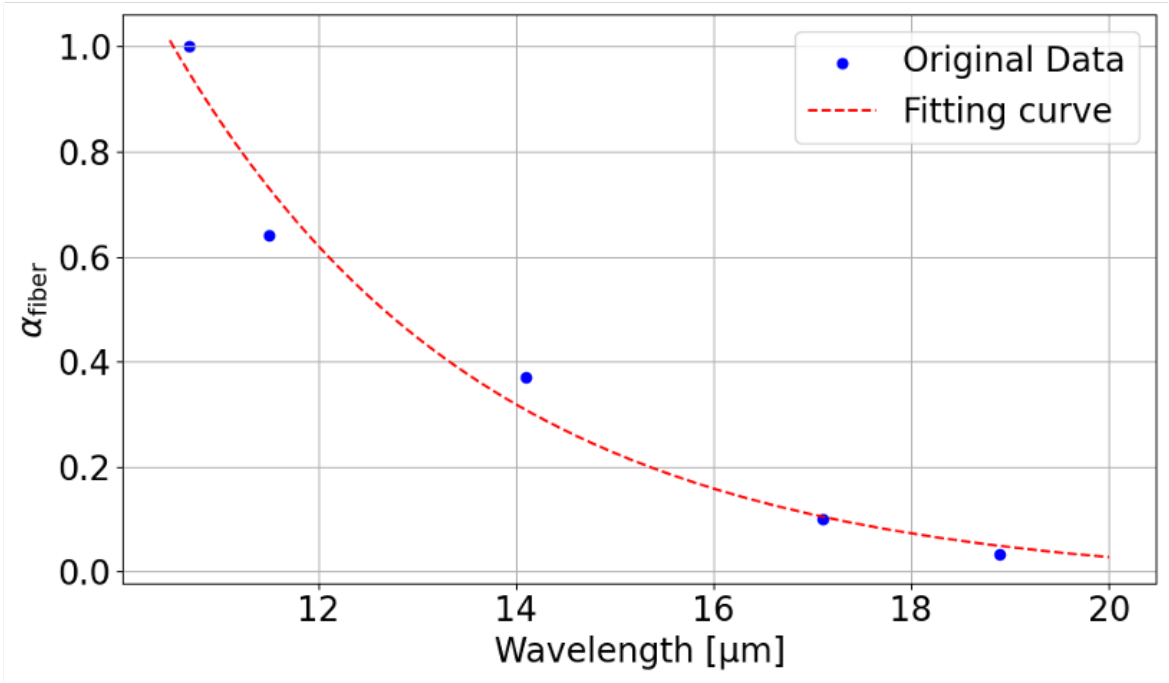

Figure 2.14: Wavelength-dependent transmittance of the hollow optical fiber $\alpha_{\mathrm{fiber}}(\lambda)$. The blue dots represent the measured points, while the red dashed line represents the fitted curve using an exponential function.

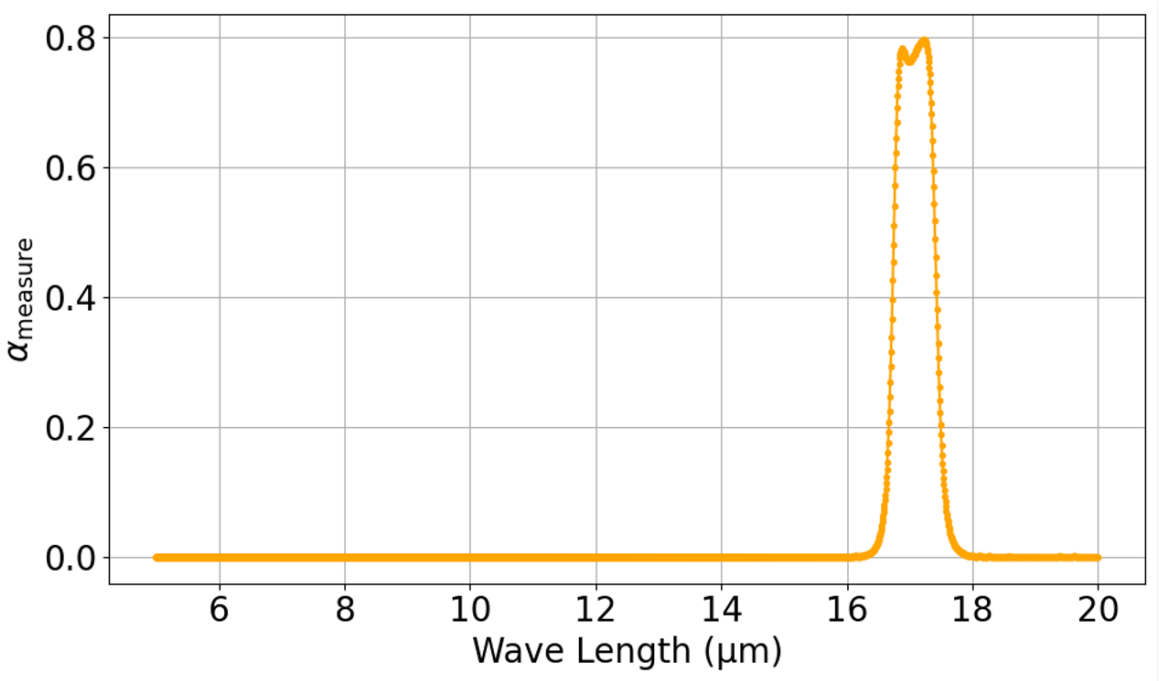

Figure 2.15: Wavelength-dependent transmittance of the 17.1 μm bandpass filter (BPF) measured with a Fourier spectrometer $\alpha_{\text{measure}}(\lambda)$.

Using the Full Width at Half Maximum (FWHM) of $\alpha_{\text{bpf}}(\lambda)$ (Figure 2.16), the following Equations (2.3, 2.4) were used to determine the effective central wavelength (CWL) and bandwidth (BW), and Table 2.1 shows other CWL and BW of BPFs:

$$\text{CWL} = \frac{\text{FWHM}_{\text{Short}} + \text{FWHM}_{\text{Long}}}{2} \tag{2.3}$$

$$\text{BW} = \frac{\text{FWHM}_{\text{Long}} - \text{FWHM}_{\text{Short}}}{2} \tag{2.4}$$

- $\text{FWHM}_{\text{Short}}$: Shorter wavelength at the FWHM,
- $\text{FWHM}_{\text{Long}}$: Longer wavelength at the FWHM.

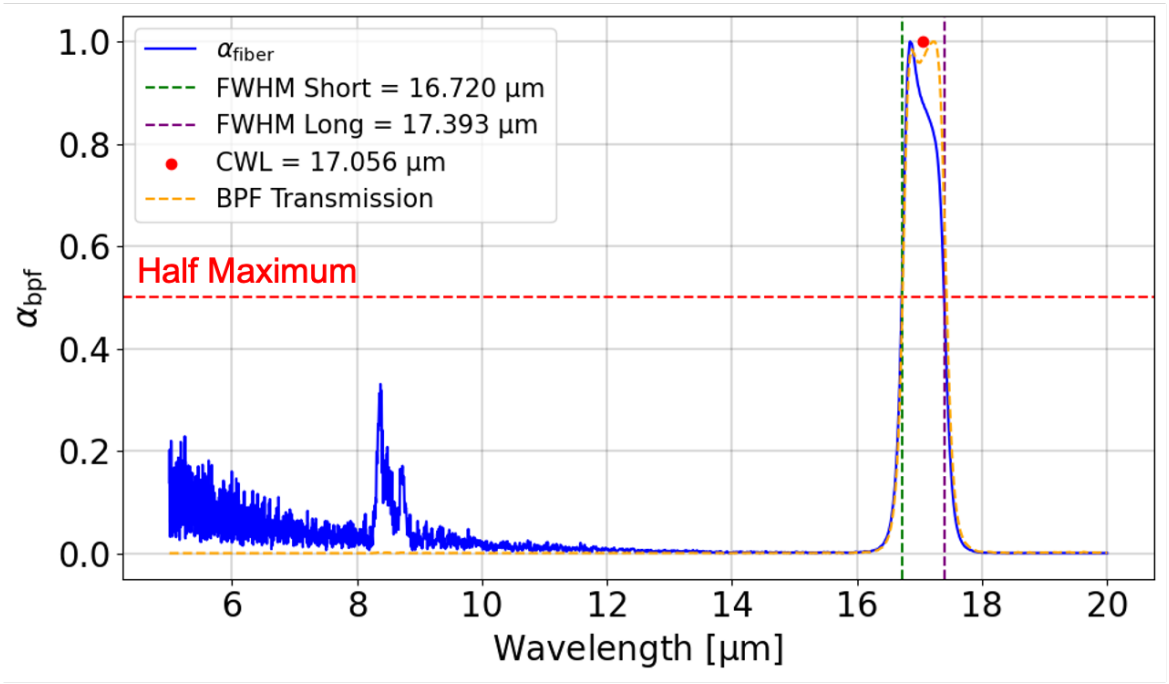

Figure 2.16: Effective wavelength-dependent transmittance of the 17.1 μm BPF $\alpha_{\text{bpf}}(\lambda)$. The red dot represents the effective central wavelength (CWL) of the BPF. The blue line shows α_{bpf}, the orange dashed line shows α_{measure}, the red dashed lines indicate the full width at half maximum (FWHM), the green dashed line represents the FWHM short wavelength, and the purple dashed line represents the FWHM long wavelength.

Table 2.1: CWL and BW of BPF

CWL (μm)	**BW (μm)**
10.6	0.5
11.4	0.4
14.0	0.4
17.1	0.3

Mercury Cadmium Telluride detector (MCT detector)

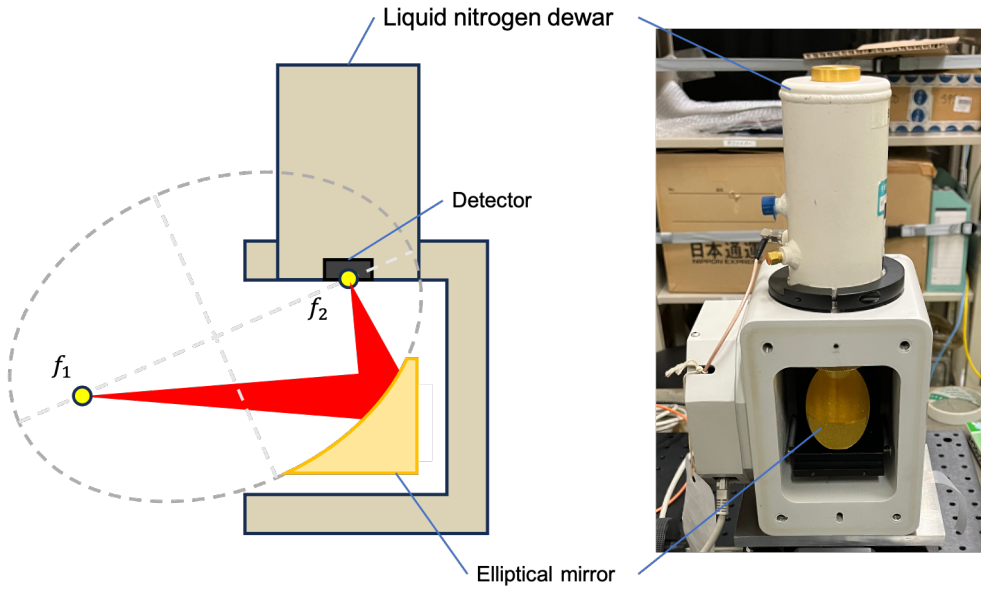

Figure 2.17: (Left)Schematic diagram of the MCT detector. (Right)Photo of the MCT detector.

The MCT detector is an infrared sensor that uses a semiconductor composed of mercury (Hg), cadmium (Cd), and tellurium (Te), characterized by ultra-high sensitivity and ultra-fast response (Figure 2.17). An MCT (IPH48) installed in the Fourier spectrometer BOMEM DA8 was removed and used as the infrared detector for this study.

As shown on the left side of Figure 2.17, this detector includes an elliptical mirror. Diffuse light from the exit aperture of the hollow optical fiber located at the focal point f_1 is reflected by the elliptical mirror and focused on the detection surface (1×1 mm^2) at the focal point f_2. To minimize the influence on the uncertainty of angle measurements, it is necessary to minimize a gap between the hollow optical fiber and the MCT detector. For this reason, the elliptical mirror is used to create a room to place aBPF wheel between the fiber and the detector surface.

Table 2.2: Specifications of MCT Detector [38]

Optical range	500 to 5,000 cm^{-1} (2 to 20 μm)
D* greater	$> 1 \times 10^{10}$
Detector size	1 mm^2
Operating temperature	77 K
Dewar hold time	8 h

2.3 Cooling system

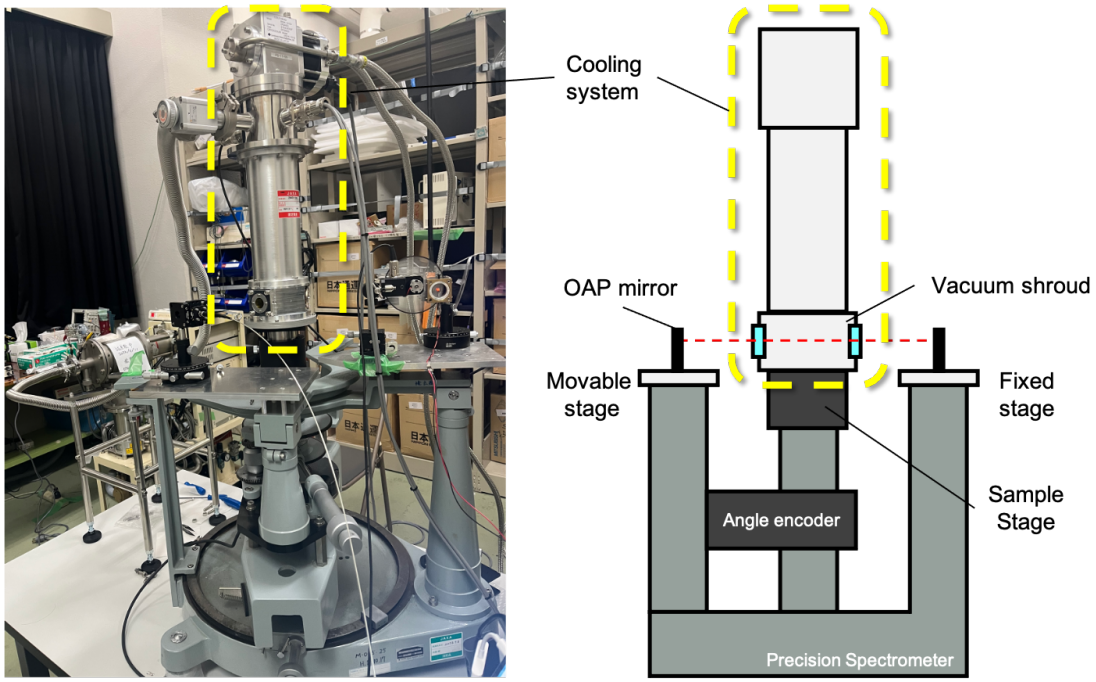

Figure 2.18: Inside the yellow dotted line is the cooling system on the sample stage. The left side is a picture and the right side is a schematic diagram. The red wavy line is the measurement collimated beam.

The cooling system is explained in this section. As shown in Figure 2.18, the cooling system is fixed to the central sample stage. Figure 2.19 is a block diagram of the cooling system and shows that this cooling system has temperature control. We used a helium circulation-type mechanical refrigerator (model PS11SS; Nagase Techno-Engineering Co.) to cool the sample for refractive index measurement to cryogenic temperatures. This

system is based on a 4 K-class GM cooler (Sumitomo Heavy Industries, RDK-101D) and provides the first-stage cooling capacity of 100 mW and the second-stage cooling capacity of 3 W. This allows the sample (sample holder) placed on the cold work surface with a diameter of 3 cm to be cooled to below 5 K in approximately 2.5 hours under no-load conditions.

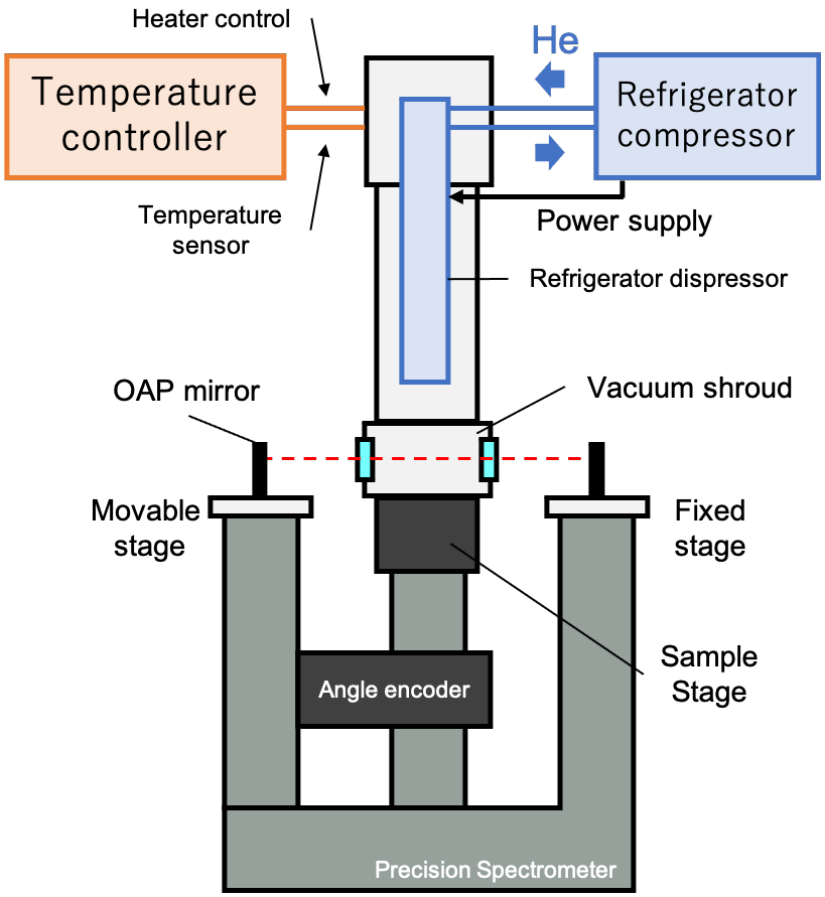

Figure 2.19: Block diagram of the cooling system

The cold work surface is equipped with a heater and a Si temperature sensor, providing temperature control functionality. The temperature of the cold work surface can be controlled to any desired temperature up to approximately 200 K with the stability of ±0.2 K (Figure 2.21 left). Hereafter, the temperature of the cold work surface measured by the Si sensor is referred to as the "Cold head temperature."

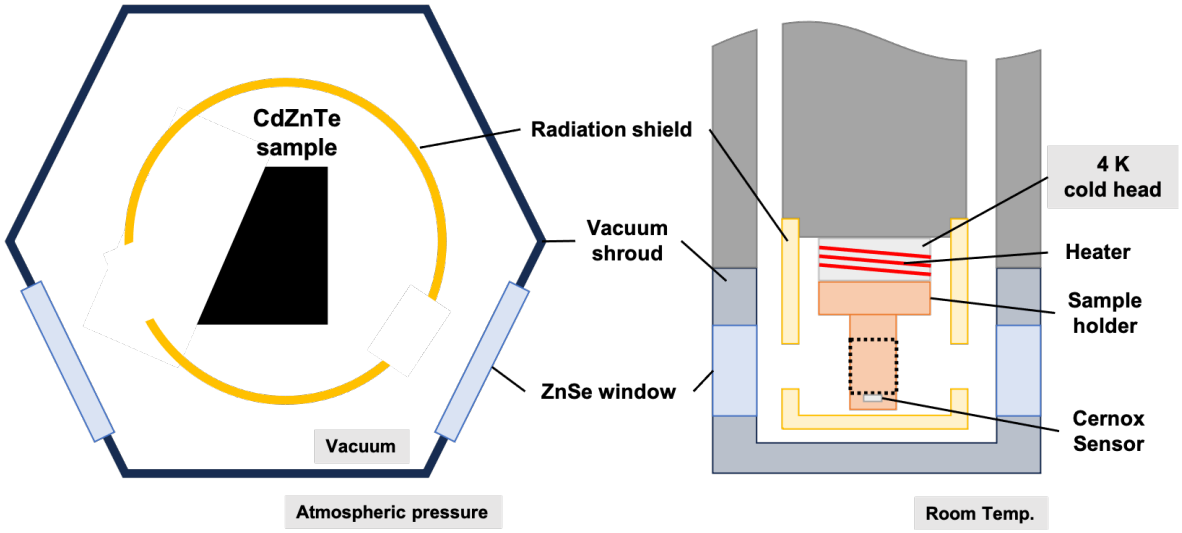

Figure 2.20: Schematic diagram of the inside of a vacuum shroud. The left side is a top view and the right side is a side view.

In order to cool the sample to cryogenic temperatures, measures are taken to prevent heat influx to the sample. As shown in Figure 2.20, there is a vacuum inside the vacuum shroud. The vacuum shroud is at room temperature to eliminate heat inflow to the sample due to air convection. In addition, if the sample is cooled to cryogenic temperatures while the shroud is filled with air, the important sample will be frosted and the windows will fog up, making it impossible to perform the measurement. Next, the sample is covered with a radiation shield to prevent heat radiation from the shroud at room temperature. The hole in the radiation shield was designed to a size sufficient to allow the deviation angle measurements described in later section 3.4, while minimizing thermal radiation as much as possible. There are no windows in the holes on the sides of the radiation shield. Although a window would have prevented the heat inflow, we decided not to add it due to the feasibility of the measurement. The light source for mid-infrared in this measurement system is very weak compared to lasers and other sources, so we did not use it to prevent the loss of light caused by the window. Finally, the sample holder is in contact with the 4 K cold head only to prevent heat conduction due to contact. With these measures, the sample temperature reached 12.57 $\pm$ 0.14 K (See section 3). The reason the sample temperature did not reach 4K was the presence of thermal contact inflow from the temperature sensor leads.

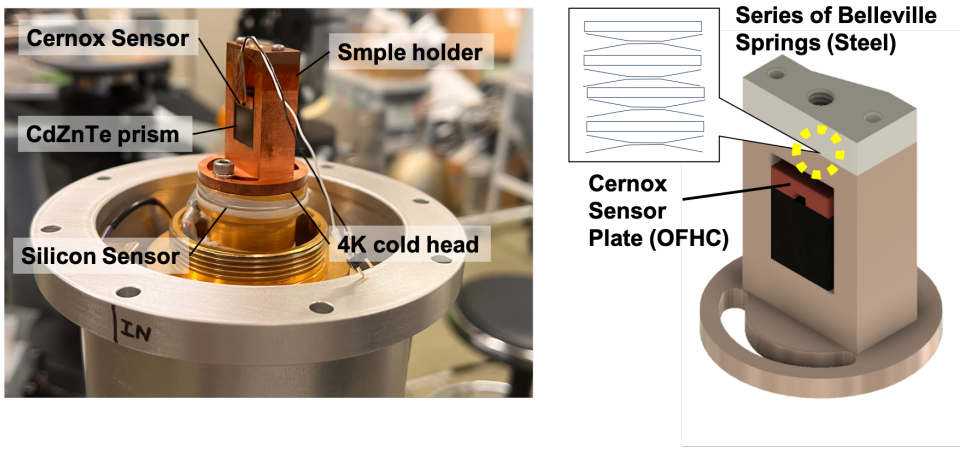

Figure 2.21: Sample holder. The sample temperature is measured by attaching a Cernox temperature sensor to the upper surface of the sample as shown in right Figure. The sensor is affixed to a copper plate, which is then pressed against the sample using a Belleville spring. (Note: the orientation is opposite to that of Figure 2.7, with the top and bottom reversed.)

The appearance of the sample holder is shown in Figure 2.21. The holder is made of oxygen-free copper (OFHC, RRR100), which has a high thermal conductivity $>$ 678W $\mathrm{m}^{-1}\,\mathrm{K}^{-1}$ at 4 – 70 K. To ensure good thermal contact between the prism and the cold work surface via the sample holder, a Cernox temperature sensor plate is pressed by a Belleville spring. Hereafter, the temperature measured by the Cernox sensor on this plate is referred to as the "Sample temperature." This is because the Cernox sensor is in contact with the sample, allowing it to measure the sample's temperature. The sample holder and prism contract as they cool to cryogenic temperatures. The reason for using a Belleville spring is to provide sufficient spring contraction, greater than the contraction of the sample holder when cooled from room temperature to cryogenic temperatures, in order to maintain good thermal contact between the prism and holder (Figure 2.21 right). The pressure at the contact surface is approximately 0.70 MPa. Although the fracture strength of CdZnTe is unknown, assuming it is similar to that of CdTe (22 MPa), this design provides a significant safety margin.

2.4 Customization

This measurement system is an improved version of the refractive index measurement apparatus developed in the previous study by Yamamuro et al. (2006) [29]. As shown in Table 1.5 in section 1.5, the wavelength range of Yamamuro et al. (2006) [29] was 0.365–3.5 μm, and the cooling system using liquid nitrogen allowed the sample to be cooled to 80 K. This system was customized to extend the wavelength range to 17 μm and to lower the sample temperature to 4 K by using a helium circulation-type mechanical refrigerator.

2.5 Novelty and originality of the measurement system

There are several instruments that can measure absolute refractive indices using the minimum declination method (Table 1.5). This study represents the first successful development of an instrument capable of measuring the absolute n across a temperature between of 12.57 and 300 K and a wavelength range of 10.6, 11.4, 14.0, and 17.1 μm.

In this section, we focus on the novelty and originality of the measurement system, which can be summarized in the following three aspects: 1) realization of a highly efficient optical system, 2) construction of a cooling system that achieves cryogenic temperatures, and 3) establishment of a minimum deviation measurement method using a single-element detector.

2.5.1 Realization of a highly efficient optical system

In the mid-infrared wavelength range above 10 μm, strong light sources (such as CO_2 , quantum cascade lasers) are not so available. Therefore, it is necessary to minimize optical losses and relatively weak, thermal (nearly black-body) light sources, as the measurement light. Additionally, because mid-infrared light is invisible, the optical system must be designed so that the optical axis aligns with visible light to ensure proper alignment.

To generate collimated beam, an OAP mirror was chosen instead of a lens. This is

because OAP mirrors with gold coatings maintain high reflectivity between visible and mid-infrared wavelengths, enabling the unification of the optical systems. Optical fibers were employed to allow for easy switching between the visible-light system for apex angle measurements and the infrared system for deviation angle measurements. Since these systems use different light sources and detectors, the flexibility of fiber positioning makes it optimal for these adjustments.

However, commonly used PIR fibers for mid-infrared light have poor transmittance beyond 14 μm. Therefore, in this study, a hollow optical fiber capable of transmitting light up to $\sim$ 20 μm was adopted. Nevertheless, the key characteristics of this fiber, such as NA and the effect of bending on transmittance, had not been fully understood. This study is the first experimental evidence to demonstrate that the infrared angular profile with the hollow optical fiber exhibits a Gaussian-like profile for unpolarized and non-coherent light, similar to conventional fibers.

2.5.2 Construction of a cooling system that achieves cryogenic temperatures

To ensure efficient cooling, the sample size was minimized to 10-mm square, despite the challenge of reducing the beam width and maintaining sufficient light intensity. To cool the sample to cryogenic temperatures, the sample must be held in a holder with high thermal conductivity. Additionally, OFHC (Oxygen-Free High Conductivity Copper) was used in the holder to ensure adequate thermal conductivity. The sample holder was carefully designed (see Figure 2.21) to prevent damage to the CdZnTe sample.

Furthermore, the relative position between the windows on the vacuum shroud and the sample holder was designed by predicting δ_{min} in advance. To minimize heat inflow from the outside, the sizes and positional relationships of the holes in the vacuum shroud and radiation shield were calculated with precision.

2.5.3 Establishment of a minimum deviation measurement method using a single-element detector

The conventional method of the GMR-1 refractometer allows for relatively easy detection of δ_{min} at visible wavelengths; however, it is challenging to apply the same method to invisible, mid-infrared wavelengths. Since it is difficult to readily procure an array detector capable of detecting mid-infrared light, a method for measuring δ_{min} using a single-element detector was established. For details, please refer to section 3.4.

2.6 Expandability of the measurement system

The light source and detector of this measurement system are located outside of the shroud. Therefore, n at 2–10 μm can be measured simply by adding a BPF in front of the detector. In addition, since there are fiber ports on both the light source and detector sides, the light source and detector can be changed without alignment adjustment, allowing measurements at various wavelengths.

Furthermore, the addition of a window in the shroud enables measurement of αe at low temperatures, making it possible to measure n of a sample more accurately.

Chapter 3

MEASUREMENTS AND RESULTS

To calculate n, the values of $\delta_{\min}$ and we have α are required, as shown in Equation 1.10. In these measurements, we determined n of CdZnTe between a wavelength of 10.6, 11.4, 14.0, 17.1 μm between cryogenic temperature and room temperatures by following the procedure outlined below:

1. Angle calibration measurement
2. Apex angle measurement at room temperature
3. Deviation angle measurement from cryogenic temperatures to room temperature

The following sections explain the procedure of each measurement and its data analysis.

The following sections show the CdZnTe sample measured firstly, and then explain the procedure of each measurement and its data analysis.

3.1 CdZnTe sample

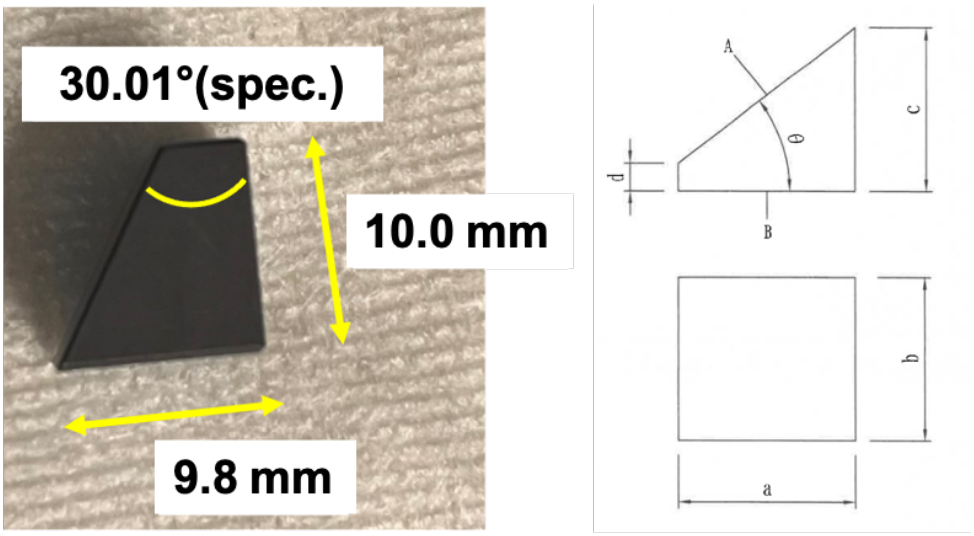

Figure 3.1: (Left) CdZnTe sample and (Right) Schematic view of a sample [39]

In this section, we describe the samples used for measurement. To determine the temperature and wavelength dependence of n of CdZnTe, we prepared a CdZnTe prism with a 10 mm square and α of 30.01° (spec.) (see Figure 3.1). The sample is a single crystal of $Cd_{0.96}Zn_{0.04}Te$ manufactured by JX Nippon Mining Metals Corporation. Based on previous research [40] indicating that high-resistivity n-type crystals with resistivity $> 1 \times 10^7\ \Omega \cdot \mathrm{cm}$ are optimal for mid-infrared immersion gratings, we measured n of a crystal with similar resistivity values in this study.

CdZnTe ingots were made by the vertical gradient freezing (VGF) method, with the manufacturer controlling conductivity and cutting 10 mm square substrates from the ingots. The substrates were then polished into the prism shape by Kogakugiken Corp. to create a sample meeting the specifications shown in Table 3.1. α was set to 30° to ensure that the refracted light at δ_{min} would pass through the vacuum shroud window and radiation shield hole (lease refer to 2 for details.) and remain within the rotational range of the movable stage. The surface roughness of $< \lambda/4$ ($\lambda = 632.8$ nm) was required to achieve sufficient autocollimation during apex angle measurements, and the actual polished surface roughness reached this requirement.

Table 3.1: Specifications of the CdZnTe Prism. The surface roughness was measured at $\lambda = 632.8$ nm [39].

No.	a (mm)	b (mm)	c (mm)	d (mm)
	10.0 ± 0.1	10.0 ± 0.1	(10)	4.0 ± 0.1
1	10.01	10.00	9.80	4.02

Surface Flatness $< \lambda/4$		θ (degrees)	Resistivity
A	B	30.0 ± 0.1	$> 1 \times 10^7\ \Omega \cdot \text{cm}$
$\lambda/11$	$\lambda/6$	30.01	$> 1 \times 10^7\ \Omega \cdot \text{cm}$

3.2 Angle calibration measurement

In the angle calibration measurement, the reference point of the movable stage is determined and aligned with the origin of the angle measurement. This measurement is done every time the light source or fiber is changed. Each measurement was performed three times.

Figure 3.2 shows the setup for the angle calibration measurement. This setup includes two rotating components: one is the central sample stage, and the other is the movable stage. Both stages share the same rotation axis, which is centered on the sample stage. In this measurement, the central rotating sample stage is left empty, with no sample placed on it. Diffused light from the light source is focused by a lens and enters an optical fiber. The transmitted light is then reflected by the OAP mirror on the fixed stage, forming a collimated beam with a diameter of 10 mm. Next, the collimated beam is reduced to a 5 mm diameter using an orifice. The beam then propagates straight through the rotation center of the sample stage. To capture this collimated beam, the movable stage is rotated, directing the beam towards another OAP mirror. The OAP mirror reflects the light, which then enters another optical fiber. At the opposite fiber end, the light is diffused, refocused by a lens, and finally detected by the PD.

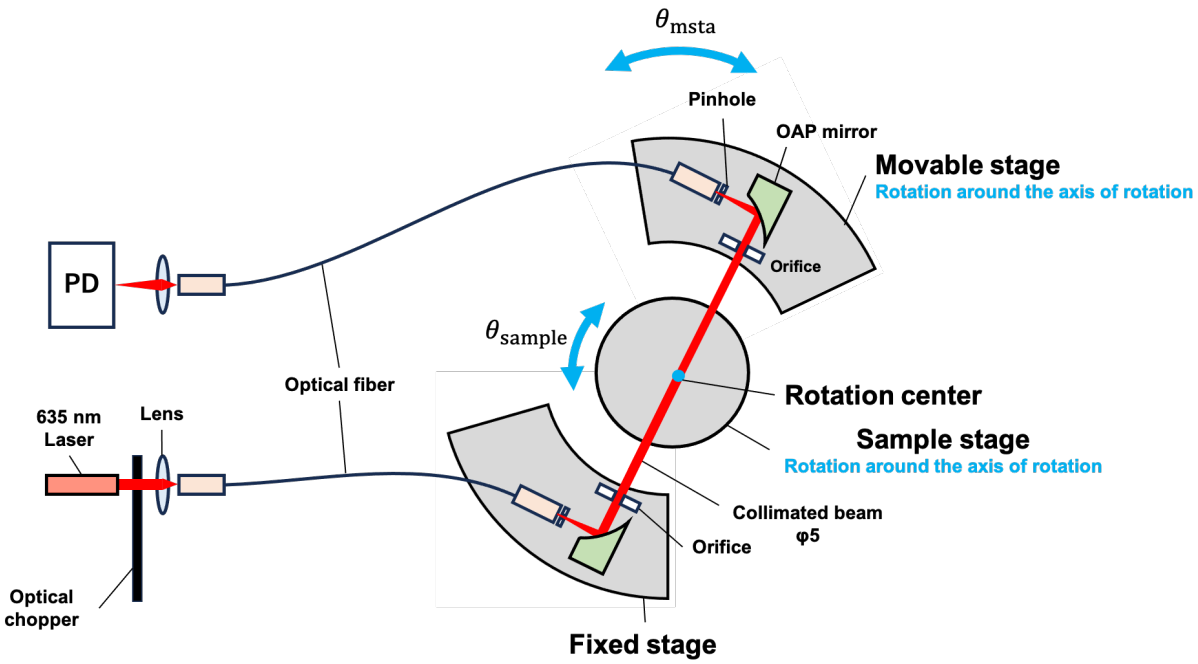

Figure 3.2: Schematic diagram of an angle calibration measurement setup. This diagram is for angle calibration measurement with a visible light source. For angle calibration measurement with an infrared light source, change the light source to an infrared filament light source.

Due to the characteristics of the optical system, the detector voltage as a function of the rotation angle θ_{msta} of the movable stage exhibits a Gaussian-like distribution. Therefore, the exact angle of a given beam was determined by fitting the obtained measurement profile with a Gaussian. The peak value of the Gaussian is defined as the calibration angle θ_0 for α and the deviation angle measurements. This procedure is applied to subsequent angle measurements as well.

Table 3.2 shows the results of the angle calibration measurements with visible and infrared light. Using the results of visible light, which allows easier alignment, as a reference, it was found that the results for infrared light were consistent within 0.4%. Furthermore, no significant difference was observed in the angle calibration measurements with and without the vacuum shroud for infrared light. Although the calibration values are not identical for each measurement due to recalibration, the visible light measurement results were used for α calibration, and the infrared light measurement results without the shroud were used for the minimum deviation angle measurement.

Table 3.2: Calibration of angle θ_0 in visible and infrared light measurements

Light Source	Calibration angle θ_0 (degree)
Visible light source at 635 nm	23.415 ± 0.001
Infrared light source at 10.68 μm	23.338 ± 0.003
Infrared light source at 10.68 μm with shroud	23.340 ± 0.007

3.3 Apex angle measurement

The apex angle α of the CdZnTe sample is measured using autocollimation measurements on the two surfaces adjacent to the apex (Surface A and Surface B). Autocollimation is a high-precision angular measurement technique that utilizes the reflection of light. This measurement was conducted at room temperature and atmospheric pressure. Each autocollimation measurement was performed three times.

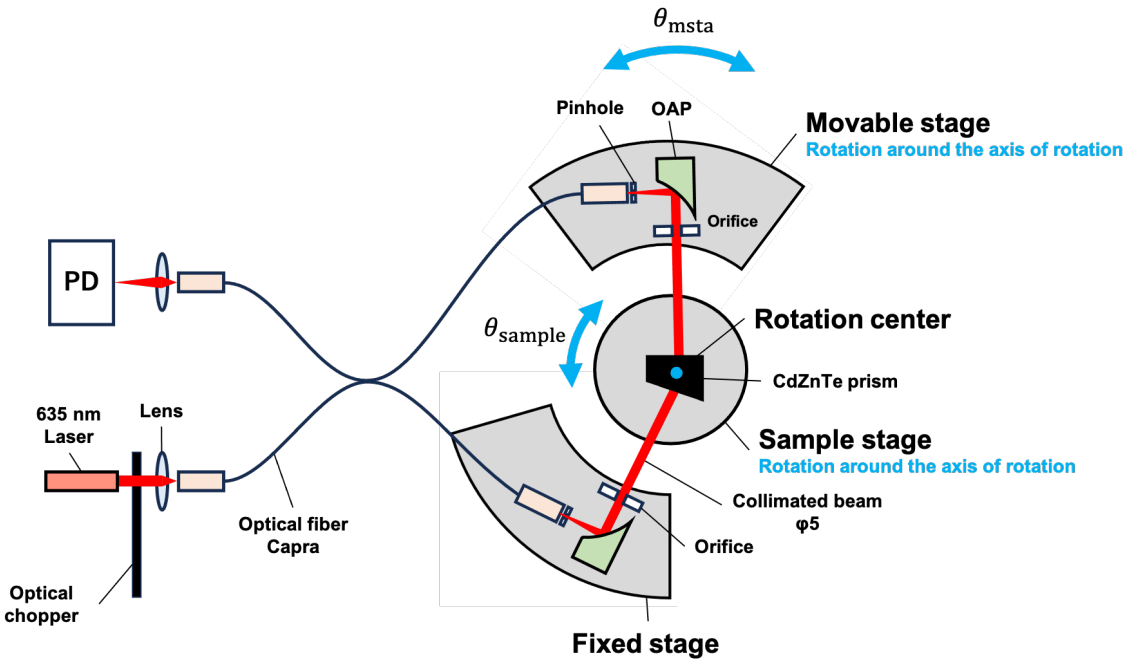

Figure 3.3: Schematic of an apex angle measurement setup

Figure 3.3 illustrates a schematic diagram of the setup for apex angle measurement. As described in the angle calibration section, both the sample stage and the movable stage rotate around the central rotation axis of the sample stage. In this measurement,

the prism is placed at the center of the sample stage. Light from a visible laser source is focused by a lens and enters the optical fiber coupler (details of the optical fiber coupler, refer to Section 2.2.1). The light is then split into two paths at a branching point: one path is transmitted to the fiber end on the fixed stage, while the other is transmitted to the fiber end on the movable stage. The light exits each fiber end as diffused light, which is then reflected by an OAP mirror to form a collimated beam with a diameter of 10 mm. Then, the collimated beam is reduced to 5 mm in diameter using an orifice.

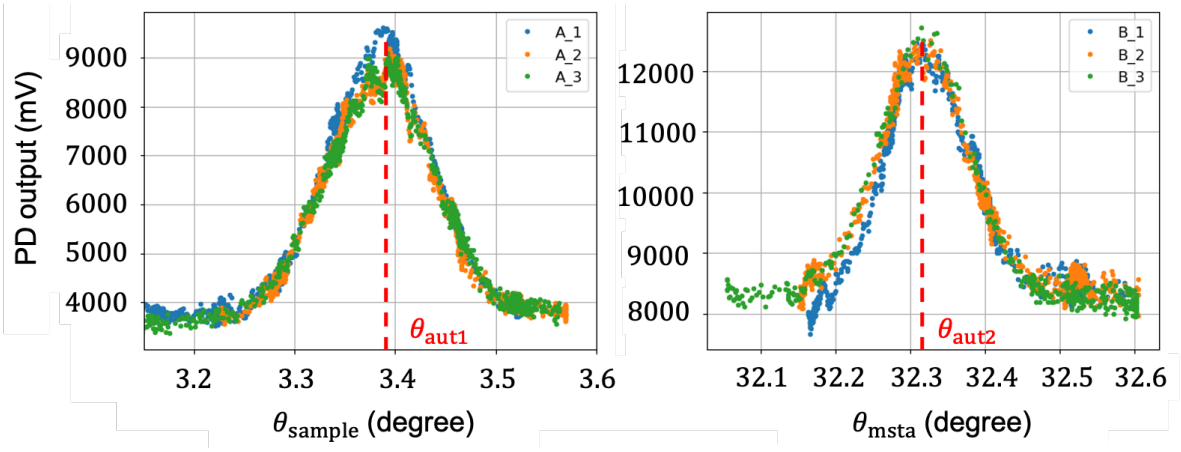

Figure 3.4: The autocollimation measurement results for Surface A (left panel) and Surface B (right panel) of the sample. Each measurement was repeated three times. The peak values for each measurement were fitted with a Gaussian function, and the autocollimation angles θ_{aut1} and θ_{aut2} were determined.

First, we describe the autocollimation measurement on the fixed stage. The collimated beam produced by the OAP mirror is incident on Surface A of the prism and is reflected. As the sample stage angle θ_{sample} is gradually rotated, the collimated beam striking Surface A is precisely reflected back to the OAP mirror. The OAP mirror then reflects the light back into the optical fiber coupler, where it is transmitted through the fiber and exits as diffused light at the opposite fiber end. This light is refocused by a lens and detected by a PD. Due to the characteristics of the optical system, the detector voltage as a function of θ_{sample} follows a Gaussian-like distribution as shown in Figure 3.4 (left panel). By fitting the obtained measurement profile with a Gaussian function, the peak value is determined. The corresponding angle is defined as the autocollimation angle θ_{aut1}. Next, we describe the autocollimation measurement on the movable stage. The

rotation angle of the sample stage θ_{sample} is set to θ_{aut1} and fixed. As in the measurement for Surface A, the collimated beam produced by the OAP mirror is incident on Surface B of the prism and is reflected. As the movable stage angle θ_{msta} is gradually rotated, the collimated beam striking Surface B is precisely reflected back to the OAP mirror. The OAP mirror then reflects the light back into the optical fiber coupler, and the transmitted light is detected by the PD in the same manner as before. The autocollimation angle for Surface B is defined as θ_{aut2} (see Figure 3.4 (right panel)). By using the optical fiber capra, collimated light can be generated from the OAPs on both sides. This simplified the optical system.

Finally, the difference between θ_{aut1} and θ_{aut2} gives α of the prism (Equation 3.1):

$$\alpha = \theta_{\text{aut2}} - \theta_0, \tag{3.1}$$

As a result, α of the CdZnTe prism was found to be $30.033 \pm 0.001°$. In the current derivation of n, we assumed that α does not have temperature dependence.

However, it is possible that using a Gaussian function to determine the peak values may not have been the optimal choice. The values of θ_{aut1} and θ_{aut2} may change slightly depending on the fitting function used. This change can affect the determination of n. To improve the accuracy of peak value determination, it is recommended to select only the region near the peak and fit it with an upward convex function.

3.4 Deviation angle measurement

In this study, the deviation angle δ is measured for each incident angle θ_1, and δ_{min} is obtained from the dependence of δ on θ_1. Each measurement was repeated multiple times.

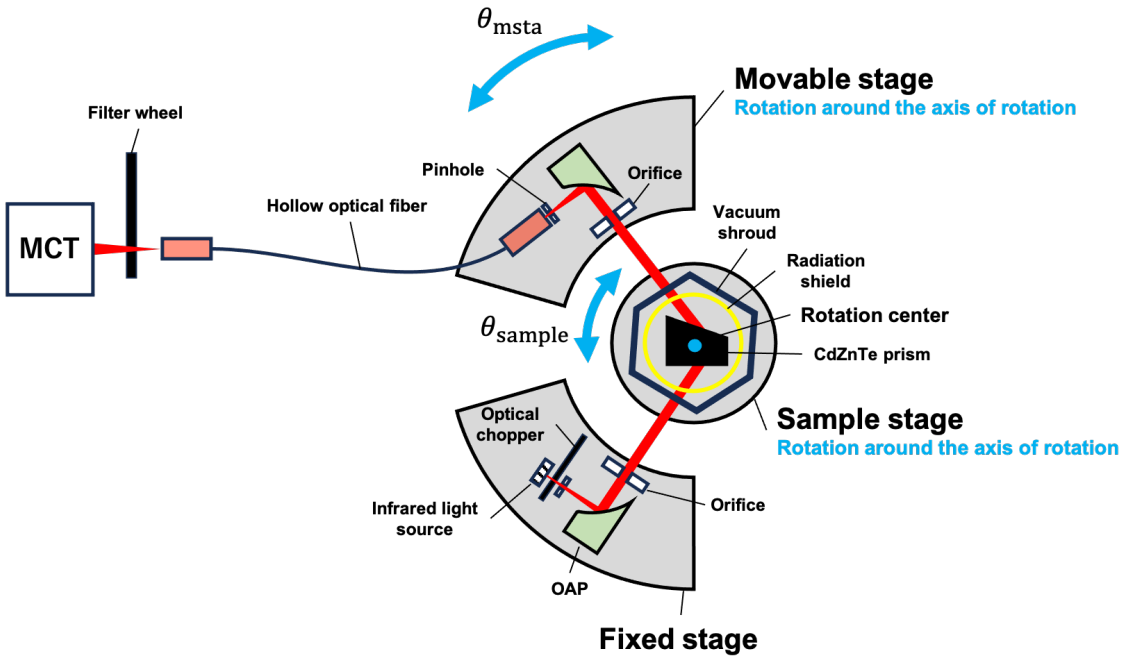

Figure 3.5: Schematic diagram of the deviation angle measurement. The arrows represent the direction of the measurement light. The 3D diagram is shown in Fig 2.7.

Figure 3.5 shows a schematic diagram of the deviation angle measurement setup. The CdZnTe sample is placed at the center of the sample stage. A pinhole with a diameter of 0.5 mm is placed in front of the diffused light from the infrared light source to create a pseudo point source. The light is reflected by the OAP mirror, forming a collimated beam with a diameter of 10 mm. The beam is then narrowed to a 5 mm diameter using an orifice. This collimated light passes through the vacuum shroud window and the radiation shield hole, refracts through the CdZnTe sample, and exits through the radiation shield hole and the vacuum shroud window. For details on the vacuum shroud and radiation shield, refer to Section 2.3. The movable stage is rotated to capture the collimated beam with the OAP mirror. The light reflected by the OAP mirror enters a hollow optical fiber and is transmitted to the MCT detector. Due to the characteristics of the optical system, the detector voltage as a function of θ_{sample} follows a Gaussian-like distribution. The hollow optical fiber used in this measurement has an aperture diameter of 1 mm. With this large diameter, the angular profile becomes broader, and the accuracy of peak determination using fitting becomes worse. Therefore, to restrict the width of the angular

profile, a pinhole with a diameter of 0.5 mm is placed at the aperture of the optical fiber. A filter wheel is placed in front of the MCT detector. This filter wheel contains four bandpass filters (BPFs) with wavelengths of 10.6, 11.4, 14.0, and 17.1 μm. By rotating the filter wheel, the measurement wavelength is selected.

Equation 3.2 represents the relationship between α of the prism and the refracted angles θ_1' and θ_2' (see Figure 1.10). Equation 3.3 corresponds to Snell's law. By using these, we obtain Equation 3.4, where the refractive index of vacuum is assumed to be $n_0 = 1$.

When Equation 3.4 is plotted with θ_1 on the horizontal axis and the deviation angle $\delta(\theta_1)$ on the vertical axis, a curve like the one shown in Figure 3.6 is produced. When an array detector is used, the turning point of δ_{min} can be captured continuously. However, with a single-element detector, it cannot be captured, so this measurement method is used. The minimum value is obtained when $\theta_1 = \theta_2$, and this minimum value is δ_{min}. In this study, δ_1 was measured at various θ_1, and Equation 3.4 was fitted to the results to determine δ_{min}.

$$\alpha = \theta_1' + \theta_2', \tag{3.2}$$

The Snell's law shows the following

$$n_0 \sin\theta_1 = n \sin\theta_1', \quad n_0 \sin\theta_2 = n \sin\theta_2', \tag{3.3}$$

Combining the Equations (3.2) and (3.3), we get the folllowng

$$\delta = \theta_1 + \theta_2 - \alpha = \theta_1 - \alpha + \arcsin\left[n \sin\left(\alpha - \arcsin\left(\frac{\sin\theta_1}{n}\right)\right)\right], \tag{3.4}$$

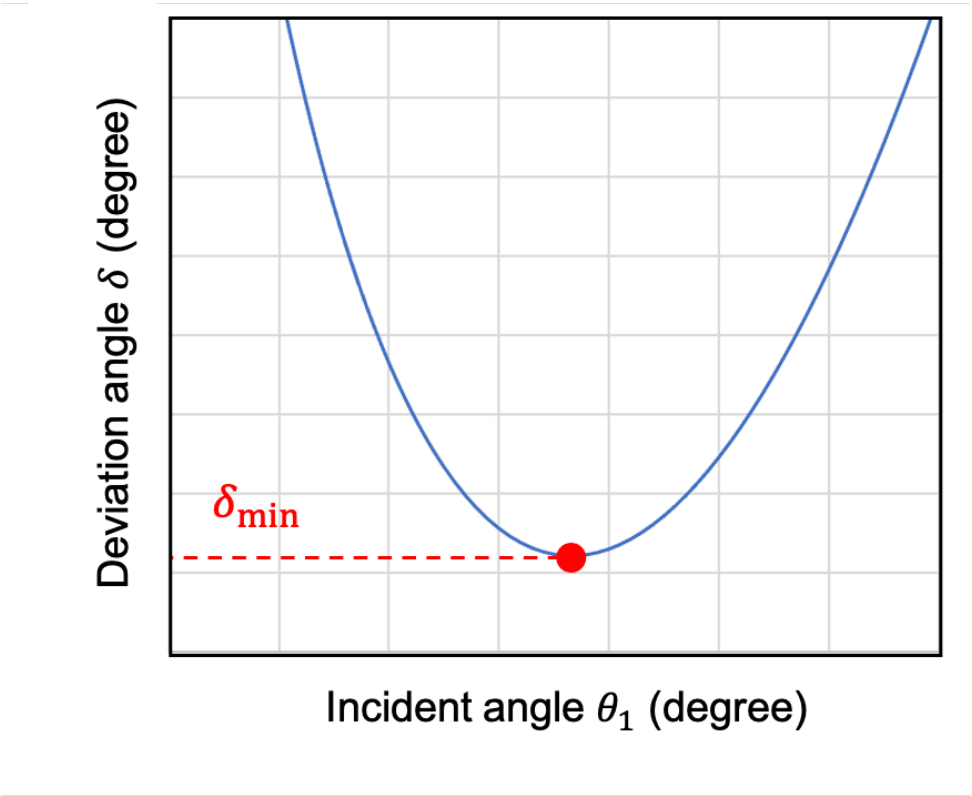

Figure 3.6: Example of the relation between incidence angle θ_1 and δ

We measured δ at room temperature (298$\pm$1 K) and 4, 20, 50, and 70 K, controlled by the heater which is built inside the cold head. Figure 3.7 shows the cold head temperature and sample temperature corresponding to each controlled temperature during the deviation angle measurements. Table 3.3 summarizes the temperatures for each controlled temperature of 4, 20, 50, and 70 K.

The temperature difference between the cold head temperature and the sample temperature is attributed to external heat input from the room temperature environment through the vacuum window, as well as thermal contact input from the Cernox temperature sensor leads measuring the sample temperature. We believe that the latter can be minimized in future setups.

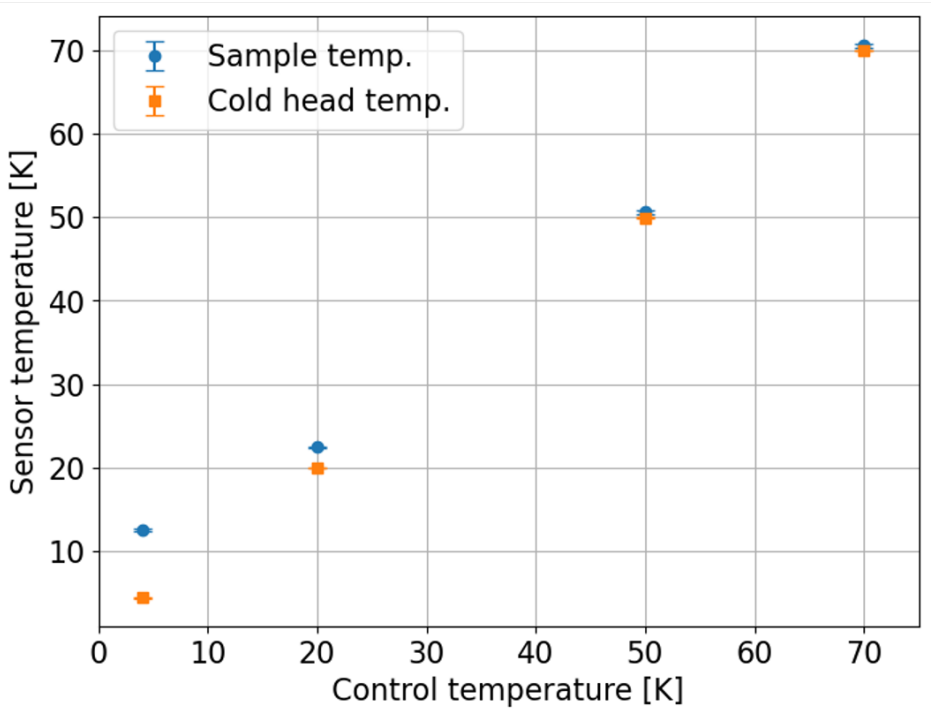

Figure 3.7: Measured temperatures vs control temperature in this experiment. The sample temperature is stable within 0.1 K at 20 K and below; 0.25 K at 50, and 70 K (control temperatures), respectively.

Table 3.3: List of temperatures in Kelvins

Control temp.	Cold head temp.	Sample temp.
70	69.97 ± 0.05	70.57 ± 0.23
50	49.94 ± 0.05	50.59 ± 0.20
20	19.99 ± 0.03	22.47 ± 0.06
4	4.43 ± 0.09	12.57 ± 0.14

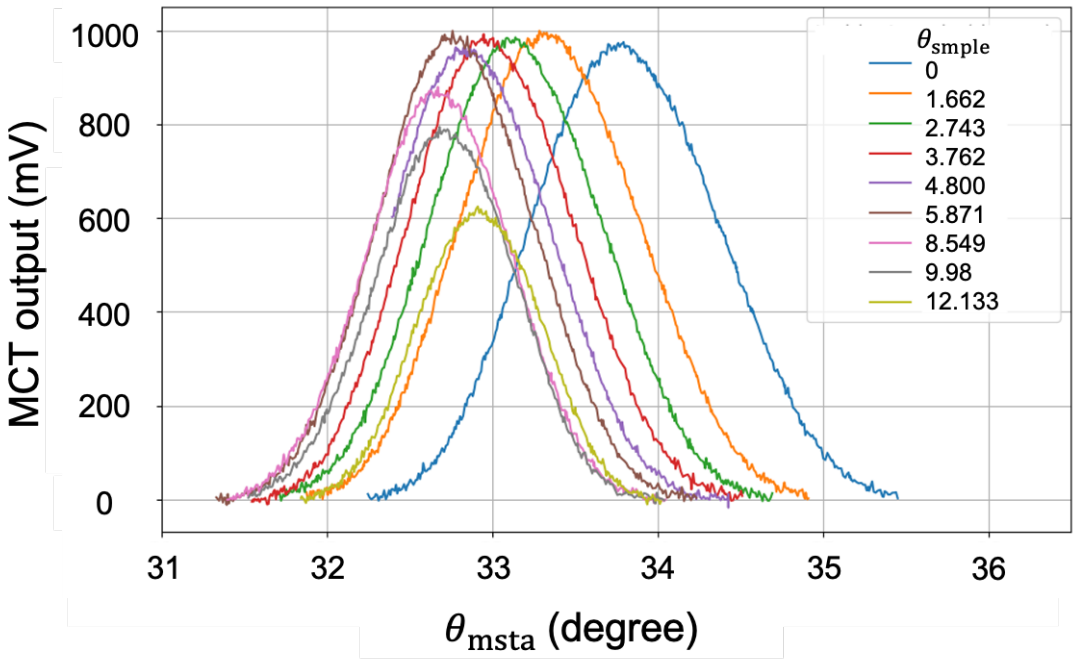

Figure 3.8: Results of deviation angle measurements at 22.47 ± 0.06 K for various incidence angles shown in the legend. The horizontal axis represents θ_{msta}, and the vertical axis shows the MCT output at that angle.

Figure 3.8 shows the results of deviation angle measurements at 22.47 ± 0.06 K for various θ_1. The horizontal axis represents θ_{msta}, and the vertical axis shows the MCT output at θ_{msta}. The peak values of each measurement's data were fitted with a Gaussian distribution to determine δ. Since δ at each θ_{msta} was measured multiple times, the weighted average of δ, obtained from each fitting was calculated. The fitting accuracy of δ, using Gaussian fitting is approximately $0.001 \sim 0.01°$. The same procedure was applied to deviation angle measurements at other temperatures and wavelengths.

In this study, Gaussian fitting was used as the fitting function. The fitting range includes the tails of the measurement data. Therefore, the fitting accuracy near the peak of the measurement data may be poor. As an improvement, it is recommended to limit the fitting range to the vicinity of the peak value (approximately the top 10%) and fit with an upward convex function (such as a quadratic function). Here, care should be taken to ensure that the fitting range is chosen where it is clear that the measurement data follow an upward convex function.

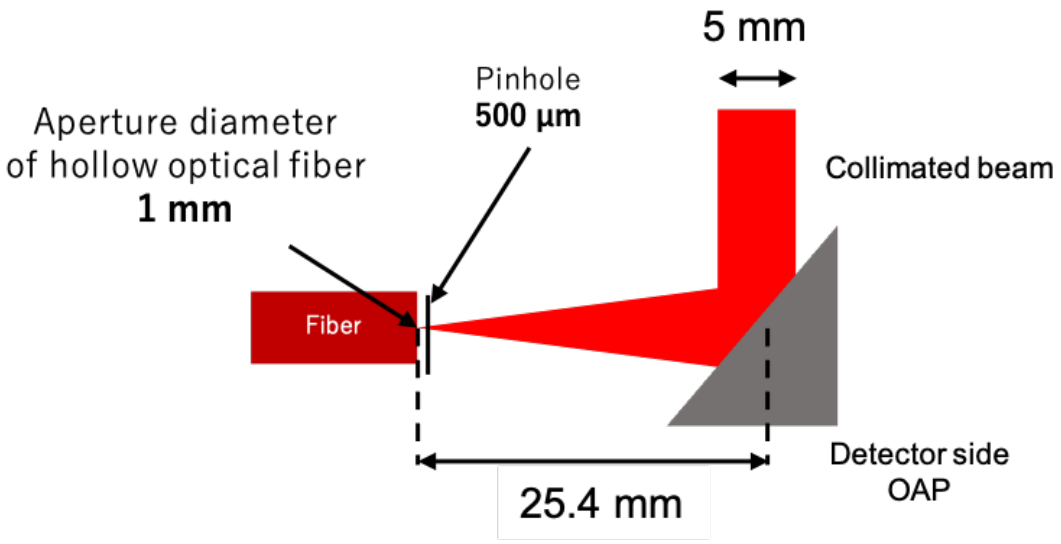

Figure 3.9: Schematic diagram illustrating how the OAP mirror on the detector side focuses the collimated beam refracted through the CdZnTe prism into a hollow optical fiber

Figure 3.9 is a schematic diagram illustrating how the OAP mirror on the detector side focuses the collimated beam refracted through the CdZnTe prism into a hollow optical fiber. Each beam profile is Gaussian-like, and its Full Width at Half Maximum (FWHM) is determined by the focal length of the OAP mirror (25.4 mm) and diameter of the pinhole in front of aperture of the fiber (Equation 3.5). A smaller FWHM improves the accuracy of fitting to determine the peak angle; therefore, a small FWHM is desirable. To achieve this, a 500 µm pinhole was placed in front of the hollow optical fiber, which has an aperture diameter of 1 mm. The calculated FWHM was 1.128°, and the measured average FWHM was $1.02 \pm 0.07°$.

$$\tan(\text{FWHM}°) = \frac{\text{Pinhole diameter (mm)}}{\text{OAP mirror focal length}} \tag{3.5}$$

3.5 Refractive index of CdZnTe

This section presents the results of refractive index measurements for CdZnTe. In this study, n of CdZnTe was measured at wavelengths of 10.6, 11.4, 14.0, and 17.1 μm, and at temperatures of 4, 20, 50, 70 K (controlled temperatures) and room temperature. During

the low-temperature measurements, the vacuum pressure inside the vacuum shroud was averaged at $(2.5 \pm 0.9) \times 10^{-3}$ Pa.

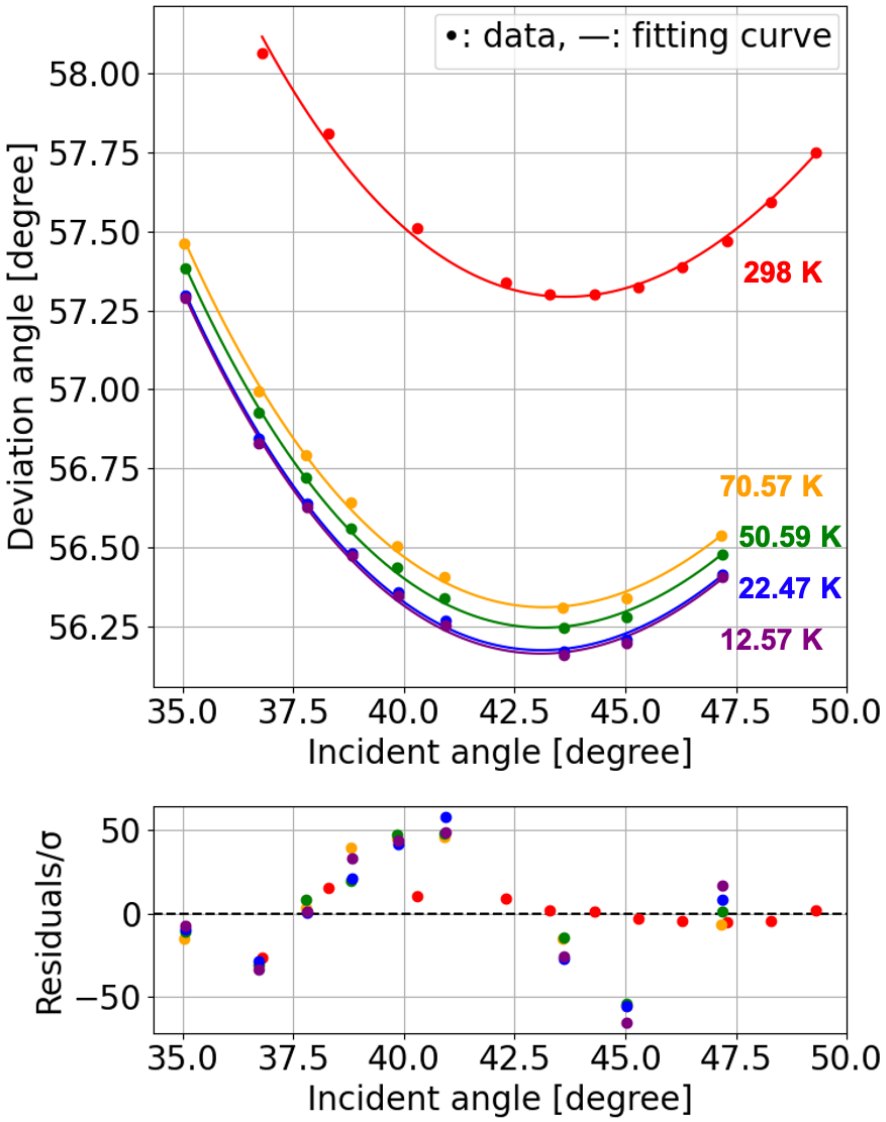

Figure 3.10: The top panel shows the results of the deviation angle measurements of CdZnTe at each control temperature at a wavelength of 10.6 μm, along with the fitting curves based on Equation 3.4. The bottom panel shows the residuals for each fitting. σ is the fitting error obtained from the deviation angle measurements (e.g., Figure 3.8).

The top panel of Figure 3.10 shows the dependence of δ on the incidence angle for the CdZnTe sample measured at 10.6 μm wavelength under controlled temperatures of 4, 20, 50, 70 K and room temperature. The plots in Figure 3.8 were fitted using Gaussian functions to obtain δ for each incidence angle. The colors of the symbols indicate the different controlled temperatures. The solid lines represent the curves of Equation 3.4

fitted to the results at each temperature, with n as a free parameter. The error bars for each data represent only statistical errors. The bottom panel of Figure 3.10 shows the residuals for each fitting, normalized by σ (the statistical error for each data). And also, Figure 3.11 shows the dependence of δ on the incidence angle for the CdZnTe sample measured at a temperature of 12.40 K and wavelengths of 10.6, 11.4, 14.0, and 17.1 μm. The colors of the symbols indicate the measured wavelengths. The solid lines represent the curves of Equation 3.4 fitted to the results at each wavelengths, with n as a free parameter.

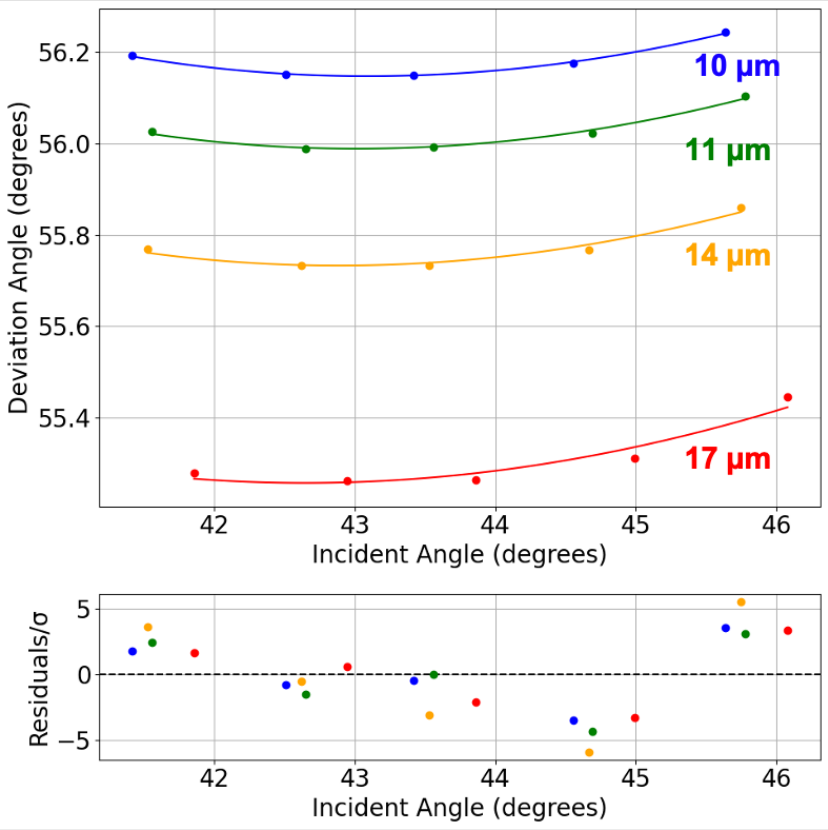

Figure 3.11: The top panel shows δ of CdZnTe at 12.40 $\pm$ 0.01 K for each wavelength, along with the fitting curves based on Equation 3.4. The bottom panel shows the residuals for each fitting. σ represents the fitting error obtained from the deviation angle measurements.

The bottom panels of Figure 3.10 and 3.11 show that the fitting residuals are large and follow a pattern that depends on the angle of incidence. This suggests that unexpected measurement errors may occur during declination measurements and that the model used in Equation 3.4 may not be correct.

The bottom panel of Figure 3.10 shows that the fitting at 298 K has smaller residual/σ values compared to other temperatures. The measurements at 298 K were taken without the vacuum shroud. Thus, the larger residual/σ values at 12.57, 22.47, 50.59, and 70.57 K are likely caused by the vacuum shroud. However, even at 298 K, a pattern is seen in the residual/σ. This could be due to the prism tilting relative to the rotation axis or aberrations in the OAP mirror. Section 4.1 talks about the measurement uncertainties in the system.

Table 3.4 and 3.5 summarizes the refractive indices of CdZnTe measured in this study.

Table 3.4: Refractive index of CdZnTe measured at various temperatures and wavelengths (1)

Wavelength (μm)	Temp. (K)	Refractive index n	Δn_{sta}	Δn_{sys}	$\Delta n_{\mathrm{total}}$
10.6	12.40 ± 0.01	2.63665	0.03×10^{-3}	0.9×10^{-3}	0.93×10^{-3}
	12.57 ± 0.14	2.63710	0.04×10^{-3}	0.9×10^{-3}	0.94×10^{-3}
11.4	12.40 ± 0.01	2.63274	0.08×10^{-3}	0.9×10^{-3}	0.98×10^{-3}
14.0	12.40 ± 0.01	2.62642	0.13×10^{-3}	0.9×10^{-3}	1.03×10^{-3}
17.1	12.40 ± 0.01	2.61464	0.35×10^{-3}	0.9×10^{-3}	1.25×10^{-3}
	22.47 ± 0.06	2.63730	1.50×10^{-3}	0.9×10^{-3}	1.05×10^{-3}
11.4	22.347 ± 0.003	2.63412	0.18×10^{-3}	0.9×10^{-3}	1.08×10^{-3}
14.0	22.347 ± 0.003	2.63002	0.08×10^{-3}	0.9×10^{-3}	0.98×10^{-3}
17.1	22.347 ± 0.003	2.61885	0.13×10^{-3}	0.9×10^{-3}	1.03×10^{-3}
10.6	50.59 ± 0.20	2.63910	0.15×10^{-3}	0.9×10^{-3}	1.05×10^{-3}
11.4	-	-	-	-	-
14.0	-	-	-	-	-
17.1	-	-	-	-	-

Table 3.5: Refractive index of CdZnTe measured at various temperatures and wavelengths (2)

Wavelength (μm)	Temp. (K)	Refractive index n	Δn_{sta}	Δn_{sys}	$\Delta n_{\mathrm{total}}$
10.6	70.57 ± 0.23	2.64070	0.18×10^{-3}	0.9×10^{-3}	1.08×10^{-3}
11.4	-	-	-	-	-
14.0	-	-	-	-	-
17.1	-	-	-	-	-
10.6	292.84 ± 0.04	2.65713	0.03×10^{-3}	0.9×10^{-3}	0.93×10^{-3}
	291.60 ± 0.03	2.65640	0.14×10^{-3}	0.9×10^{-3}	1.04×10^{-3}
	288.30 ± 0.30	2.65651	0.08×10^{-3}	0.2×10^{-3}	0.28×10^{-3}
11.4	292.84 ± 0.04	2.65413	0.04×10^{-3}	0.9×10^{-3}	0.94×10^{-3}
14.0	292.84 ± 0.04	2.64676	0.05×10^{-3}	0.9×10^{-3}	0.95×10^{-3}
17.1	292.84 ± 0.04	2.63465	0.13×10^{-3}	0.9×10^{-3}	1.03×10^{-3}

Chapter 4

DISCUSSION

4.1 MEASUREMENT UNCERTAINTIES

There are various effects in the measurement system that are not considered in Equation 3.4, and these effects could potentially contribute to the uncertainties of the refractive index measurement. Table 4.5 shows the different factors contributing to refractive index errors and their worst-case estimates. The sum of uncertainty was $\Delta n_{\text{sum}} < 0.9 \times 10^{-3}$. Below, the details of the evaluation for each factor are described.

1. Δn_1 caused by the lateral shift of the collimated measurement beam due to the vacuum window.

2. Δn_2 caused by the change in α due to the tilt of the sample prism.

3. Δn_3 caused by the angular measurement error of the encoder.

Additionally, this section also describes the results of measurements for CaF_2 and N-BK7, whose refractive indices in the visible light range are well known, to verify the measurement accuracy of the apparatus.

The method for calculating the refractive index error Δn from the error in the minimum deviation angle $\Delta\delta$ is described in the Appendix **??**.

4.1.1 Lateral shift of the collimated measurement beam due to the vacuum window

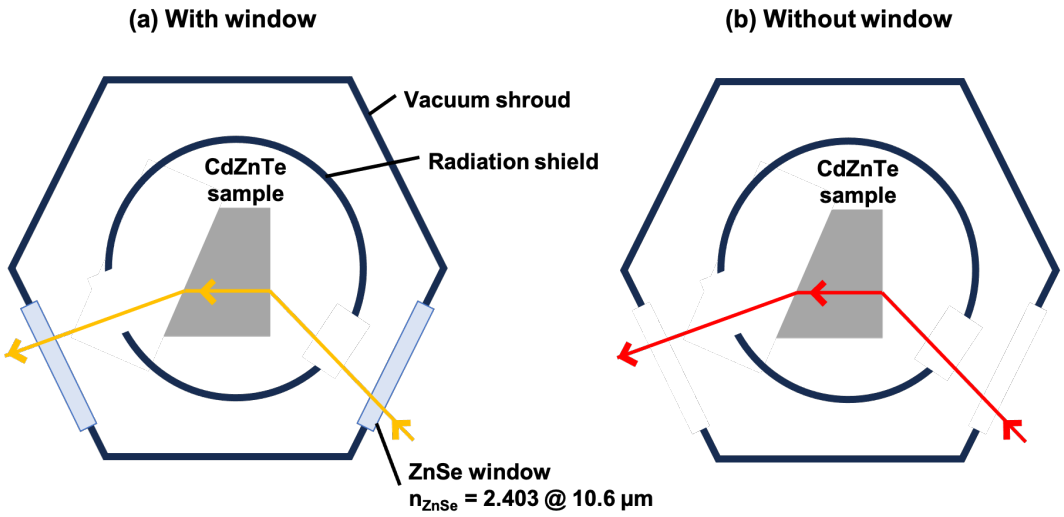

Figure 4.1: Schematic diagram show the refractive index measurement of the CdZnTe sample with (a) and without (b) the ZnSe vacuum window. The red line represents the measurement beam in the absence of the window, while the orange line represents the measurement beam affected by the ZnSe vacuum window.

First, we describe the refractive index error Δn_2 caused by the ZnSe vacuum window. As shown in Figure 4.1 (a), during cryogenic experiments, 3-mm-thick ZnSe windows (with a refractive index of $n_{\mathrm{ZnSe}} = 2.3950$ at 10.6 μm [41]) were used on both the incident and outgoing sides. To investigate the effect of the ZnSe vacuum window on refractive index measurements, experiments were conducted under the following two conditions. Both measurements were performed at room temperature and atmospheric pressure:

- Refractive index measurement with ZnSe windows, as shown in Figure 4.1 (a).
- Refractive index measurement without ZnSe windows, as shown in Figure 4.1 (b).

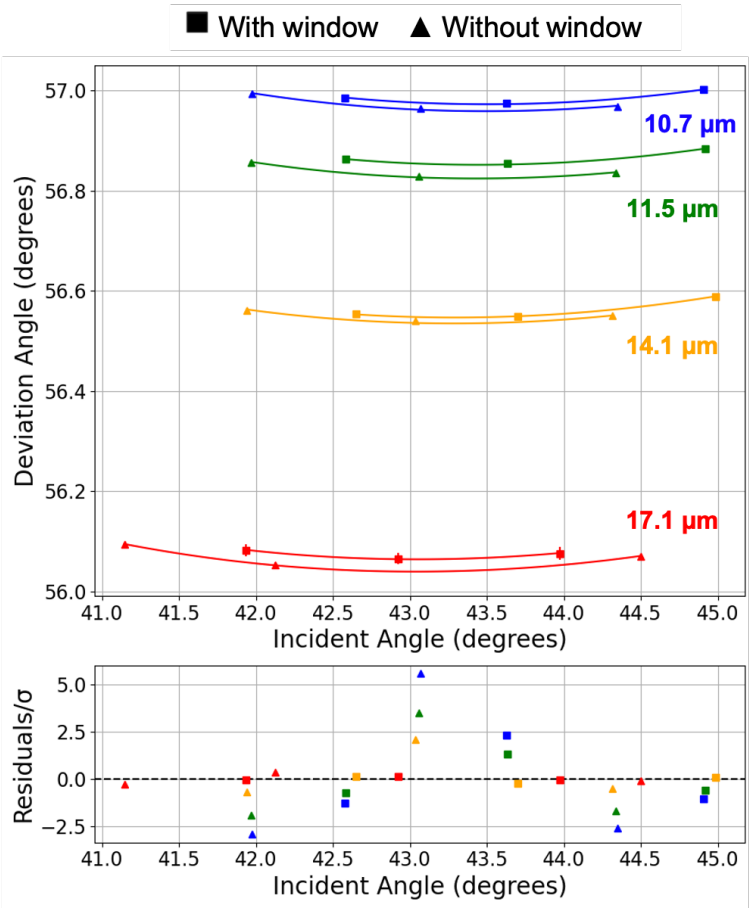

Figure 4.2: Squares represent the refractive index measurement results with the ZnSe vacuum window, while triangles represent the results without the window. Each plot was fitted using an Equation 3.4, and the order of the residuals was approximately the same for both cases. Additionally, the color differences represent variations in the measurement wavelengths.

n with the ZnSe window is n_a, and n without the window is n_b.

Figure 4.2 shows the results of each measurement. Comparing the results of deviation angle measurements with and without the window, it is found that n is higher for all wavelengths when the window is present. And Table 4.1 shows the corresponding fitting results.

The refractive indices n_a and n_b, measured under atmospheric pressure, are relative refractive index with respect to the refractive index of air n_{air} ($= 1.00027$ [47]). Therefore, the absolute refractive index n_{abs} were calculated using the corresponding Equation 4.1.

$$n_{\text{abs}} = n_{\text{air}} \times n_{\text{measured in air}}, \tag{4.1}$$

And Δn in Table 4.1 represents the values considering only the statistical error.

The measurement results reveal that the systematic error in the refractive index measurement caused by the presence of the window, derived from $n_a - n_b$, is $\Delta n_{\mathrm{mea}} < 0.7 \times 10^{-3}$.

Table 4.1: Comparison of refractive index measurements with and without ZnSe window

BPF (μm)	**(a) With window**			**(b) Without window**			
	n_a	$n_{a,\mathrm{abs}}$	Δn_a	n_b	$n_{b,\mathrm{abs}}$	Δn_b	$n_a - n_b$
10.6	2.65688	2.65688	0.03×10^{-3}	2.65654	2.65654	0.14×10^{-3}	0.34×10^{-3}
11.4	2.65392	2.65392	0.04×10^{-3}	2.65325	2.65325	0.14×10^{-3}	0.67×10^{-3}
14.0	2.64645	2.64645	0.01×10^{-3}	2.64616	2.64616	0.13×10^{-3}	0.29×10^{-3}
17.1	2.63458	2.63458	0.04×10^{-3}	2.63397	2.63397	0.15×10^{-3}	0.61×10^{-3}

To verify whether $\Delta n_{\mathrm{mea}} < 0.7 \times 10^{-3}$ is reasonable, I used Snell's law and geometry to formulate Equation 4.2 – 4.29. The refractive index outside the ZnSe vacuum window is n_{air} because of the presence of air, while the refractive index inside it is n_0 because of the vacuum.

Here, $n_{\mathrm{air}} - n_0 = 0.27 \times 10^{-3}$ was assumed. Additionally, the difference between θ_1 near the minimum deviation angle ($-1^\circ < \theta_3 < 1^\circ$) and the angles θ_4 and θ_4' was evaluated as the refractive index error. Note that the vacuum window is a parallel flat plate, Thus although the collimated measurement beam may shift, it does not affect the angle and is not included in the calculations here.

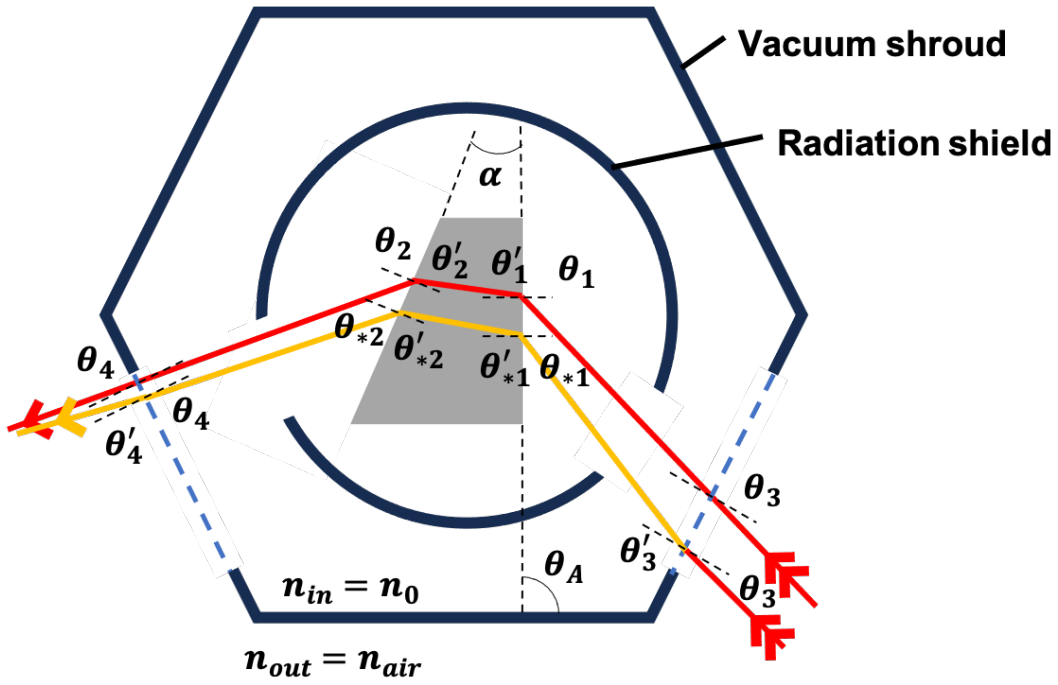

Figure 4.3: Schematic diagram of the measurement beam passing through the vacuum shroud. The orange line L_2 is refracted at the boundary of the vacuum window due to the difference in refractive index between the vacuum and the atmosphere.

The refractive indices inside and outside the shroud are n_{in} and n_{out}, respectively. The red line L_1 represents the measured beam when $n_{\text{in}} = n_{\text{out}}$, and the orange line L_2 represents the measured beam when $n_{\text{in}} \neq n_{\text{out}}$ in Figure 4.3.

To solve for the measurement beam L_1 using Snell's law: When the measurement beam enters the CdZnTe sample:

$$n_{\text{air}} \cdot \sin\theta_1 = n_{\text{CdZnTe}} \cdot \sin\theta_1', \tag{4.2}$$

$$\sin\theta_1' = \frac{n_{\text{air}} \cdot \sin\theta_1}{n_{\text{CdZnTe}}}, \tag{4.3}$$

$$\theta_1' = \sin^{-1}\left(\frac{n_{\text{air}}}{n_{\text{CdZnTe}}} \cdot \sin\theta_1\right). \tag{4.4}$$

When the measurement beam exits from the CdZnTe sample:

$$n_{\text{CdZnTe}} \cdot \sin\theta_2' = n_{\text{air}} \cdot \sin\theta_2, \tag{4.5}$$

$$\sin\theta_2 = \frac{n_{\text{CdZnTe}} \cdot \sin\theta_2'}{n_{\text{air}}}, \tag{4.6}$$

$$\theta_2 = \sin^{-1}\left(\frac{n_{\text{CdZnTe}}}{n_{\text{air}}} \cdot \sin\theta_2'\right). \tag{4.7}$$

Additionally, the geometric relationship is given by:

$$\alpha = \theta_1' + \theta_2', \tag{4.8}$$

$$\theta_4 = -\theta_A + -\alpha - \theta_2 + \theta_{\text{hex}}. \tag{4.9}$$

Here, θ_{hex} is the interior angle of a regular hexagon, which equals 120°, and θ_A is the installation angle of the vacuum shroud and the prism, determined through measurement. Variations in θ_A of approximately ±2.5° have no effect on the error in the refractive index.

To solve for the measurement beam L_2 using Snell's law: When the measurement beam enters the vacuum shroud:

$$n_{\text{air}} \cdot \sin\theta_3 = n_0 \cdot \sin\theta_3', \tag{4.10}$$

$$\sin\theta_3' = \frac{n_{\text{air}} \cdot \sin\theta_3}{n_0}, \tag{4.11}$$

$$\theta_3' = \sin^{-1}\left(\frac{n_{\text{air}} \cdot \sin\theta_3}{n_0}\right). \tag{4.12}$$

When the measurement beam enters the CdZnTe sample:

$$n_0 \cdot \sin\theta_{*1} = n_{\text{CdZnTe}} \cdot \sin\theta_{*1}', \tag{4.13}$$

$$\sin\theta'_{*1} = \frac{n_0}{n_{\mathrm{CdZnTe}}} \cdot \sin\theta_{*1}, \tag{4.14}$$

$$\theta'_{*1} = \sin^{-1}\left(\frac{n_0}{n_{\mathrm{CdZnTe}}} \cdot \sin\theta_{*1}\right). \tag{4.15}$$

When the measurement beam exits the CdZnTe sample:

$$n_{\mathrm{CdZnTe}} \cdot \sin\theta'_{*2} = n_0 \cdot \sin\theta_{*2}, \tag{4.16}$$

$$\sin\theta_{*2} = \frac{n_{\mathrm{CdZnTe}}}{n_0} \cdot \sin\theta'_{*2}, \tag{4.17}$$

$$\theta_{*2} = \sin^{-1}\left(\frac{n_{\mathrm{CdZnTe}}}{n_0} \cdot \sin\theta'_{*2}\right). \tag{4.18}$$

From the geometric relationships:

$$\alpha = \theta'_{*1} + \theta_{*2}, \tag{4.19}$$

$$\theta_{*1} = \theta_A + \theta'_3 - (180^\circ - \theta_{\mathrm{hex}}). \tag{4.20}$$

$$\theta_4 = \theta_{*2} + \theta_A - \alpha - \theta_{\mathrm{hex}}. \tag{4.21}$$

Finally, when the beam exits the shroud:

$$n_0 \cdot \sin\theta'_4 = n_{\mathrm{air}} \cdot \sin\theta_4, \tag{4.22}$$

$$\sin\theta'_4 = \frac{n_0}{n_{\mathrm{air}}} \cdot \sin\theta_4, \tag{4.23}$$

$$\theta_4' = \sin^{-1}\left(\frac{n_0}{n_{\text{air}}} \cdot \sin\theta_4\right). \tag{4.24}$$

For the entry angle θ_{*1}'' and exit angle θ_{*2}'' of the sample in L_2, they are expressed as:

$$\theta_{*1}'' = \theta_{*1} + (\theta_3' - \theta_3), \tag{4.25}$$

$$\theta_{*2}'' = \theta_{*2} + (\theta_4' - \theta_4). \tag{4.26}$$

Thus, the deviation angles δ_{L1} and δ_{L2} for L_1 and L_2, respectively, are given by:

$$\delta_{L1} = \theta_1 + \theta_2 - \alpha, \tag{4.27}$$

$$\delta_{L2} = \theta_{*1}'' + \theta_{*2}'' - \alpha. \tag{4.28}$$

Finally, the difference in deviation angles $\Delta\delta_L$ is:

$$\Delta\delta_L = \delta_{L1} - \delta_{L2}. \tag{4.29}$$

α is 30.033°, the refractive index of CdZnTe n_{CdZnTe} is 2.6625, the refractive index of air n_{air} is 1.0003, and the refractive index in vacuum n_0 is 1. When θ_A is 102.772°, the error in the minimum deviation angle $\Delta\delta < 0.033°$. From this angle error, the refractive index error Δn_{cal} was calculated to be $\Delta n_{\text{cal}} < 0.8 \times 10^{-3}$. This result did not change even when n_{CdZnTe} was adjusted by ± 0.02.

The refractive index error from the measurement, Δn_{mea}, and the error from the calculation, Δn_{cal}, were of a similar magnitude: $\Delta n_{\text{mea}} < 0.7 \times 10^{-3}$ and $\Delta n_{\text{cal}} < 0.8 \times 10^{-3}$. In this study, the experimentally obtained refractive index error, Δn_{mea}, is defined as Δn_{u2}.

4.1.2 Angular measurement error of the encoder

The angular measurement error caused by the encoder, treated as a random error, is $\theta_{u3} = \pm 0.6 \times 10^{-3}$ degree. The encoder used is the Heidenhain RON806, and θ_{u3} is based on its specifications. The error in the refractive index n_{u3} is converted to $\Delta n_{u3} = 0.1 \times 10^{-3}$.

4.1.3 Change in the apex angle due to the tilt of the sample prism

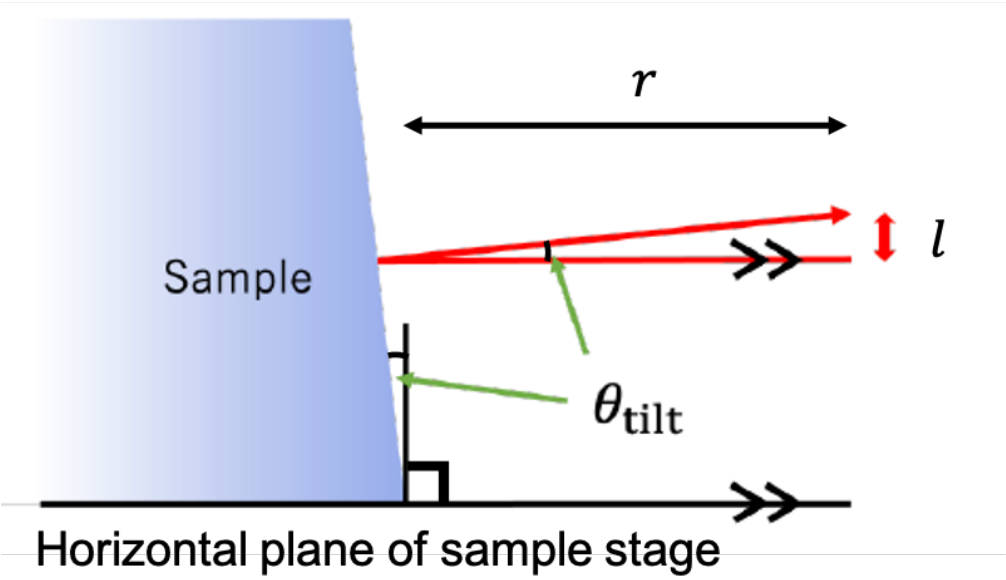

Figure 4.4: Schematic diagram of sample tilt measurement

Moreover, we explain the angular error θ_{u4} caused by the tilt of the sample around the vertical axis. When a tilt θ_{tilt} occurs, α changes to α as shown in Equation 4.30. Since a change in α affects the deviation angle δ in Equation 1.10, it introduces an angular error as

$$\alpha' = \frac{\alpha}{\cos\theta_{\text{tilt}}}. \tag{4.30}$$

When the θ_{tilt} is less than or equal to 1 degree, the refractive index error is evaluated as $\Delta n \leq 0.1 \times 10^{-3}$ based on Equation 1.10. In practice, we confirmed that the tilt was less than 1 degree using an auto-collimation measurement.

4.1.4 The effect of the exit-side orifice on deviation angle measurements

In the measurement system, as shown in Figure 4.5, orifices with an aperture of 5 mm are installed on both the incident and outgoing side. The incident-side orifice is placed to reduce the diameter of the collimated measurement beam to 5 mm. The exit-side orifice would not pose any issue if the collimated measurement beam passes through the ideal optical path. However, the presence of the ZnSe vacuum window causes the collimated measurement beam to deviate from the ideal optical path, potentially resulting in the beam being clipped by the orifice.

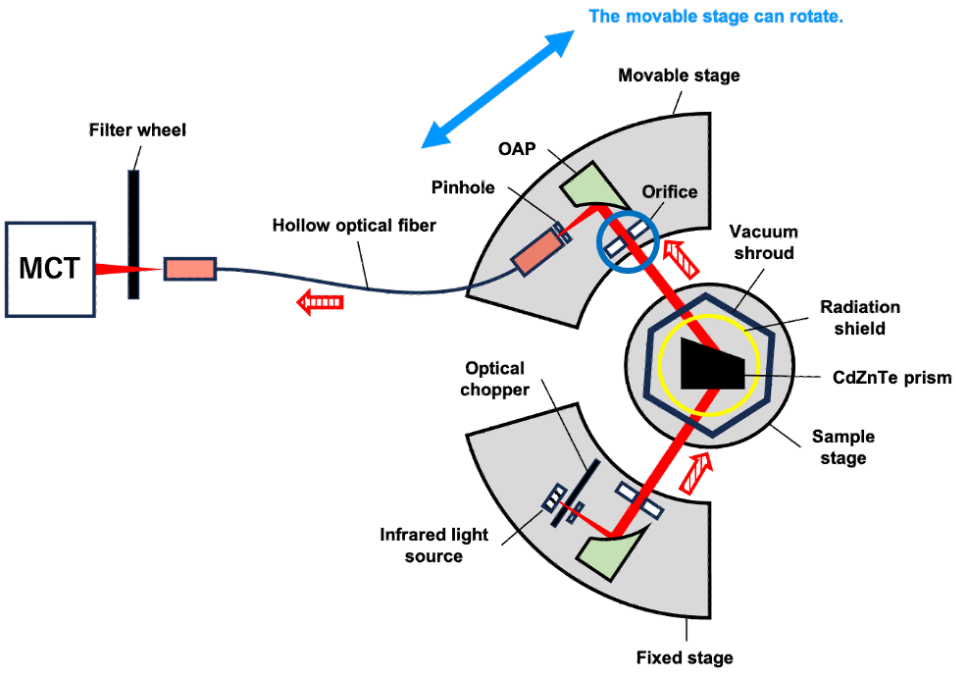

Figure 4.5: Schematic diagram of the deviation angle measurement. The part enclosed in the blue circle represents the exit-side orifice.

Here, to clarify the effect of beam Vignetting caused by the outgoing side orifice on the refractive index measurement, deviation angle measurements of the CdZnTe sample were performed under the following two conditions. Both measurements were performed at room temperature and atmospheric pressure:

- The outgoing side orifice aperture of 20 mm

- The outgoing side orifice orifice aperture of 5 mm

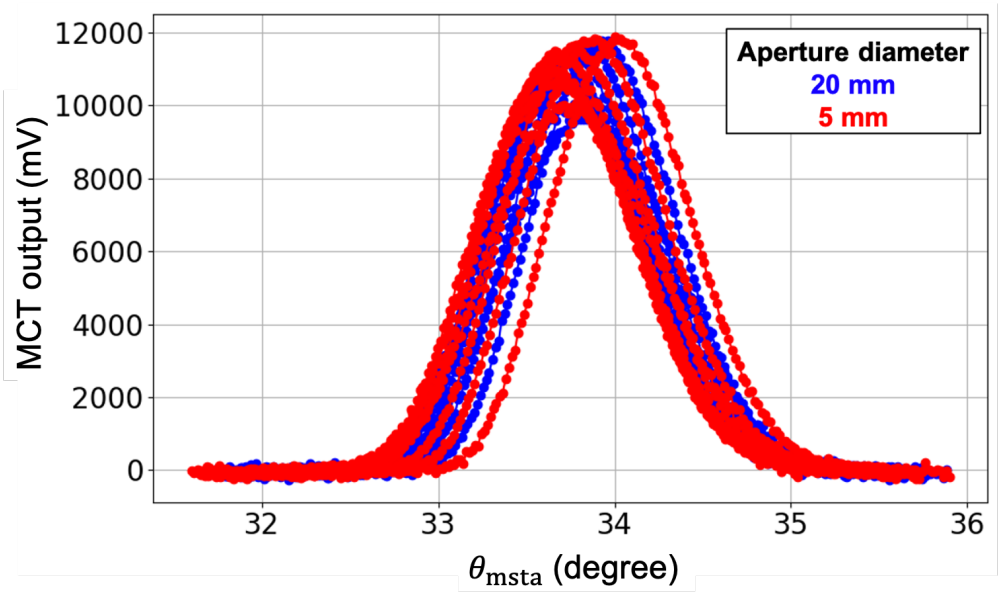

Figure 4.6: Measurement results of δ with an exit-side orifice aperture of 20 mm (blue) and 5 mm (red)

Figure 4.6 shows the results of deviation angle measurements with the exit-side orifice aperture set to 20 mm (blue) and 5 mm (red). From these results, it was found that there is no significant difference in the MCT output values between the 20 mm (blue) and 5 mm (red) orifice apertures. Figure 4.7 shows the results of fitting the deviation angle measurements to the corresponding Equation 3.4. The residuals of the fittings were of the same order. The refractive indices of the CdZnTe sample obtained from these fittings are listed in Table 4.2. When the orifice aperture was 20 mm, δ was larger than that for the 5 mm aperture, with a difference of $\Delta\delta = 0.047°$. Considering only statistical error Δn_{sta}, a significant difference in refractive indices was observed between the 20 mm and 5 mm orifice apertures. However, when systematic error Δn_{sys} is also included, no significant difference in refractive indices was observed. Therefore, the influence of Vignetting caused by the exit-side orifice is negligible.

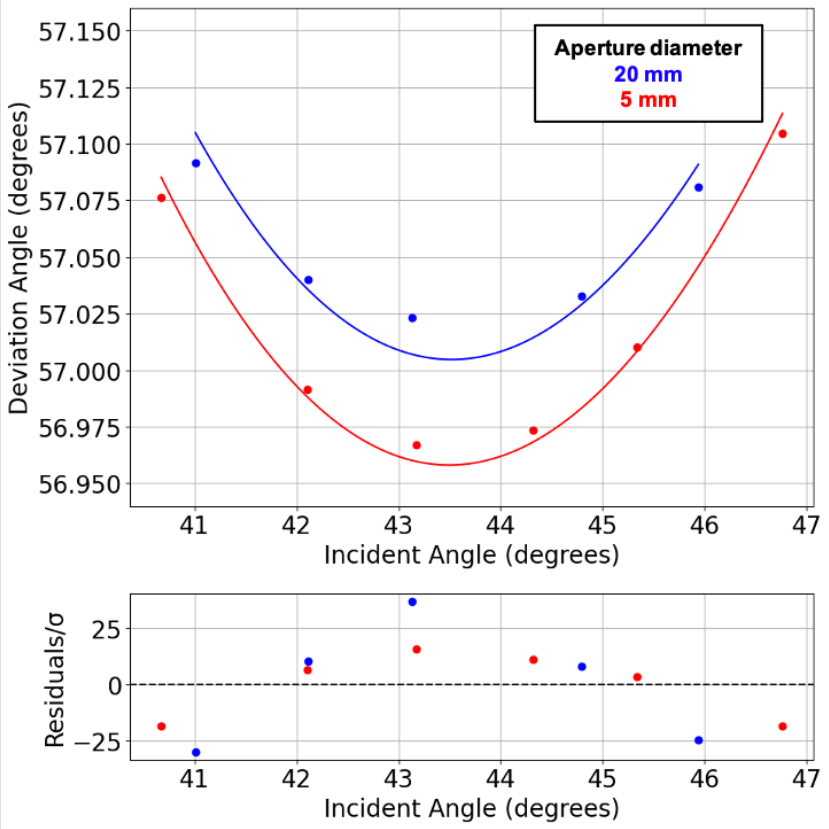

Figure 4.7: The top panel shows the measurement results of δ of the CdZnTe sample at room temperature and a wavelength of 10.6 μm with an orifice aperture of 20 mm (blue) and 5 mm (red), along with the fitting curves based on Equation 3.4. The bottom panel displays the residuals for each fitting. Here, σ represents the fitting error obtained from the deviation angle measurements (4.6).

Table 4.2: Deviation angle and refractive index for different aperture diameters

Parameter	**20 mm**	**5 mm**
$\alpha(°)$	43.498	43.503
$\delta(°)$	57.005	56.958
n	2.65765	2.65651
Statistical error $\Delta n_{\mathbf{sta}}$	1.5×10^{-4}	0.8×10^{-4}
Systematic error $\Delta n_{\mathbf{sys}}$	1.6×10^{-3}	1.6×10^{-3}
Sum error Δn	1.8×10^{-3}	1.7×10^{-3}

Additionally, for the case of the aperture diameter of 5 mm on the outgoing side, no significant difference from the previous measurement results was observed within the range of the statistical error Δn_{sta}, confirming the high reproducibility of the measurements.

4.1.5 Misalignment for calibration measurement

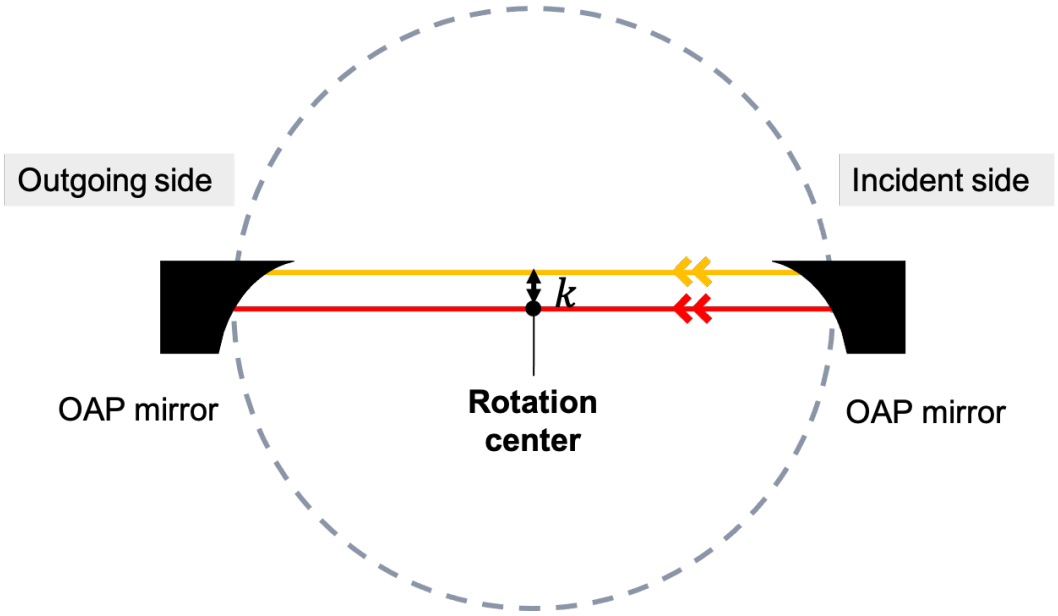

Figure 4.8: The schematic diagram shows the misalignment for calibration measurement. The red line represents the measurement collimated beam through the center, and the orange line represents the collimated beam shifted k in the lateral direction. The collimated beam is made by the OAP mirror on the incident side. The collimated beam is then reduced to 5 mm in diameter by an orifice (omitted in Figure) immediately behind it. On the outgoing side, there is the OAP mirror to focus the collimated beam.

The error to the refractive index caused by a misalignment for calibration measurement are discussed in Figure 4.8. Due to the characteristics of the optical system, there is no error in deviation angle measurement due to lateral shift k of the measurement collimated beam. Even if the collimated beam shifts k from the center of rotation, the focal point remains the same because the collimated beam is focused by the OAP mirror on the outgoing side. Therefore, since the diameter of the collimated beam is 5 mm, in principle, k can be shifted up to 2.5 mm without affecting the angle measurement. In the measurement, k is about 0.1 mm, Therefore it does not affect the angle measurement and does not cause refractive index errors.

4.1.6 Deflection of the ZnSe vacuum window

The impact of the deflection of the ZnSe vacuum window is explained. Due to the pressure difference between the atmospheric pressure and the vacuum level inside the vacuum shroud, the window deflects inward as shown in Figure 4.9.

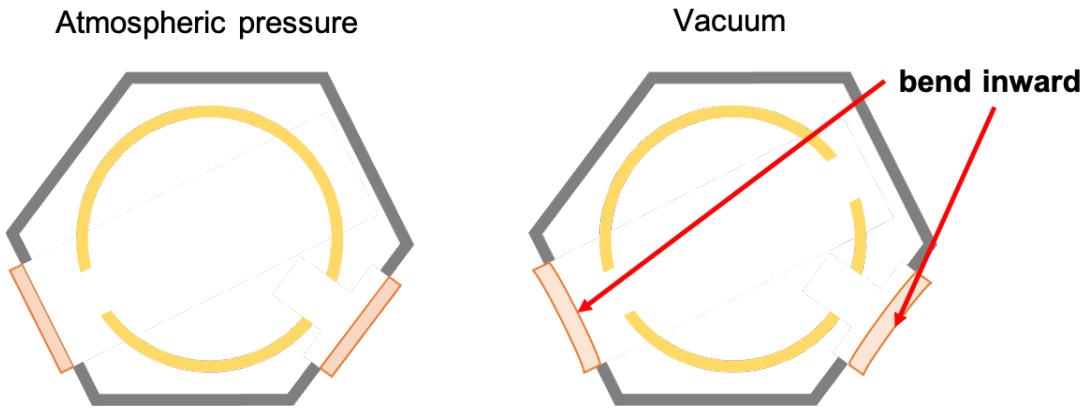

Figure 4.9: Schematic diagram showing the case where the inside of the vacuum shroud is at atmospheric pressure (left) and in vacuum (right). In the vacuum case, the ZnSe vacuum window bends inward toward the inside of the vacuum shroud.

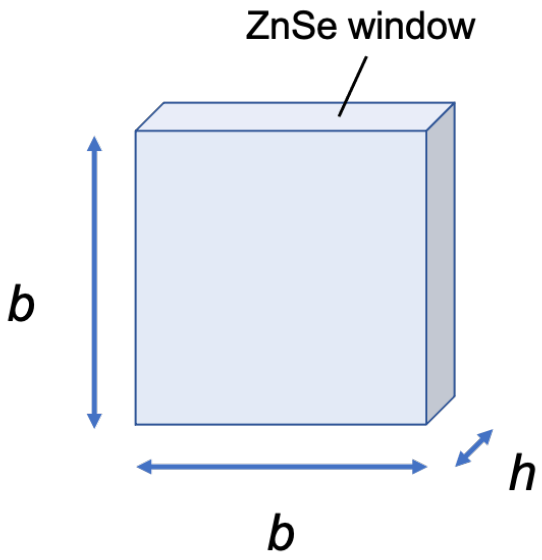

Figure 4.10: The ZnSe vacuum window approximated as a square with a side length b and thickness h

Although the window is actually circular, it is approximated here as a square with a side length b and thickness h (see Figure 4.10). Using the Equation 4.31–4.33, the

maximum inward deflection $y_{\max}$ of the window is calculated. I represents the second moment of area, and w represents the uniformly distributed load per unit length. And Table 4.3 explains each parameter.

$$y_{\max} = \frac{5wl^4}{384EI} \quad \left[\frac{\mathrm{N/m \cdot m^4}}{\mathrm{N/m^2 \cdot m^4}}\right], \tag{4.31}$$

$$I = \frac{bh^3}{12} \quad [\mathrm{m^4}], \tag{4.32}$$

$$w = bP \quad \left[\mathrm{m} \cdot \frac{\mathrm{N}}{\mathrm{m^2}}\right]. \tag{4.33}$$

Table 4.3: Definition of Parameters

Parameter	value	**Description**
$E\ [N/m^2]$	6.72×10^{-12}	Young's modulus of ZnSe
$I\ [m^4]$	45×10^{10}	Second moment of area
$w\ [N/m]$	2026.5	Uniformly distributed load per unit length
$l\ [m]$	20×10^{-3}	Length of the beam
$b\ [m]$	20×10^{-3}	Length of one side
$h\ [m]$	3×10^{-3}	Thickness
$P\ [Pa]$	101.325	Atmospheric pressure

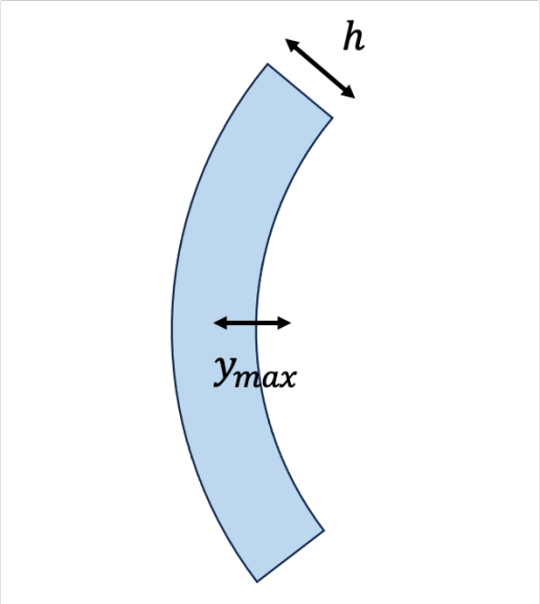

Figure 4.11: Cross-sectional view of the ZnSe vacuum window when deflected by $y_{\max}$

As a result of the calculation, $y_{\max}$ is 1.4×10^{-6} m. As shown in Figure 4.11, the window deflects, but $y_{\max}$ is extremely small compared to the window thickness of 3.0×10^{-3} m and can be neglected.

4.1.7 Verification of the measurement accuracy of the system

To verify the measurement accuracy of the apparatus, samples of CaF_2 and N-BK7 (Figure 4.12), whose refractive indices are well known in the visible light range, were measured. For the CaF_2 and N-BK7 samples, calibration measurements, apex angle measurements, and deviation angle measurements were performed using the same procedures described in Chapter 3. These measurements were performed using a visible laser with a wavelength of 635 nm, under room temperature and atmospheric pressure conditions without the shroud. n_{abs} for each sample, obtained from these measurements, is shown in Table 4.4. And Δn represents the values considering only the statistical error.

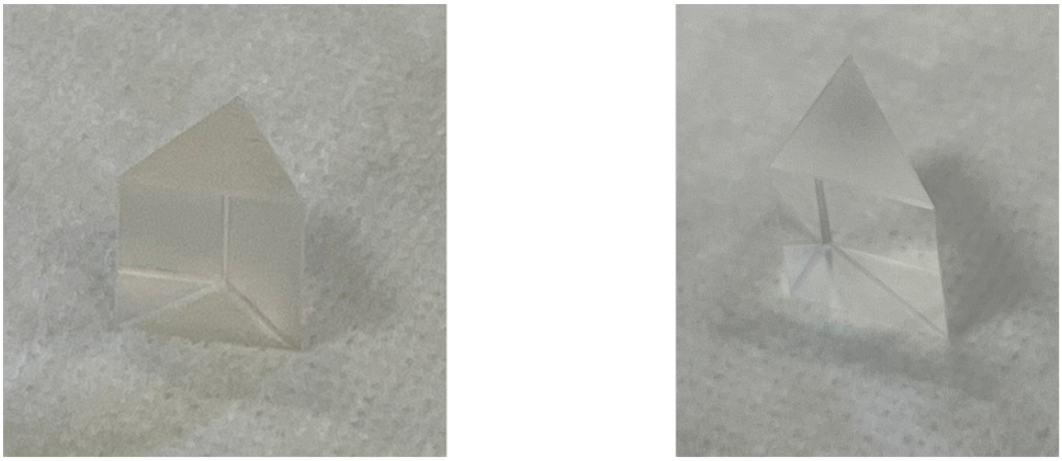

Figure 4.12: Photos of (left) CaF_2 and (right) N-BK7.

Table 4.4: CaF_2 and N-BK7 of α and refractive index n at 635 nm

Material	$\alpha_{\mathbf{mea}}$ (°)	$n_{\mathbf{abs}}$
CaF_2	59.969 ± 0.003	1.43397 ± 0.0004
N-BK7	44.892 ± 0.006	1.51654 ± 0.0007

n of CaF_2 was measured by Douglas B et al [42]. They measured at a temperature range between 25 K and 300 K and a wavelength range between 0.4 and 5.6 μm. The uncertainty in their measurement at 295 K and 500 nm was $\pm 1.7 \times 10^{-5}$. The deviation between our measurement and the linearly interpolated value from Douglas B et al.'s data at 635 nm was 0.7×10^{-3}.

Additionally, the refractive index measurements of N-BK7 were compared with the data sheet provided by SCHOTT [43]. Since the data sheet did not specify the measurement uncertainty, we estimated it to be $\pm 0.3 \times 10^{-4}$ based on the significant figures. The deviation between our measurement and the linearly interpolated value from the data sheet at 635 nm was 0.5×10^{-3}.

From the above discussion, it is considered that the measurement accuracy of this apparatus at room temperature and a wavelength of 635 nm is at most 0.7×10^{-3}.

In this study, measurements to verify the measurement accuracy at low temperatures and in infrared region were not conducted. However, we estimate it based on previous

discussions on uncertainty evaluation. Since the uncertainty increases due to the vacuum shroud in measurements at low temperatures and in the infrared region, we estimate the accuracy to be at most 1.4×10^{-3}.

4.1.8 Summary of uncertainties investigation

Table 4.5 shows a list of the various uncertainties examined in this section 4.1. The temporal stability of the light source and detector was evaluated as part of the statistical error by performing multiple measurements in this experiment. The sum of uncertainty Δn_{sum} was calculated by linearly summing the errors, resulting in a sum of error of $\Delta n_{\mathrm{sum}} < 0.9 \times 10^{-3}$. Adding the statistical error from fitting to this value, the total error in refractive index is $\Delta n_{\mathrm{total}} < 1.3 \times 10^{-3}$. This value approximately satisfies the required measurement accuracy of $\Delta n_{\mathrm{req}} < 10^{-3}$ for the system.

However, the following sources of error were considered minor and are not numerically evaluated in this paper:

- Radiation cooling of the vacuum window causes a temperature distribution within the window. This temperature distribution results in n distribution, which in turn affects the collimated beam used for measurement, but the effect is small.
- Due to cooling, the prism contracts. The change in α due to this contraction introduces errors in n. Since CdZnTe is a single crystal, it is assumed to contract uniformly, and therefore, this error is considered to be small.
- Refractive index errors due to temperature stability: During measurements, the temperature stability was at most $\Delta T \sim 0.2$ K. The temperature dependence of the refractive index is $\frac{\Delta n}{\Delta T} \sim 10^{-4}$, Therefore the refractive index variation due to temperature stability is $\Delta n \sim 10^{-5}$. Therefore, the effect is small.
- Refractive index errors due to vacuum stability: The vacuum level varies depending on the measurement temperature. At room temperature and atmospheric pressure, the error is ± 0.1 Pa; in a vacuum, it is $\pm 3.0 \times 10^{-3}$ Pa; at 50 K, it is $\pm 3.0 \times 10^{-4}$

Pa; at 20 K, it is $\pm 3.0 \times 10^{-3}$ Pa; and at 12 K, it is $\pm 0.3 \times 10^{-4}$ Pa. A 1 hPa change in atmospheric pressure causes a change of approximately 0.3 ppm in the refractive index of air. Therefore, the impact of the vacuum stability error on n is considered to be small.

- Regarding the reproducibility and long-term stability of the angle measurement, n under the same measurement conditions agrees with a precision of $\Delta n < 10^{-3}$. Since the required measurement precision is satisfied, the reproducibility and long-term stability of the angle measurement are good.

- The alignment accuracy of the OAP mirrors and fibers is related to the collimation of the measured collimated light. For visible light, a collimated beam with a diameter of 5 mm will become 10 mm in diameter at a distance of 5 m. The behavior for infrared light remains unverified. We consider the alignment to be matched by machine precision.

- The surface precision of the prism affects the refractive index measurement. The Rayleigh limit, which assumes that if the maximum wavefront aberration of a lens is less than $\frac{\lambda}{4}$, the lens is considered ideal, is used as a criterion. The maximum wavefront aberrations of the samples measured in this study are $\frac{\lambda}{11}$ on surface A and $\frac{\lambda}{4}$ on surface B. Therefore, the impact of the prism's surface precision on the refractive index measurement is considered small.

- The light emitted from the fiber is not a perfect point source, Thus there should be aberrations. These aberrations affect the profile of the measured light, leading to errors in the refractive index.

4.1.9 Comparison of measurement accuracy

In this section, the measurement accuracy of the present measurement system (see Figure 4.13) is compared with that of the measurement system described in Ymamuro et al. (2006) [29]. He introduces two remarkable error sources leading to uncertainty in the

Table 4.5: List of the measurement uncertainties

Δn_i	$\Delta\theta_{\mathrm{ui}}(degree)$	Description
$\Delta n_1 < 0.7 \times 10^{-3}$	$\theta_{\mathrm{u1}} < 6.0 \times 10^{-2}$	Angular error due to lateral displacement of the measurement beam caused by the vacuum window, 3 mm thick ZnSe window with high refractive index ($n = 2.403$ @ 10.6 µm)
$\Delta n_2 = 0.1 \times 10^{-3}$	$\theta_{\mathrm{u2}} = 6.0 \times 10^{-4}$	Specification of the encoder error
$\Delta n_3 < 0.1 \times 10^{-3}$	$\theta_{\mathrm{u3}} < 1.0 \times 10^{-4}$	Angular error caused by an increase in the distance the collimated measurement beam passes through due to the tilt between the prism surfaces
$\Delta n_{sum} < 0.9 \times 10^{-3}$	$< 6.1 \times 10^{-2}$	Sum of all uncertainties

measured refractive indices. Among the 20 optical materials measured, the refractive index measurement error of KRS-5, which has the highest refractive index in the infrared region, is compared.

- **Optical Aberration**

  Coma aberration of the collimator and telemeter causes a shift in the intensity profile on the detector. This shift leads to angular errors of approximately ±20 arcseconds (about 0.005°) in α and $\delta_{\min}$. These two angular errors result in an error of $\Delta n < 0.3 \times 10^{-3}$.

- **Deformation of the Detector Cryostat**

  Relative movement between the detector and the slit within the cryostat causes angular errors. This angular error is estimated to be ±12 arcseconds (about 0.003°). When converted to the error in the refractive index gradient, it corresponds to $\Delta n(T) < 0.1 \times 10^{-3}$.

Thus, the error in refractive index measurements at low temperatures is $\Delta n < 0.4 \times 10^{-3}$. In contrast, the error in this study is $\Delta n_{\text{total}} < 1.3 \times 10^{-3}$, which is one order of magnitude worse. The following two reasons are considered to account for this discrepancy:

- In Ymamuro et al. (2006), prisms are symmetrically placed with respect to the sample cooling cryostat window. Since the prisms are symmetric in shape, they are easy to install. Unlike the method used in this system to derive $\delta_{\min}$, a method that directly captures $\delta_{\min}$ is employed. At $\delta_{\min}$, θ_1 and the exit angle are equal. Therefore, the symmetric arrangement cancels out the effects of the window. There is no equivalent to the error due to the vacuum shroud window Δn_1, which is the largest error factor in this measurement system.

- Misalignment in the perpendicular direction to the rotation axis of the optical axis plane and angular measurement errors are considered negligible in comparison to the "two major error sources." Therefore, there is no equivalent to Δn_3 and Δn_4 errors in this measurement system.

In this way, if the refractive index error Δn_1 caused by the vacuum window, which is the main error factor in this measurement system, can be eliminated, the refractive index error would become comparable to that of Yamamuro et al. (2006). In this measurement method, δ is measured while varying θ_1 to the sample. Therefore, it is considered that Δn_1 depends on θ_1. If this θ_1 dependence can be incorporated into the fitting code, it is expected that Δn_1 can be eliminated as an error factor.

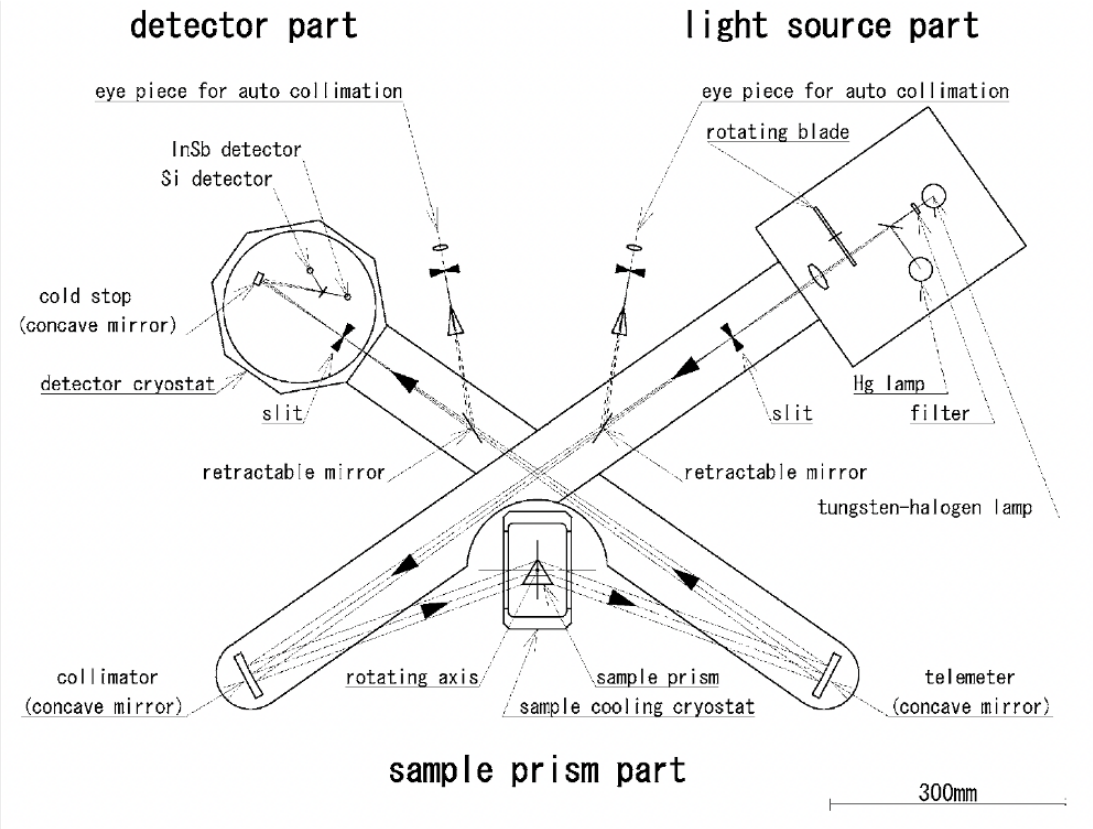

Figure 4.13: This diagram is the Measurement system of Yamamuro et al. 2006. Figure 3 in [29]

4.2 Temperature dependence of refractive index

In this section, we discuss the temperature dependence of n of CdZnTe. Figure 4.14 shows the temperature dependence of the refractive indices of CdZnTe at wavelengths of 10.6, 11.4, 14.0, and 17.1 μm. The temperature dependence of the refractive indices of CdZnTe was obtained by linear fitting to the refractive indices at each wavelength (Table 4.6), and it was found that the temperature dependence of the refractive indices of CdZnTe

varies with wavelength, becoming larger with increasing wavelength. On the other hand, when the temperature dependence is obtained by linear fitting to the refractive indices from cryogenic to room temperature, the difference with wavelength is small. Therefore, to obtain the temperature dependence of n with high accuracy, it is necessary to measure n at many temperatures.

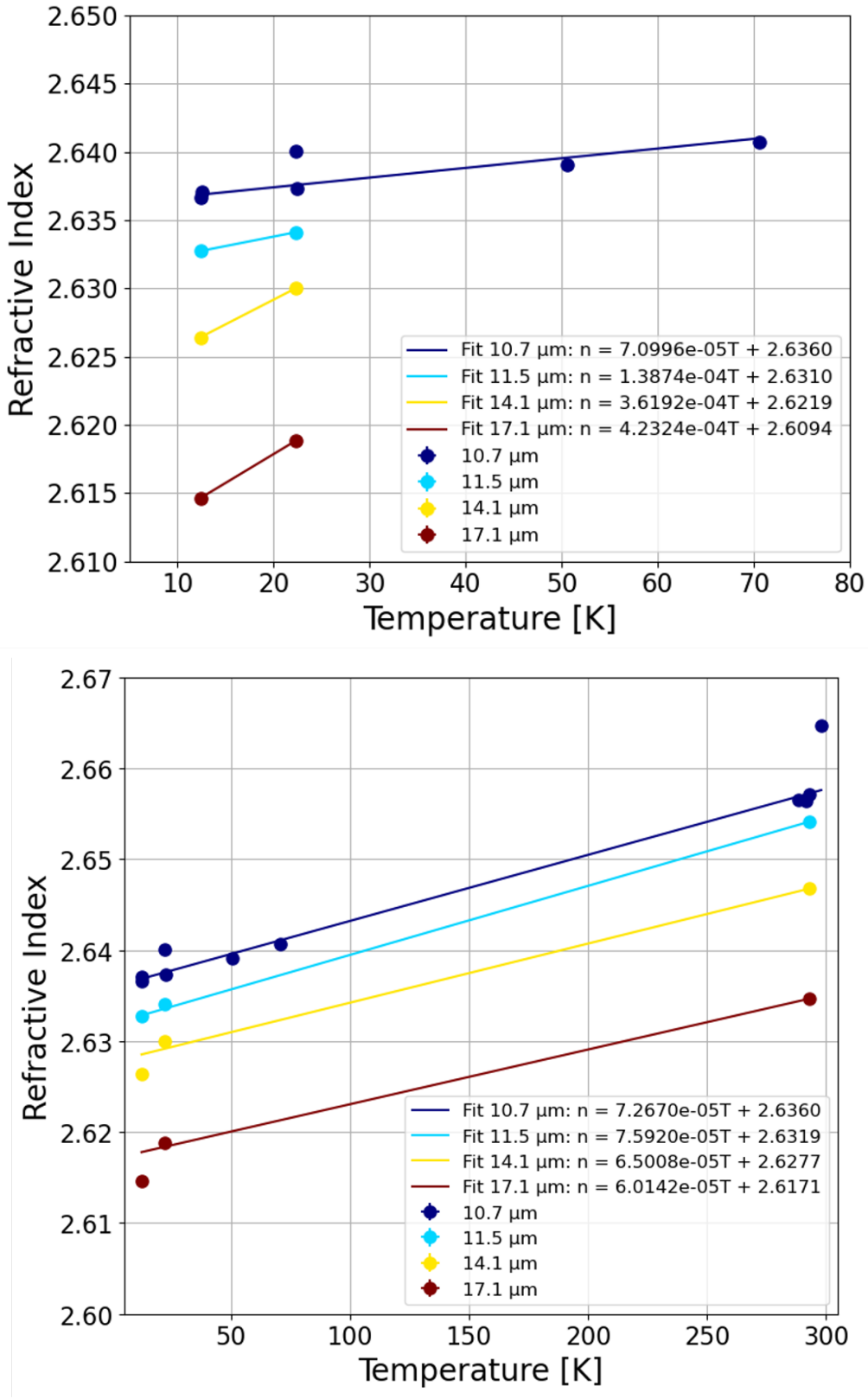

Figure 4.14: The temperature dependence of n of CdZnTe at wavelengths of 10.6, 11.4, 14.0, and 17.1 μm. The top panel shows the results of a linear fit (solid line) to n (dots) only at cryogenic temperatures. The bottom panel shows the results of a linear fit from cryogenic to room temperatures.

Table 4.6: Temperature dependence of the refractive index of CZT at different wavelengths

Wavelength (µm)	Temperature range (K)	$\frac{\Delta n_{\mathrm{CZT}}}{\Delta T}$
10.6	12.4 – 70.6	$(7.1 \pm 0.2) \times 10^{-5}$
	12.4 – 292.8	$(7.27 \pm 0.01) \times 10^{-5}$
11.4	12.4 – 22.3	$(13.9 \pm 2.0) \times 10^{-5}$
	12.4 – 292.8	$(7.59 \pm 0.03) \times 10^{-5}$
14.0	12.4 – 22.3	$(36.2 \pm 1.5) \times 10^{-5}$
	12.4 – 292.8	$(6.50 \pm 0.03) \times 10^{-5}$
17.1	12.4 – 22.3	$(42.3 \pm 3.8) \times 10^{-5}$
	12.4 – 292.8	$(6.01 \pm 0.07) \times 10^{-5}$

Figure 4.15 shows the temperature dependence of n of CdTe at a wavelength of 10 µm. The temperature dependence of n of CdTe in the temperature range of 20–80 K was $\frac{\Delta n_{\mathrm{CT}}}{\Delta T} = (7.1 \pm 0.2) \times 10^{-5}$. Therefore, the estimated n derived from the temperature dependence of CdTe includes an error of Δn as shown by Equation 4.34.

$$\Delta n = \left(\frac{\Delta n_{\mathrm{CZT}}}{\Delta T} - \frac{\Delta n_{\mathrm{CT}}}{\Delta T} \right) \Delta T \tag{4.34}$$

This result does not satisfy the required measurement accuracy of $\Delta n < 10^{-3}$ set in this study. This result indicates that the refractive index temperature dependence of CdTe and CdZnTe is different, and n at cryogenic temperature measured in this study is important.

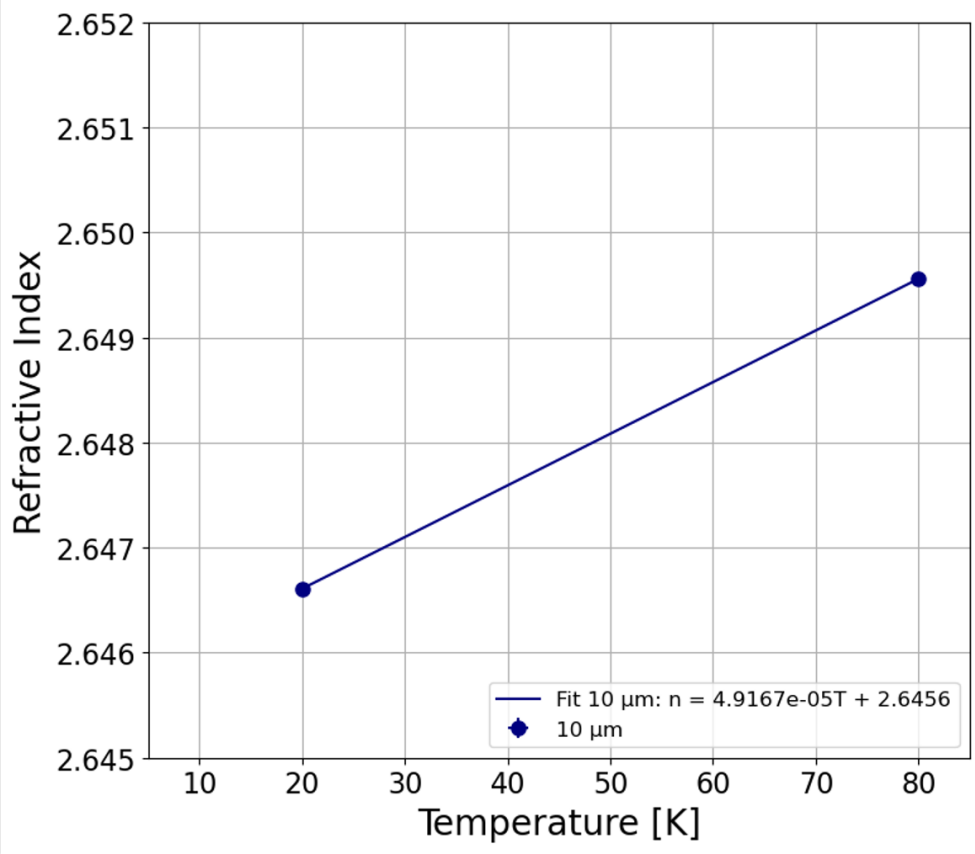

Figure 4.15: The temperature dependence of the refractive index of CdTe at wavelength of 10 μm

4.3 Comparison of measured and estimated CdZnTe refractive indices

In this section we compare the refractive indices of CdZnTe measured in this study with those of CdZnTe estimated from CdTe [48].

Assuming no wavelength dependence in the temperature dependence of CdTe, the temperature dependence $\frac{\Delta n_{CT}}{\Delta T} = (7.1 \pm 0.2) \times 10^{-5}$. at 10 µm is used. Table 4.7 shows the refractive index errors at each temperature based on n at temperature of 292.84 K.

Table 4.7: Temperature Dependence of Δn_{CT}

Temp. (K)	$\boldsymbol{\Delta n_{\mathrm{CT}}}$
12.40	-0.0138
22.347	-0.0133
50.59	-0.0119
70.57	-0.0109
292.84	0

These refractive index errors were used to offset from the room temperature n of CdZnTe to obtain a curve of wavelength dependence at each temperature (Figure 4.16)

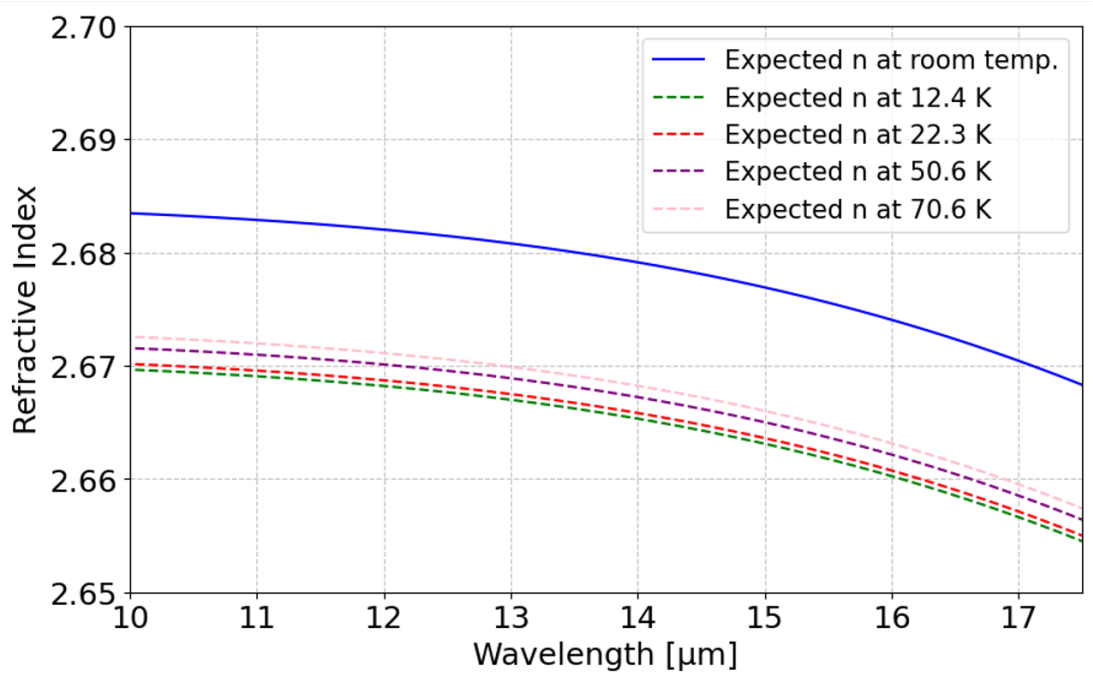

Figure 4.16: Estimation of n at each temperature from the wavelength dependence of n of CdZnTe at room temperature

From these curves in Figure 4.16, the refractive indices at the wavelength of 10.6, 11.4, 14.0, and 17.1 μm at each temperature were determined (Table 4.8).

Table 4.8: Refractive Index of CdZnTe at Different Temperatures and Wavelengths

Wavelength (μm)	Temp (K) **12.4**	**22.347**	**50.59**	**70.57**	**292.84**
10.6	2.66926	2.66976	2.67116	2.67216	2.68306
11.4	2.66867	2.66917	2.67057	2.67157	2.68247
14.0	2.66512	2.66562	2.66702	2.66802	2.67892
17.1	2.65622	2.65672	2.65812	2.65912	2.67002

Table 4.9 also shows the difference between this estimated refractive index and the refractive index measured in this study (Table 3.4 and 3.5).

Table 4.9: Δn for CdZnTe at Different Temperatures and Wavelengths.Blank areas are no measured values

Wavelength (μm)	Temp (K) **12.4**	**22.347**	**50.59**	**70.57**	**292.84**
10.6	0.03261	0.02973	0.03206	0.03146	0.02593
11.4	0.03593	0.03505	-	-	0.02834
14.0	0.03870	0.03560	-	-	0.03216
17.1	0.04158	0.03787	-	-	0.03537

Thus, the difference in refractive index is $\Delta n < 4.2 \times 10^{-2}$, and n of CdZnTe estimated from CdTe does not meet the required accuracy of $\Delta n_{\mathrm{req}} < 1 \times 10^{-3}$.

n of CdZnTe in the mid-infrared region at cryogenic and room temperatures has not been directly measured before this study. The results of this study are important in that the refractive indices of optical materials for mid-infrared applications were accurately measured at cryogenic temperatures.

4.4 Impact on the design of CdZnTe immersion gratings

Finally, the impact of the refractive index measurements obtained in this study on immersion grating fabrication will be discussed.

For GREX-PLUS, the target wavelength of observation is 17.754 μm, which can be captured even in the inner region to identify the position of the snow line in the equatorial plane of the protoplanetary disk. Since this emission line is extremely weak, we would

like to design the optical system so that this emission line can be observed efficiently. In other words, we want to design the optics so that the wavelength of the emission line is as close as possible to the blazed wavelength introduced in the introduction section 1.3, and to obtain a diffraction efficiency of 90% or higher. The accuracy of estimating that efficiency depends on the accuracy of n.

Ultimately, we would like to consider the impact on immersion gratings to be installed in GREX-PLUS, but the detailed optical system has not yet been determined. Therefore, for the case study, we will take as an example the mid-infrared high-dispersion spectrometer for ground-based observation, which is currently being studied under the leadership of Nakagawa, Baba, and Hirahara. This spectrometer is designed to demonstrate CdZnTe Immersion grating, and its specifications are shown in Table 1.4.

Assuming that the target wavelength is 13.5 μm and coincides with the brazed wavelength, the relative bandwidth of the free spectral range $\Delta\lambda = 0.157$ by Equation 1.5. Baba's initial study suggested that m=86 is a reasonable diffraction order for this spectrometer. Diffraction efficiency is maximum at the center of the free spectral range, and efficiency decreases as it shifts from there. Since the brazed wavelength is proportional to n, the accuracy of determining n is proportional to the accuracy of determining the brazed wavelength. Thus, if the refractive index accuracy is approximately $\Delta n_{\mathrm{total}} < 1.3 \times 10^{-3}$, there is a concern that the diffraction efficiency may drop to 75–85%. In the case of mounting on GREX-PLUS, the influence is considered to be small due to the lower diffraction order m and the wider free spectral range compared to ground-based spectrometers, and the current accuracy of $\Delta n_{\mathrm{total}} < 1.3 \times 10^{-3}$ is deemed sufficient.

Chapter 5

CONCLUSION

In this study, we developed a high-precision cryogenic mid-infrared refractive index measurement system at wavelengths of 10.6, 11.4, 14.0, and 17.1 μm between a temperature of 12.4 and 300 K. The novelty and originality of this system are as follows:

- Realization of a highly efficient optical system
- Construction of a cooling system that achieves cryogenic temperatures
- Establishment of a minimum deviation measurement method using a single-element detector

The wavelength range of Yamamuro et al. (2006) [29] was 0.365–3.5 μm, and the cooling system using liquid nitrogen allowed the sample to be cooled to 80 K. This system was customized to extend the wavelength range to 17 μm and to lower the sample temperature to 4 K by using a helium circulation-type mechanical refrigerator.

This measurement system has several sources of uncertainty. Among them, we quantitatively investigated the major systematic error factors, and the total uncertainty was found to be $\Delta n_{\mathrm{sum}} < 0.9 \times 10^{-3}$. Adding the statistical error from fitting to this value, the total error in refractive index is $\Delta n_{\mathrm{total}} < 1.3 \times 10^{-3}$. This value almost meets the required precision of $\Delta n_{\mathrm{req}} < 1.0 \times 10^{-3}$. However, the refractive index measurement error was one order of magnitude worse than in previous studies [29].

Two experiments were conducted to determine n of CdZnTe using the minimum deviation method (as shown in Table 3.4 and 3.5):

- Measurement of the apex angle of the prism using visible light autocollimation
- Infrared cryogenic deviation angle measurements

From the measurement results, we discuss the following:

- The temperature dependence of n of CdZnTe at low temperatures for each wavelength was revealed. This indicates that the temperature dependence of CdZnTe differs from that of CdTe.
- It was also found that the previously estimated refractive index of CdZnTe, based on the temperature dependence of CdTe, does not meet the required precision of $\Delta n_{\mathrm{req}} < 1.0 \times 10^{-3}$. Therefore, we demonstrated the importance of measuring refractive indices at cryogenic temperatures in the mid-infrared region.
- We examined the impact of the measurement precision of this system on the design of immersion gratings. We assumed the adaptation of the optical system to a high-dispersion spectrometer for ground-based demonstration of immersion gratings. As a result, it was found that the diffraction efficiency could drop to 75–85%. In the case of mounting on GREX-PLUS, the influence is considered to be small due to the lower diffraction order m and the wider free spectral range compared to ground-based spectrometers, and the current accuracy of $\Delta n_{\mathrm{total}} < 1.3 \times 10^{-3}$ is deemed sufficient.

By measuring n of CdZnTe at cryogenic temperatures in the mid-infrared region, we have contributed to the design of spectrometers equipped with a CdZnTe immersion grating. Furthermore, the wavelength range of this mid-infrared refractive index measurement system is unique worldwide, and it is expected that this system can be used to determine the refractive indices of various materials at cryogenic temperatures in the mid-infrared region.

Appendix A

Calculation of CWL of BPFs

We calculated the effective central wavelength (CWL) of the BPFs.

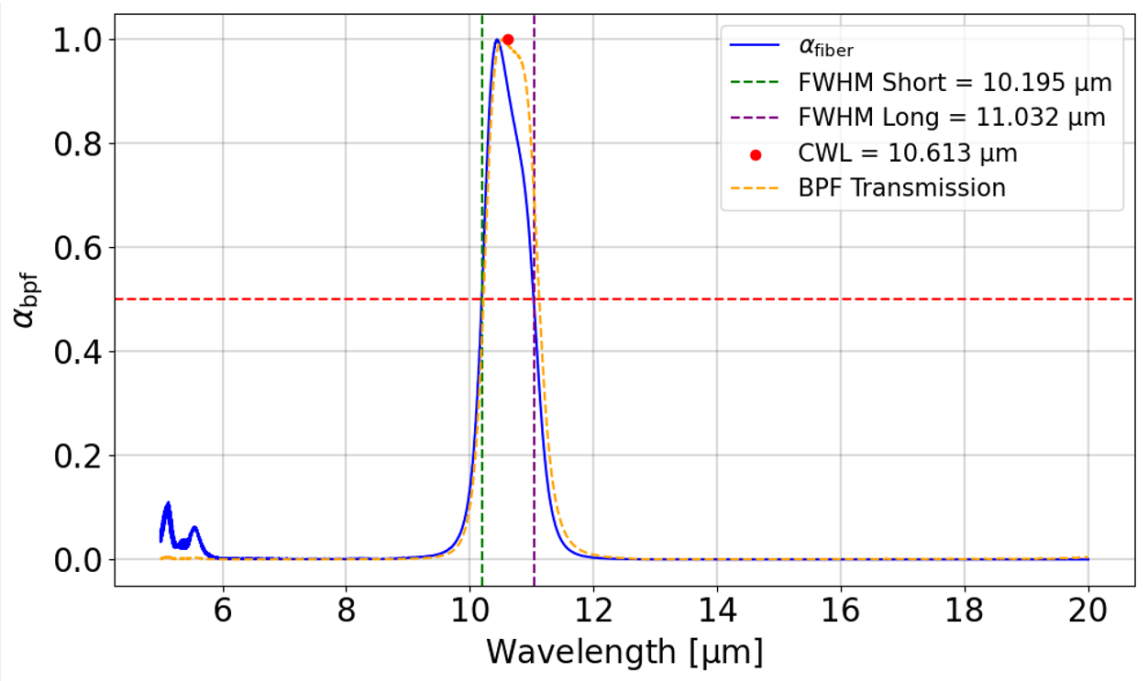

Figure A.1: CWL of 10.6 μm BPF

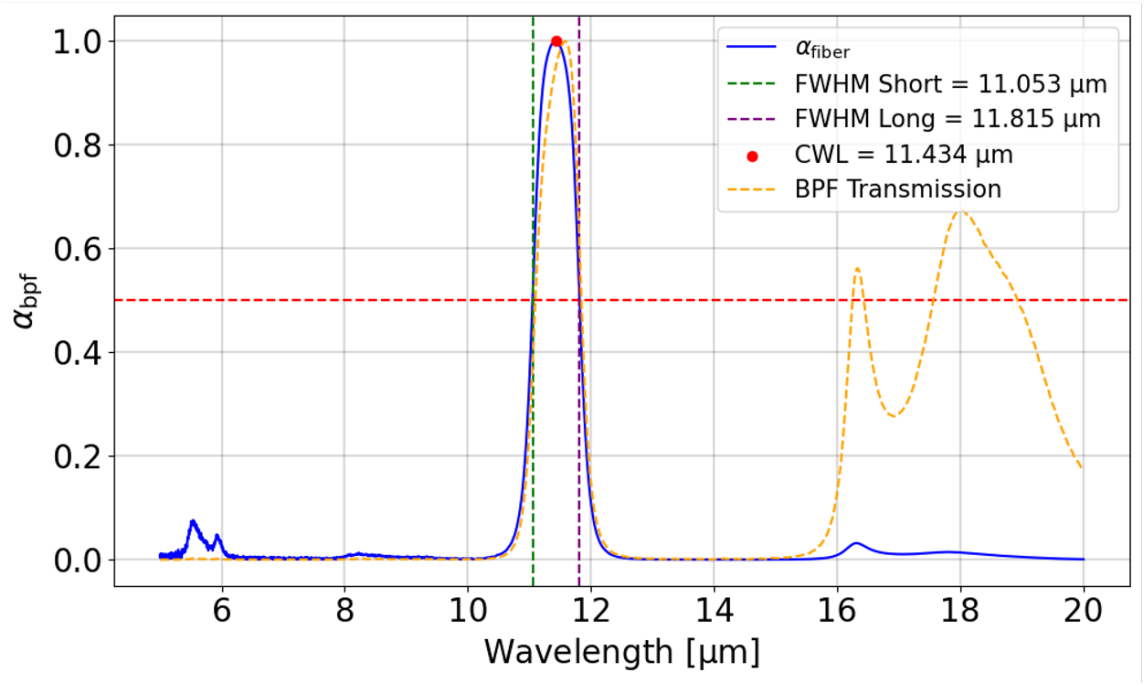

Figure A.2: CWL of 11.4 μm BPF

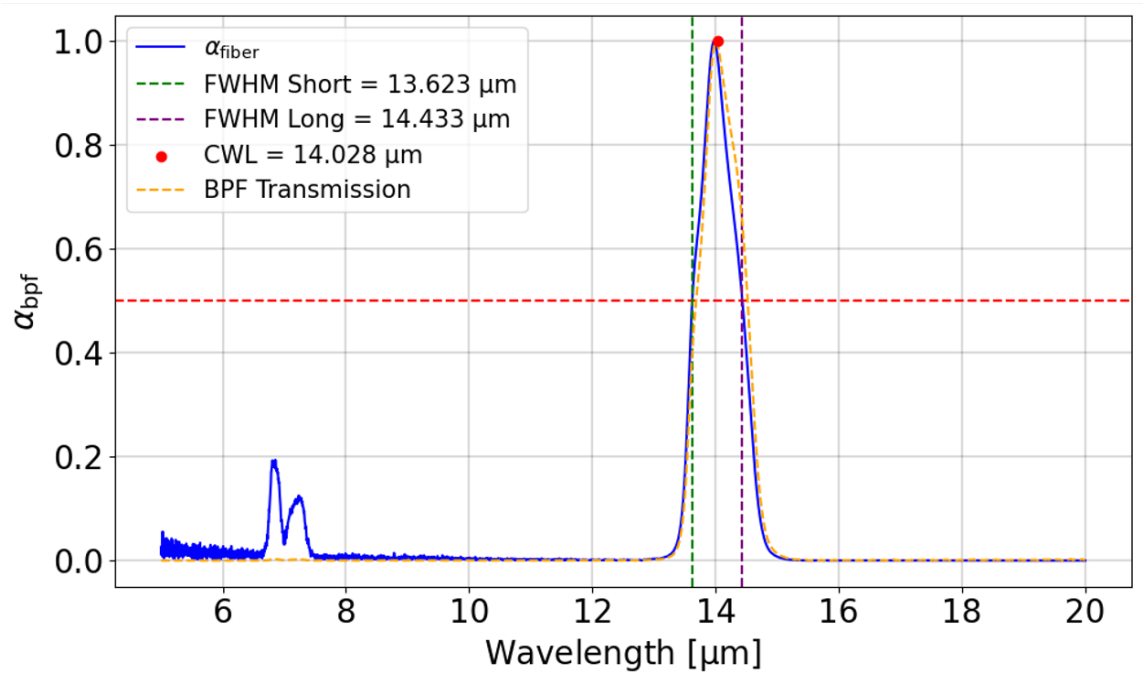

Figure A.3: CWL of 14.0 μm BPF

Appendix B

Calculation of Refractive Index Error

This set of equations quantifies how the angular error associated with the measurement (the error between the apex angle and the minimum declination angle) affects the error in n in prism-based refractive index measurements.

$$n = \frac{\sin\frac{\alpha+\beta}{2}}{\sin\frac{\alpha}{2}} = f(\alpha, \beta) \tag{B.1}$$

α: apex angle, β: minimum deviation angle

$$(\delta n)^2 = \left(\frac{\partial f}{\partial \alpha}\right)^2 \delta\alpha^2 + \left(\frac{\partial f}{\partial \beta}\right)^2 \delta\beta^2 \tag{B.2}$$

$$\frac{\partial f}{\partial \alpha} = \frac{n}{2\tan\frac{\alpha}{2}} + \sin\left(\frac{\alpha+\beta}{2}\right) \cdot \left(-\frac{1}{\sin^2\frac{\alpha}{2}} \cdot \cos\frac{\alpha}{2}\right) \tag{B.3}$$

$$\frac{\partial f}{\partial \beta} = \frac{n}{2\tan\frac{\alpha+\beta}{2}} \tag{B.4}$$

$\delta\alpha$: error in the apex angle, $\delta\beta$: error in the deviation angle

Note: In principle, β is used to represent the minimum deviation angle when expressing δ. However, to avoid confusion with δ, β is explicitly used here.

Acknowledgements

Throughout the preparation of this dissertation, I have received invaluable guidance and support from many individuals.

First, I would like to express my sincere gratitude to Assoc. prof. Keigo Enya at JAXA/ISAS, who kindly took on my supervisor role during my doctoral thesis review and provided detailed guidance despite his busy schedule. I am deeply grateful for his support.

I extend my heartfelt appreciation to Assoc. prof. Yasuhiro Hirahara at Nagoya University, who is the chief examiner of this doctoral thesis, and to Prof. Takao Nakagawa at JAXA/ISAS, who is the sub-chief examiner. Since I was a master's student, they have offered invaluable advice and support for my experiments. Their technical expertise and knowledge taught me not only research methodologies but also the essence of scientific inquiry. I am truly grateful for their patience and guidance.

I would also like to thank Assoc. prof. Toyoaki Suzuki and Prof. Toru Yamada at JAXA/ISAS for their insightful feedback, which helped improve my doctoral thesis. Their meticulous reviews and suggestions played a crucial role in refining my research.

Special thanks to Assoc. prof. Takehiko Wada at NAOJ and Dr. Shunsuke Baba at JAXA/ISAS for their support in collaborative research and paper writing. Their contributions have been invaluable to my academic progress.

I am grateful to Dr. Ryoichi Koga at Nagoya City University and to Mr. Li Yuan, Mr. Biao Zhao, and Mr. Hiroshi Sasako at Nagoya University for their support during. Their hospitality and collaboration enriched my research experience.

I also extend my gratitude to lab members, including Mr. Ting-Chi Huang, Mr.

Hiromichi Ebihara and Mr. Ryodai Yamaguchi, and Mr. Hayato Tanaka. Thanks to their friendship, my graduate school experience was truly fulfilling.

My deep appreciation goes to Mrs. Hitomi Kimura, Mrs. Chieko Nakaya, and Mrs. Kumiko Nishimatsu at JAXA/ISAS Infrared Group Secretariat. Their support ensured the smooth progress of my research, I was always reassured by their kind responses.

The members of the JAXA/ISAS LIRA Group have warmly supported me since I was a master's student, providing numerous opportunities for learning and experience. I am profoundly grateful for their encouragement and guidance.

I would also like to thank prof. Hideo Matsuhara at JAXA/ISAS for warmly welcoming me into the field of space development.

I extend my appreciation to Mr. Yoshiaki Mitsutake, Mr. Shunichi Nakatsubo, and the staffs at the JAXA/ISAS Advanced Machining Group for their assistance in manufacturing crucial components for my research. Their prompt and precise work was invaluable.

Mr. Kenji Fukunabe at the JAXA/ISAS Electronics Workshop provided critical support in the development of visible light detectors. His hands-on training in electronic circuit design was an invaluable learning experience for me.

I am also grateful to Mr. Masahiro Kohira, Mrs. Naoko Fukayama, and Mrs. Miho Nakayama at SOKENDAI's student affairs office. Their support greatly contributed to my smooth graduate school life.

This research was supported by JSPS KAKENHI (Grant Numbers JP23H05441, JP23H01222, JP23H01222) and JST SPRING (Grant Number JPMJSP2104). I would like to express my deepest gratitude for this financial support.

Many individuals supported my graduate school life.

Ms. Kaori Hirata is my only female Ph.D. student colleague at ISAS. She shared countless memorable moments with me. We signed an armistice and launched the IGC and Uchupping. We chat and chat during hard times and happy times. I enjoyed the five years I spent with you. Thank you for inviting me to SCCOT. I hope we'll always be friends.

My closest friends at ISAS, including Mr. Ayumu Nohno, Mr. Kento Kaneko, and Ms. Sara Nakama, made my time here even more special. Along with Ms. Kaori and Ayumu's wife, Mrs. Yui, we made unforgettable memories through trips and celebrations. Though we are now embarking on separate paths, I eagerly anticipate our future reunions. Thank you for bringing color to my graduate life.

Dr. Mayu Tominaga and Dr. Takumi Midooka were exemplary seniors for me. They led seminars and research events and had high standard leaderships. Though I may not have reached their level, I aspired to follow their example. Thank you very much for your many supports.

Asst. Prof. Go Murakami at JAXA/ISAS provided me with valuable opportunities to participate in outreach. Through these activities, I expanded my network beyond my field, broadening my research perspective. My goal is to become a researcher who enjoys both research and outreach to the fullest like Asst. Prof. Go. Thank you for giving me the opportunity to stay in academia. I'm looking forward to working with you as a research collaborator.

Dr. Yudai Suzuki, Dr. Shunta Kimura, Dr. Yuki Kubo, Mrs. Iori Kajitani, and SCCOT members have been like an oasis for me. They listened when I was struggling, helped me recharge, and encouraged me to face my research challenges with renewed energy. Thank you always.

Prof. Hiroto Habu at JAXA/ISAS supported the launching and activities of Uchupping, as well as my project presentations. The experiences and skills I gained from these activities have been invaluable, and I hope to continue exploring new outreach possibilities. I deeply appreciate his guidance.

The members of Uchupping helped me realize my dream of combining space and projection mapping. Though I had many shortcomings as a leader, they supported me. Thank you for being part of this incredible project. Let's collaborate again.

I would also like to thank Mrs. Kanako Toshioka, Mr. Aya Nakajo, and PR team for providing outreach opportunities. These activities allowed me to connect with researchers and receive valuable feedback on my research.

Finally, I wish to express my deepest gratitude to those who supported me in my personal life.

Mr. Koichi Taniguchi has supported me since I was a undergraduate student and has been my greatest cheerleader throughout my Ph.D. life. During the final year, when I was entirely absorbed in research and barely spent time together, he never once complained and always prioritized my schedule. Thank you for being my unwavering support.

My family has supported me in countless ways. I became interested in physics as a child after watching the TV drama “Galileo”, the mysterious flying object “Komekome 1”, and frequent visits to science museums with my grandfather. They have always encouraged me. Without their support, I would not have completed graduate school. Thank you from the bottom of my heart. I will continue to do my best.

Bibliography

[1] Wesley A. Traub and Mark T. Stier, "Theoretical atmospheric transmission in the mid- and far-infrared at four altitudes," *Applied Optics*, Vol. 15, pp. 364–377, 1976., URL: https://doi.org/10.1364/AO.15.000364

[2] Masanori Iye, *Shirīzu Gendai no Tenmongaku Vol. 15: Uchū no Kansoku - Hikari, Sekigai Tenmongaku (Modern Astronomy Series Vol. 15: Observing the Universe - Optical and Infrared Astronomy)*, Nihon Hyoronsha, 2023.

[3] G. Neugebauer, H. J. Habing, *et al.*, "The Infrared Astronomical Satellite (IRAS) mission," *The Astrophysical Journal*, Vol. 278, p. 1, 1984.

[4] H. Murakami, M. M. Freund, *et al.*, "Infrared Astronomical Mission Overview," *Publications of the Astronomical Society of Japan (PASJ)*, Vol. 48, p. 41, 1996.

[5] M. F. Kessler, J. A. Steinz, *et al.*, "The Infrared Space Observatory (ISO) mission," *Astronomy & Astrophysics (A&A)*, Vol. 315, p. 27, 1996.

[6] M. W. Werner, T. L. Roellig, *et al.*, "The Spitzer Space Telescope Mission," *The Astrophysical Journal Supplement Series (ApJS)*, Vol. 154, p. 1, 2004.

[7] H. Murakami, H. Baba, *et al.*, "The AKARI Infrared Space Telescope mission," *Publications of the Astronomical Society of Japan (PASJ)*, Vol. 59, p. 369, 2007.

[8] K. M. Amanda, E. Peter, *et al.*, "Title of the SPIE Conference Paper," *SPIE Proceedings*, Vol. 5899, p. 262, 2005.

[9] G. L. Pilbratt, J. R. Riedinger, *et al.*, "The Herschel Space Observatory Mission Overview," *Astronomy & Astrophysics (A&A)*, Vol. 518, p. 1, 2010.

[10] M. Clampin, "James Webb Space Telescope (JWST) Overview," *SPIE Proceedings*, Vol. 9143, p. 02, 2014.

[11] T. Nakagawa, "Terahertz Astronomy and Future Prospects," *IEEE Transactions on Terahertz Science and Technology*, Vol. 5, No. 6, pp. 1133–1141, 2015.

[12] GREX-PLUS Study Group, "Strategic Implementation of Medium-Class Plan GW", *GREX-PLUS Proposal*, Medium-class space mission proposal for gravitational wave detection.

[13] C. Hayashi, K. Nakazawa, Y. Nakagawa, "Formation of the Solar System. in Protostars and Planets II", *University of Arizona Press*, p. 1100-1153, 1985.

[14] A. Oka, T. Nakamoto, and S. Ida, "EVOLUTION OF SNOW LINE IN OPTICALLY THICK PROTOPLANETARY DISKS: EFFECTS OF WATER ICE OPACITY AND DUST GRAIN SIZE" *The Astrophysical Journal*, Volume 738, Issue 2, article id. 141, 11 pp., 2011, URL: https://iopscience.iop.org/article/10.1088/0004-637X/738/2/141

[15] Shota Notsu, Hideko Nomura, Daiki Ishimoto, Catherine Walsh, Mitsuhiko Honda, Tomoya Hirota, and T. J. Millar, "CANDIDATE WATER VAPOR LINES TO LOCATE THE H_2O SNOWLINE THROUGH HIGH-DISPERSION SPECTROSCOPIC OBSERVATIONS. I. THE CASE OF A T TAURI STAR," *The Astrophysical Journal*, Vol. 827, p. 113, 2016., URL: https://doi.org/10.3847/0004-637x/827/2/113

[16] Shota Notsu, Hideko Nomura, Daiki Ishimoto, Catherine Walsh, Mitsuhiko Honda, Tomoya Hirota, and T. J. Millar, "Candidate Water Vapor Lines to Locate the H_2O Snowline Through High-dispersion Spectroscopic Observations. II. The Case of a Herbig Ae Star," *The Astrophysical Journal*, Vol. 836, p. 118, 2017., URL: https://doi.org/10.3847/1538-4357/836/1/118

[17] J. P. Marsh, D. J. Mar, and D. T. Jaffe, "Production and evaluation of silicon immersion gratings for infrared astronomy", *Applied Optics*, Vol. 46, pp. 3400–3416, 2007, URL: https://doi.org/10.1364/AO.46.003400

[18] Michael A. Gully-Santiago, Daniel T. Jaffe, Cynthia B. Brooks, Daniel W. Wilson, and Richard E. Muller, "High performance Si immersion gratings patterned with electron beam lithography," *Advances in Optical and Mechanical Technologies for Telescopes and Instrumentation*, Proceedings of SPIE, Vol. 9151, p. 91515K, 2014., URL: https://doi.org/10.1117/12.2056912

[19] Yasuhiro Hirahara, Tsuyoshi Hirao, Yoshio Tatamitani, Tomohisa Yonezu, Noboru Ebizuka, Kentarou Kawaguchi, Hitoshi Tokoro, and Tomomichi N. Oka, "Development of the mid-IR echelle high-dispersion spectrograph employing the germanium immersion grating," *Ground-based and Airborne Instrumentation for Astronomy III*, Proceedings of SPIE, Vol. 7735, p. 77351B, 2010., URL: https://doi.org/10.1117/12.856624

[20] Yuki Sarugaku, Sayumi Kaji, Yuji Ikeda, Naoto Kobayashi, Takashi Sukegawa, Takao Nakagawa, Hirokazu Kataza, Sohei Kondo, Chikako Yasui, Kenshi Nakanishi, and Hideyo Kawakita, "Infrared Attenuation Spectrum of Bulk High-Resistivity CdZnTe Single Crystal in Transparent Wavelength Region Between Electronic and Lattice Absorptions," *Journal of Electronic Materials*, Vol. 46, pp. 282–287, 2017., URL: https://doi.org/10.1007/s11664-016-4917-3

[21] Yuji Ikeda, Naoto Kobayashi, Yuki Sarugaku, Takashi Sukegawa, Shigeru Sugiyama, Sayumi Kaji, Kenshi Nakanishi, Sohei Kondo, Chikako Yasui, Hirokazu Kataza, Takao Nakagawa, and Hideyo Kawakita, "Machined immersion grating with theoretically predicted diffraction efficiency," *Applied Optics*, Vol. 54, No. 16, pp. 5193–5202, 2015., URL: https://doi.org/10.1364/AO.54.005193

[22] Yuan Li, Yasuhiro Hirahara, Biao Zhao, Hiroshi Sasago, Umi Enokidani, Hideo Matsuhara, Takao Nakagawa, Ryoichi Koga, and Takehiko Wada, "Transmittance

measurement of high-resistivity CdZnTe at cryogenic temperature for material selection of the immersion grating for the next-generation infrared telescope GREX-PLUS," *Space Telescopes and Instrumentation 2024: Optical, Infrared, and Millimeter Wave*, Proceedings of SPIE, Vol. 13092, p. 130923E, 2024., URL: https://doi.org/10.1117/12.3019645

[23] Ioannis Argyriou, Alistair Glasse, David R. Law, Alvaro Labiano, Javier Álvarez-Márquez, Polychronis Patapis, Patrick J. Kavanagh, Danny Gasman, Michael Mueller, Kirsten Larson, Bart Vandenbussche, Adrian M. Glauser, Pierre Royer, Daniel Dicken, Jake Harkett, Beth A. Sargent, Michael Engesser, Olivia C. Jones, Sarah Kendrew, Alberto Noriega-Crespo, Bernhard Brandl, George H. Rieke, Gillian S. Wright, David Lee, and Martyn Wells, "JWST MIRI flight performance: The Medium-Resolution Spectrometer," *Astronomy & Astrophysics*, Vol. 675, p. 15, 2023., URL: https://doi.org/10.1051/0004-6361/202346489

[24] Akio K. Inoue, Issei Yamamura, Toyoaki Suzuki, Takao Nakagawa, Hidehiro Kaneda, Hideko Nomura, Tadayuki Kodama, Takehiko Wada, Fumihide Iwamuro, Kentaro Motohara, Yutaka Komiyama, Shinki Oyabu, Yuichi Harikane, Takashi Moriya, Masami Ouchi, Toru Yamada, and Shota Notsu, "Concept study of GREX-PLUS: Galaxy Reionization EXplorer and PLanetary Universe Spectrometer," *Space Telescopes and Instrumentation 2024: Optical, Infrared, and Millimeter Wave*, Proceedings of SPIE, Vol. 13092, p. 130920Y, 2024., URL: https://doi.org/10.1117/12.3017780

[25] Takao Nakagawa, Hideo Matsuhara, Umi Enokidani, Toyoaki Suzuki, Shunsuke Baba, Yasuhiro Hirahara, Hidehiro Kaneda, Ryoichi Koga, Li Yuan, Biao Zhao, Daiki Takama, Hiroshi Sasago, Takehiko Wada, Toshihiro Nakaoka, Taiki Eda, Ryota Kakihara, Yoshinori Shiomitsu, Takuya Hosobata, Noboru Ebizuka, Yutaka Yamagata, Shota Notsu, and Hideko Nomura, "Development of the CdZnTe Immersion Grating Spectrometer for the Detection of Snow-Lines with High-Resolution Spectroscopy," *Space Telescopes and Instrumentation 2024: Optical, Infrared,*

and Millimeter Wave, Proceedings of SPIE, Vol. 13092, p. 130923D, 2024., URL: https://doi.org/10.1117/12.3019636

[26] Douglas B. Leviton, Manuel A. Quijada, Kevin H. Miller, "New measurements of MWIR cryogenic refractive indices for silicon and germanium from CHARMS," *Proceedings of SPIE*, vol. 12188, p. 121882K, 2022. URL: https://doi.org/10.1117/12.2631523

[27] Simon G. Kaplan and Michael E. Thomas, "Measurement of the o-ray and e-ray infrared refractive index and absorption coefficient of sapphire from 10 K to 295 K," *Proceedings of SPIE*, vol. 4822, pp. 41-50, 2002.

[28] Euclid Collaboration, Y. Mellier et al., "Euclid. . Overview of the Euclid mission," *Astronomy Astrophysics*, vol. 682, L2, 2024., URL: https://doi.org/10.48550/arXiv.2405.13491

[29] Tomoyasu Yamamuro, Shuji Sato, Takahiro Zenno, Norihide Takeyama, Hideo Matsuhara, Ippei Maeda, and Yoshio Matsueda, "Measurement of refractive indices of 20 optical materials at low temperatures", *Optical Engineering*, Vol. 45, No. 8, p. 083401, 2006., URL: https://doi.org/10.1117/1.2336241

[30] Shimadzu Corporation, "Kalnew Precision Spectormeter", URL: https://www.shimadzu.co.jp/products/opt/products/spec/index.html

[31] Bunkoukeiki Co.,Ltd, "NRI-200 Distributed infrared spectroscopy evaluation system", URL: https://www.bunkoukeiki.co.jp/materialevalutionoptocal-nri-200.html

[32] LIAO Sheng, NI Lei, REN Qi-feng, "Design of a cryogenic absolute prism refractometer for infrared optical materials," *Proceedings of SPIE*, Vol. 8321, 2011, pp. 832117-1–832117-8., URL: https://doi.org/10.1117/12.904003

[33] Umi Enokidani, Hideo Matsuhara, Takao Nakagawa, Yasuhiro Hirahara, Ryoichi Koga, Li Yuan, Biao Zhao, Daiki Takama, Hiroshi Sasago, and Takehiko Wada,

"Development of a Mid-Infrared Refractive Index Measurement System at Cryogenic Temperature for the Development of an Immersion Grating to be onboard Next-Generation Infrared Space Telescope GREX-PLUS," *Space Telescopes and Instrumentation 2024: Optical, Infrared, and Millimeter Wave*, Proceedings of SPIE, Vol. 13092, p. 130923F, 2024., URL: https://doi.org/10.1117/12.3019753

[34] Thorlabs, Inc., "MPD019-M01 - Ø1/2" 90° Off-Axis Parabolic Mirror, Prot. Gold, RFL = 1"", URL: https://www.thorlabs.co.jp/thorproduct.cfm?partnumber=MPD019-M01

[35] IR System Co., Ltd., "Pulse/continuous emission thermal type infrared light source (1∼20 μm)", URL: https://www.irsystem.com/product/ir_emitter_pulse/

[36] DOKO Engineering, "MATSUURA & KATAGIRI LAB", URL: https://www.ecei.tohoku.ac.jp/photonics/research.html

[37] Yuji Matsuura, Todd Abel, and James A. Harrington, "Optical properties of small-bore hollow glass waveguides," *Applied Optics*, Vol. 34, pp. 6842–6847, 1995., URL: https://doi.org/10.1364/AO.34.006842

[38] BOMEM INC., "DA SERIES DETECTORS MANUAL"

[39] Kogakugiken Corp., "Data sheet: JX-PSPC-526650"

[40] Hiroshi Maeshima, Kosei Matsumoto, Yasuhiro Hirahara, Takao Nakagawa, Ryoichi Koga, Yusuke Hanamura, Takehiko Wada, Koichi Nagase, Shinki Oyabu, Toyoaki Suzuki, Takuma Kokusho, Hidehiro Kaneda, and Daichi Ishikawa, "Infrared Absorption and Its Sources of CdZnTe at Cryogenic Temperature," *Journal of Electronic Materials*, Vol. 51, pp. 564–576, 2022., URL: https://doi.org/10.1007/s11664-021-09361-1

[41] Querry, Marvin, "Optical Constants of Minerals and Other Materials from the Millimeter to the Ultraviolet", URL: https://apps.dtic.mil/sti/citations/ADA192210

[42] Douglas B. Leviton, Bradley J. Frey, Timothy J. Madison, "Temperature-dependent refractive index of CaF and Infrasil 301," *Proceedings Volume 6692, Cryogenic Optical Systems and Instruments XII*, p.669204, 2007), URL: https://doi.org/10.1117/12.735594

[43] SCHOTT AG, "SCHOTT N-BK7 Optical Glass Datasheet", 2023, URL: chrome-extension://efaidnbmnnnibpcajpcglclefindmkaj/https://media.schott.com/api/public/content/41e799d0bf874807a0bb8e702fbb75b5?v=54856406

[44] Simon G. Kaplan, Michael E. Thomas, "Measurement of the o-ray and e-ray infrared refractive index and absorption coefficient of sapphire from 10 K to 295 K," *Proceedings of SPIE*, Vol. 4822, pp. 41–50, 2002., URL: https://doi.org/10.1117/12.453432

[45] P. Hlídek, J. Bok, J. Franc, and R. Grill, "Refractive index of CdTe: Spectral and temperature dependence," *Journal of Applied Physics*, Vol. 90, pp. 1672–1674, 2001., URL: https://doi.org/10.1063/1.1385351

[46] Di Yang, Michael E. Thomas, William J. Tropf, and Simon G. Kaplan, "Infrared refractive index measurements using a new method," *Proceedings of SPIE*, Vol. 4103, pp. 42–52, 2000., URL: https://doi.org/10.1117/12.396808

[47] Richard J. Mathar, "Refractive index of humid air in the infrared: model fits," *Journal of Optics A: Pure and Applied Optics*, Vol. 9, No. 5, p. 470, 2007., URL: https://doi.org/10.1088/1464-4258/9/5/008

[48] J. S. Browder, *Handbook of Infrared Optical Materials*, Marcel Dekker, Inc., New York, 1991.